SCIENTIFIC PROGRESS OF THE MC-PAD NETWORK

January 2013

The MC-PAD network

MC-PAD is a multi-site Initial Training Network on particle detectors in physics experiments. It comprises nine academic participants, three industrial partners and two associated academic partners. 17 recruited Early Stage and 5 Experienced Researchers have performed their scientific work in the network.

The research and development work of MC-PAD is organized in 12 work packages, which focus on a large variety of aspects of particle detector development, electronics as well as simulation and modelling.

The network was established in November 2008 and lasted until October 2012 (48 months). This report describes the R&D activities and highlights the main results achieved during this period.

Table of contents

PROJECT 1: RADIATION TOLERANT MINI-STRIP TRACKING DETECTORS

Project Coordinator: Michael Moll, CERN.

Nicola Pacifico, ESR, CERN. Supervisor: Michael Moll.

Tomáš Balog, ESR, GSI. Supervisor: Johann Heuser.

INTRODUCTION

Since decades, silicon strip sensors have been the favored choice for the construction of inner tracking systems in High Energy Physics (HEP) experiments. Due to their proximity to the interaction point silicon sensors are often exposed to high radiation levels. This can on the long term affect heavily on their performance. Aim of the present project was on the one hand to contribute to the definition of radiation tolerant silicon sensor technologies for future silicon strip trackers at the high luminosity LHC experiments and on the other hand develop radiation tolerant silicon detectors for the Silicon Tracking System (STS) at the CBM Experiment at FAIR.

RADIATION EFFECTS ON SILICON SENSORS

The current generation of HEP experiments mostly uses silicon sensors produced with n-type Float Zone silicon. The Float Zone process is a long-established growth technique, which allows the production of silicon ingots with a high level of crystalline purity. This crystalline purity translates into a very high resistivity of the resulting wafers, reaching up to several 10^4 Ω cm. Since operation of a silicon sensor requires its complete depletion from charge carriers, a high resistivity bulk allows for low depletion voltages at a typical device thickness of about 300μm. However, well-established studies on radiation damage [1] have demonstrated that irradiation with hadrons creates acceptor levels in the silicon bulk material that compensate and eventually overwhelm the initial concentration of shallow donors, producing at first a space charge sign inversion from positive to negative space charge and afterwards a steep increase of the full depletion voltage. These are two of the main reasons for the efficiency loss in silicon sensors due to radiation damage. The space charge sign inversion brings the high electric field region away from the readout electrode and the increasing negative space charge makes it on the long term impossible to fully deplete the bulk, with a resulting loss in the sensitive volume of the sensor.

A further important effect of hadron irradiation on silicon sensors is the creation of electrically active defects which are located energetically deep in the band gap. These defects act as generation/recombination centres, thus having a twofold effect:

- Reduction of the lifetime of carriers and thus signal loss, due to charge carrier trapping.

- Increase of noise and power dissipation, due to the increase of the leakage current.

In order to overcome or compensate some of the above-mentioned effects, several alternative silicon materials and sensor technologies have been investigated, partly resulting in promising results in terms of radiation hardness. For example, oxygen enrichment of the silicon bulk material [2] is known to induce a process which compensates part of the negative space charge produced during irradiation or, in some special cases, can even suppress the space charge sign inversion effect. Another very promising approach is to use p-type bulk sensors with n-readout which avoid the space charge sign inversion of the bulk, as they have net negative space charge before and after irradiation [3].

3

In order to better understand and parameterize radiation effects on presently used and new silicon materials and sensor types, the ESR at CERN has developed new measurement setups for the investigation of heavily irradiated silicon sensors and has performed systematic measurements on several materials [4].

Characterization using laser beams

Two setups were developed with the purpose of studying the field configuration of heavily irradiated silicon sensors. Both setups make use of the so called "Transient Current Technique" (TCT). In this technique, a localized cloud of charge is generated in the bulk. As the charge drifts under the effect of an applied electric field, the transient of the induced charge on the readout electrodes is measured. Studying the shape of the transient pulse provides information on the geometrical configuration of the electric field inside the sensor. In the standard TCT setup (see Fig. 1), the charge cloud is generated by means of a red laser, which is projected on one of the two electrodes of a silicon planar diode. The absorption length, in the order of 3 µm, allows for the production of a very shallow charge cloud, which will drift as a whole and "scan" the field inside the detector. This technique, however powerful, is not suitable for studying heavily irradiated sensors, as the pulse shape is heavily affected by the dramatic reduction of drifting charge carriers caused by their short lifetime. In order to be able to scan all the thickness of a sensor with an amount of charge virtually unaffected by carrier trapping, an evolution of this technique called "Edge-TCT" was developed within the RD50 collaboration [5, 6], and the ESR personally built a setup at CERN exploiting this new technique. In this evolution, the charge is injected by focusing, transversally to the detector electrodes, an infrared laser beam, underneath an electrode. A scanning table allows injecting the charge at chosen depths of the sensor. Advanced manipulation of the data allows obtaining profiles of the carrier drift velocity also for heavily irradiated sensors.
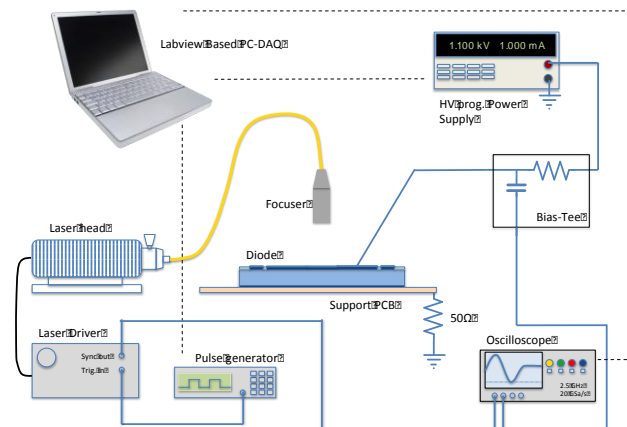

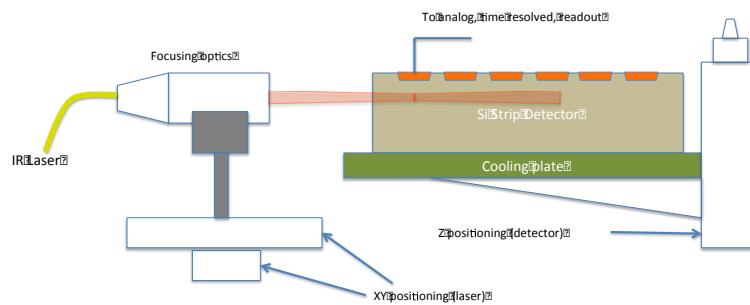**Fig. 1: Schematic view of the Transient Current Technique setup**

Fig. 2: Schematic view of the Edge-Transient Current Technique setup

Characterization using a source

In order to understand the evolution of the Signal-to-Noise ratio of silicon strip sensors with increasing irradiation, in conditions as close as possible to their operation in HEP experiments, a setup was built to measure the charge collection efficiency with MIP-like particles, namely β particles from a ^{90}Sr source. The setup was used to characterize several different silicon materials (Magnetic Czochralski, Float Zone) irradiated with neutrons and/or protons. In particular, a systematic study was performed on n-type silicon strip sensors manufactured by Hamamatsu and currently used in most of the LHC trackers. The study aimed at assessing the effects of a prolonged annealing on the charge collection efficiency of the sensors, with remarkable results which have been submitted for publication.

Results overview

The purpose of the project has been twofold.

- Characterization of the sensors currently employed in LHC experiments to provide a better modelling of their performance evolution throughout the operation of the LHC
- Study of new materials for high-luminosity applications in future experiments

The first study has been carried out as, though the current generation of silicon sensors (FZ n-bulk, p-readout) has been thoroughly characterized in recent years, there was a lack of literature on the effects of long term annealing. This is for example important to understand the impact of cooling failures or long-term room-temperature maintenance on the charge collection efficiency of the strip sensors. The study was carried out on sensors of the same type as the ones currently installed in LHC. The results (a sample is shown in Fig. 3) suggest that at higher fluences, the cooling will be essential to keep sensor parameters within operational limits.
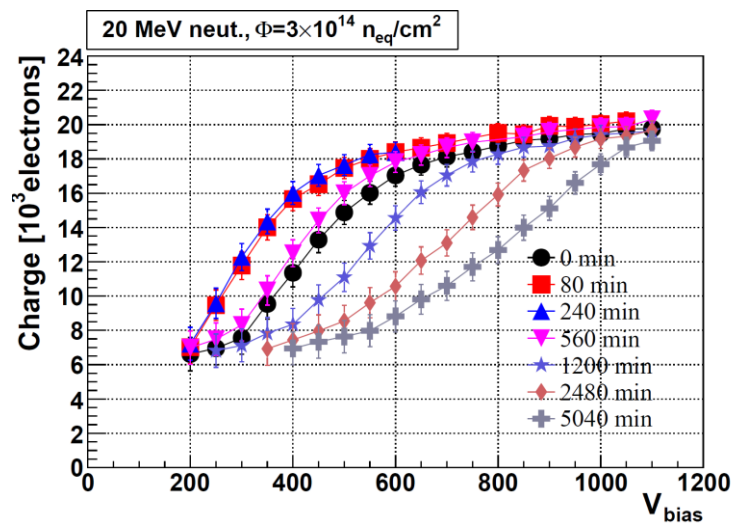

Fig. 3: Annealing induced development of collected charge in a FZ p-on-n sensor irradiated to 3×10^{14} n/cm2 at 60°C.

In the study of new materials and technologies, Edge-TCT was extensively used to characterize both n-bulk oxygenated devices (Fig. 4) and p-bulk detectors (Fig. 5). In both cases, the previously observed higher radiation hardness was found to be largely due to a favourable field profile development with a high-field present on the readout side.
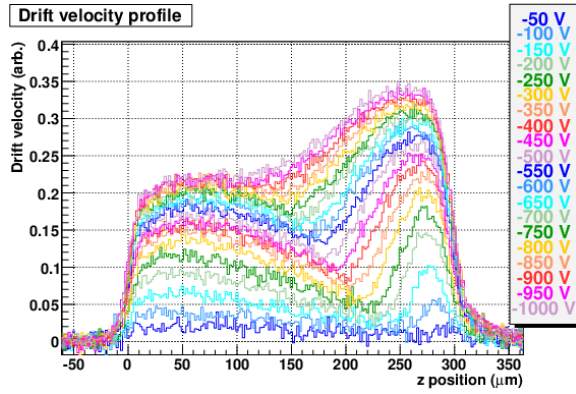
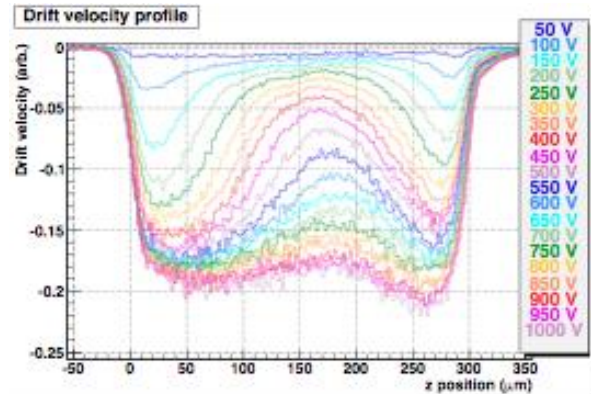**Fig. 4: Sample drift velocity profile for a Float Zone p-bulk detector irradiated to 3×10^15 n/cm^2.**

Fig. 5: Sample drift velocity profile for a Float Zone p-bulk detector irradiated to 1.6×10^16 23 GeV protons / cm^2.

A remarkable result of the research project has been the discovery of a bistable defect in p-bulk silicon devices, which are known to express charge multiplication at extremely high hadron irradiation fluences. The abovementioned defect, can be primed thermally or by current injection, is stable for several days at low temperature (-20°C) and produces a notable modification in the collected charge, almost deactivating completely the charge multiplication mechanism (see Fig. 6).
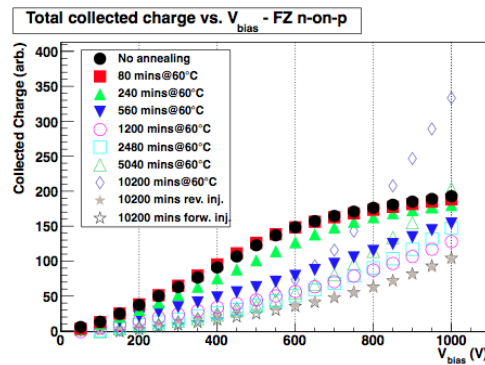

Fig. 6: Annealing induced development of collected charge in a FZ p-on-n sensor irradiated to 1.6×10^16 23 GeV protons / cm2.

DOUBLE-SIDED SILICON MICROSTRIP DETECTOR SYSTEMS FOR THE CBM SILICON TRACKER

The Compressed Baryonic Matter (CBM) experiment [7] is one of the main experimental parts of the new Facility for Antiproton and Ion Research (FAIR) which is under construction at the Helmholtz Centre for Heavy-ion Research (GSI) in Darmstadt, Germany. The aim of the research program on nucleus-nucleus collisions is the investigation of highly compressed nuclear matter. The role of the CBM experiment is to map the phase diagram of strongly interacting matter and to explore the fundamental properties of QCD. The FAIR synchrotrons will deliver high intensity beams to the CBM cave with a rate up to 10^9 ions per second on a target of 1% nuclear interaction length. This CBM experiment requires radiation hard and fast detectors with high-speed read-out electronics for data acquisition.

The CBM detector is illustrated in the left panel of Fig. 1. The Silicon Tracking System (STS) as the main detector of the CBM experiment will be built from 300 μm thick double-sided silicon microstrip sensors. The strips on the front and back sides are arranged under a stereo angle of 7.5°. The system will consist of

8 tracking stations at distances between 30 cm and 100 cm downstream of the target, covering a total area of about 4 m^2 and comprising more than 2 million read-out channels. In order to achieve a low material budget, the read-out electronics will be placed at the periphery of the detector system. The silicon sensors are mounted onto light carbon fibre supports. The sensors are read out through ultra-thin multi-line aluminum-polyimide flat cables. In central Au+Au interactions at 25 AGeV projectile energy up to 1000 charged particles are produced per collision. About 700 particles traverse the aperture of the detector at up to 10 MHz rate. Due to their inhomogeneous distribution in particular the inner parts of the tracking station around the beam pipe will be exposed to radiation levels up to 1×10^{14} $n_{eq}cm^{-2}$. The emerging STS engineering design is shown in the right panel of Fig. 1.

Within this study, investigations on the data rates produced by the STS, the performance of prototype front-end electronics and prototypes of an STS detector module were conducted. Results from the studies have been included in the CBM STS Technical Design Report [8], submitted to FAIR in December 2012.
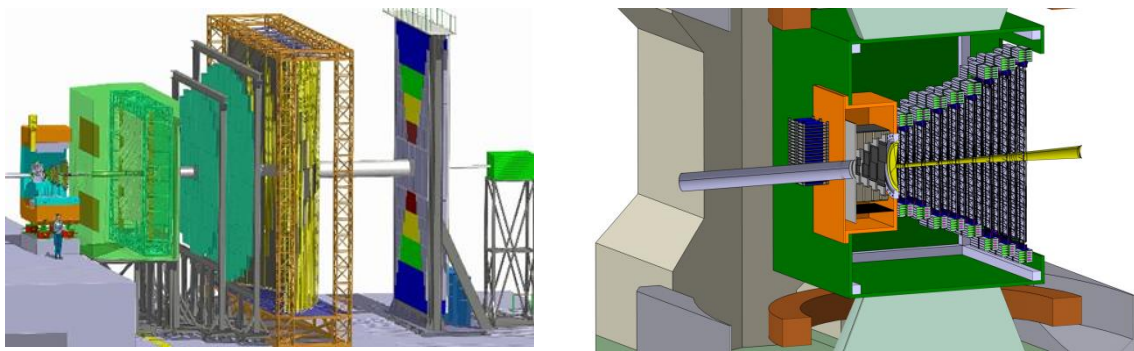

Fig. 1: Schematic view of the CBM experiment in electron-hadron configuration: Dipole magnet with the Silicon Tracking System, RICH, TRD, TOF, ECAL and PSD detector systems (left). Emerging engineering design of the Silicon Tracking System shown in the dipole magnet (right).

Self-triggering front-end electronics

In high interaction rate experiments a situation when the data rate temporarily exceeds available bandwidth can occur. In conventional triggered systems these overload situations are handled with common dead time mechanisms which discards fraction of the events. With self-triggering front end electronics such overload situations would lead, without further measures, to uncontrolled data losses and potentially a large number of incomplete events. Thus investigations on the occurrence of such situations and expected data rates were needed and performed using the FAIRRoot/CBMRoot [9] framework in simulation studies. The main problem in terms of data load comes from delta-electrons produced during collisions. The magnetic field of 1 T in which the STS will be operated turns low energy delta-electrons back to the last stations where they overload most of the detectors. This is shown in Fig. 2. Shielding of these delta-electrons is therefore needed.
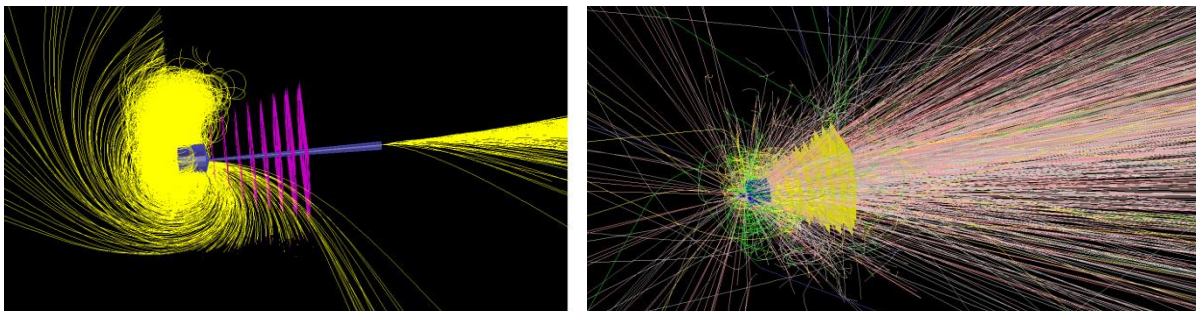

Fig. 2: Paths of delta-electrons (left) and collision products (right) in the STS.

In simulations a cut at 30 MeV was implemented. This value is relates to the radius of the path of delta-electrons which still do not interact with the first station (30 cm from the target) and thus can be removed from the active area. Afterwards the load per chip (hit rate per chip) was calculated. Hit rate within one chip is mostly at MHz level but some of the chips will have to sustain up to 100 MHz data rate which comes mainly from fast (high energy) delta-electrons. The results are illustrated in Fig. 3.
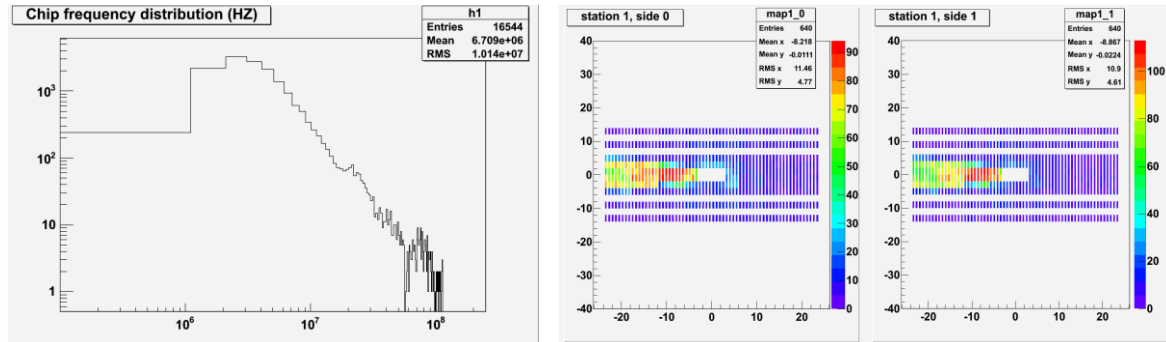

Fig. 3: Amount of chips with their data load (left) and chip-by-chip distribution of the data load for the most upstream STS station.

For early prototyping of CBM detectors the self-triggering n-XYTER chip [10] has been used. The chip was originally developed for neutron physics experiments. A schematic diagram of the chip is shown in Fig. 4.
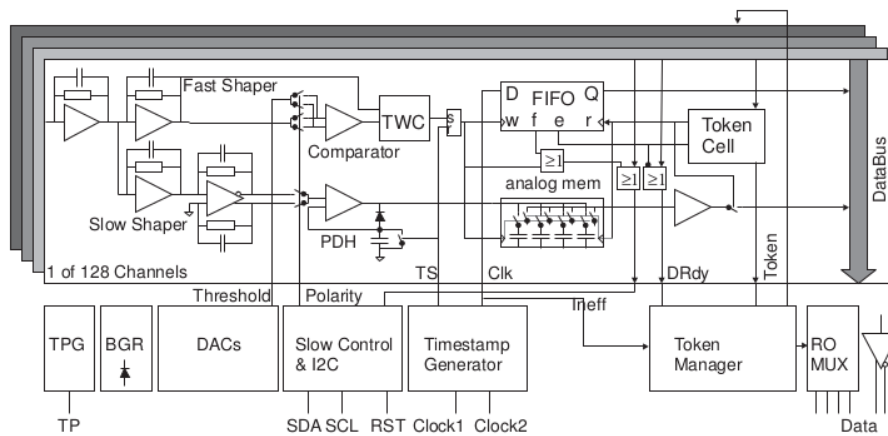
Fig. 4: Diagram of the n-XYTER architecture.

The energy calibration of such electronics is important for further evaluation of the detector performance. Calibration was obtained from a known voltage step pulse over a capacitor, created with an external pulse generator. The amount of charge in a pulse Q in this case is given by the product of coupling capacitance and voltage step amplitude, and the pulse duration equals to the transition time of the voltage step. To generate charge pulses as low as 1 fC a very small coupling capacitance (1 pF) and very small voltage steps (about 1 mV) are required. The result of the calibration for negative and positive signals is given in Fig. 5.
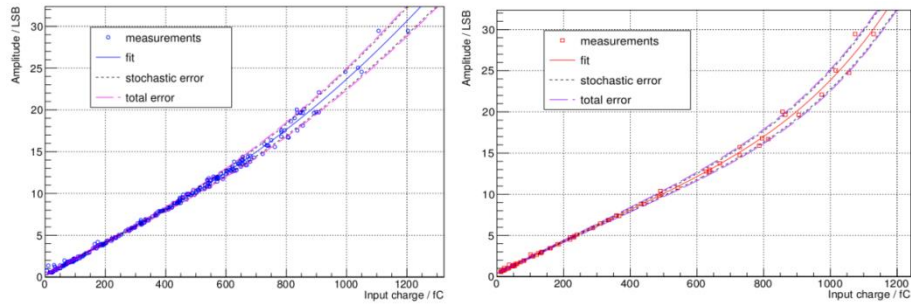
Fig. 5: ADC energy calibration of n-XYTER electronics for negative and positive signal.

Prototype measurements

For first beam tests of the system the CBM02 detector with an area of 1.5×1.5 cm^2 was used. It consists of double-sided 300 μm thick detectors with 256 strips at 50 μm pitch on both sides and a stereo-angle of 90°. The tested system, shown in Fig. 6, consisted of 3 stations with one detector each. During the test with a 2.4 GeV proton beam at the Cooler Synchrotron (COSY) in Jülich (see Fig. 6) the tracking performance and spatial resolution were measured. Results are shown in Figs. 7 and 8. One of the stations was populated with sensors irradiated to different neutron fluences between 1×10^{11} and 1×10^{14} n_{eq}cm^{-2} for radiation hardness studies. The noise in the system was at a level of 500 e$^-$.

Fig. 6: Station with detector and electronics (left), 3 stations in the JESSICA cave at COSY (right).

Fig. 7: Beam spots measured by the detectors stations.

9

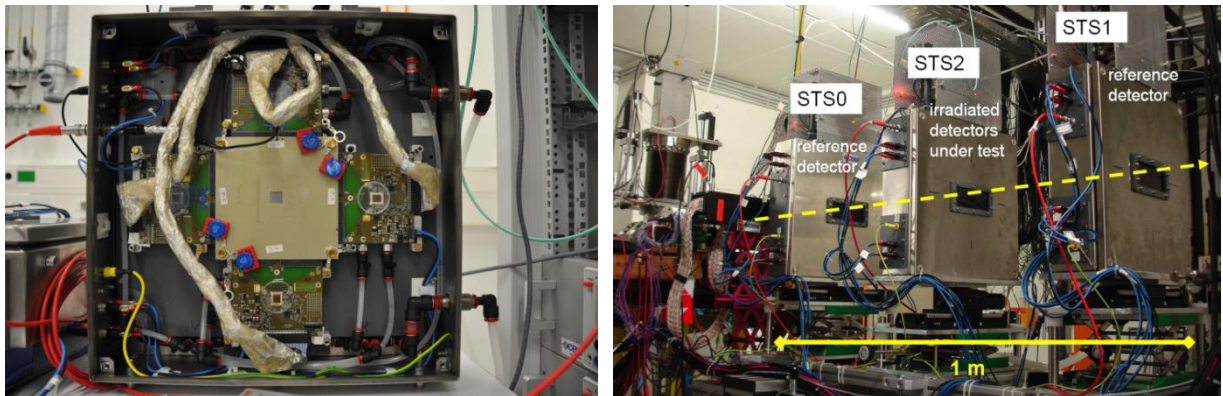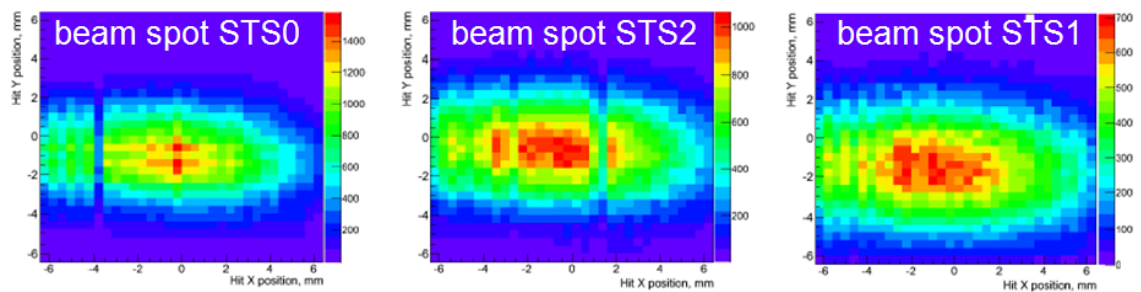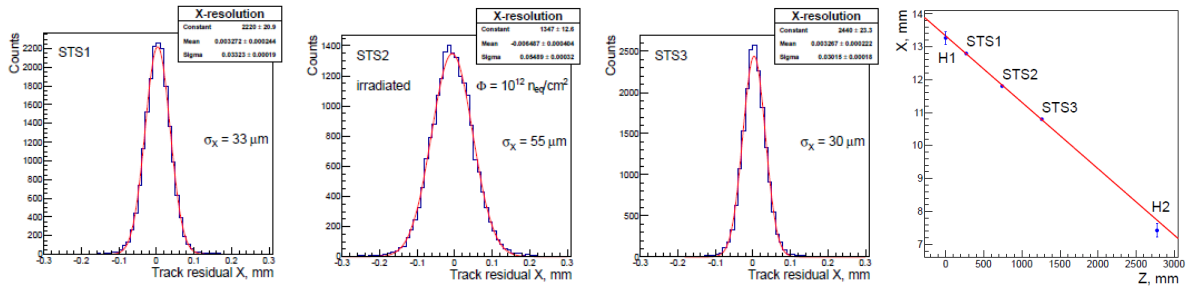**Fig. 8: Examples of the spatial resolutions achieved. Shown are the track residuals (in one of the transverse coordinates) for all three stations, and one track drawn through the three silicon tracking stations and two scintillating fiber hodoscopes (x-z projection).**

After the beam test the first prototype module assembled with CBM01 sensors (area 5.3 × 5.3 cm^2), read-out cables and read-out electronics was tested in the lab at GSI. The noise performance and the dependency of the charge collection efficiency on the length of the read-out cable were investigated. A picture of the prototype and the experimental results are given in Figs. 9 and 10.
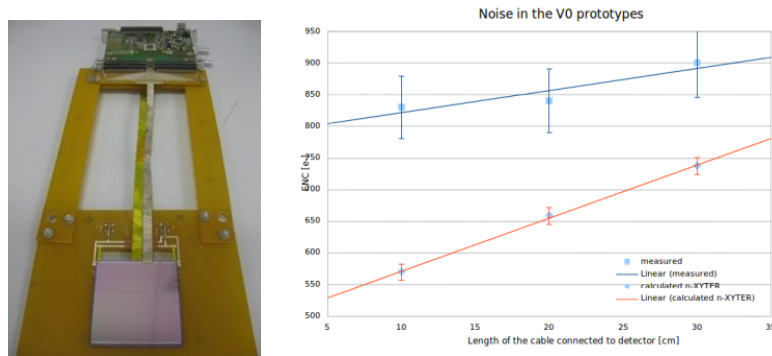
Fig. 9: Photo of the prototype module, comprising a CBM01 prototype sensor, two aluminum-polyimide read-out cables of 128 channels each, and two n-XYTER front-end boards (left) and noise performance (right) as function of the read-out cable length.
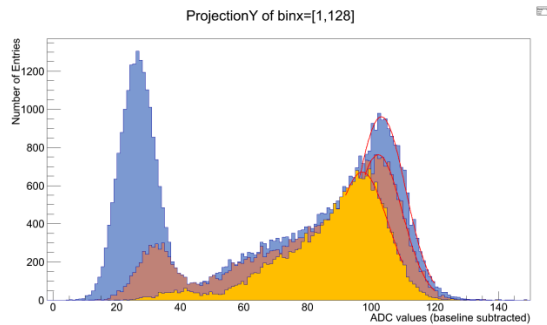
Fig. 10: Signal amplitude distributions from an ^{241}Am source in prototype modules with read-out cables of 10 (blue), 20 (red) and 30 cm (yellow) length. The peaks at low ADC values are represent system noise, detected at zero threshold (forced trigger). In self-triggering operation, the thresholds are adjusted above the noise.

Different lengths of cables were investigated – namely 10 cm, 20 cm and 30 cm. The noise performance shows a low level of equivalent noise charge which will allow putting a global threshold for the STS below 4 ke$^-$ (one of the requirements for achieving sufficiently high spatial resolution and tracking efficiency). In the ideal case (24 ke$^-$ signal per strip) the achieved signal to noise ratio in system would be above 20. The charge collection efficiency, measured with a ^{241}Americium gamma source, drops from 89% for a system with a 10 cm long cable to 83% for a system with a 30 cm long cable which is as expected from the performed calculations.

References

[1] M. Moll, PhD thesis, University of Hamburg, DESY-THESIS-1999-040 (1999) ISSN 1435-8085

[2] J. Haerkoenen et al., Nuclear Instruments and Methods in Physics Research Section A: Accelerators, Spectrometers, Detectors and Associated Equipment, Volume 579, Issue 2, 2007, Pages 648-652

[3] A. Affolder et al., Nuclear Instruments and Methods in Physics Research Section A: Accelerators, Spectrometers, Detectors and Associated Equipment, Volume 612, Issue 3, 2010, Pages 470-473

[4] N. Pacifico, PhD thesis, University of Bari, 2012

[5] The RD50 collaboration: www.cern.ch/rd50

[6] G. Kramberger et al., Investigation of Irradiated Silicon Detectors by Edge-TCT, IEEE TNS 57(4), 2294 (2010)

[7] The CBM Experiment, http://www.fair-center.eu/for-users/experiments/cbm.html

[8] STS Technical Design Report, December 2012, submitted to FAIR

[9] http://fairroot.gsi.de/

[10] A. S. Brogna et al., Nuclear Instruments and Methods in Physics Research Section A: Accelerators, Spectrometers, Detectors and Associated Equipment, Volume 568, 2006, Pages 301-308

Project Coordinator : Tilman Rohe, PSI

Jennifer Sibille, ESR, PSI. Supervisor: Tilman Rohe.

Jiaguo Zhang, ESR, UHH. Supervisor: Robert Klanner.

INTRODUCTION

Silicon detectors are used in nuclear and particle physics since the 1960s. However, the real breakthrough came in the early 1980s when micrometer position resolution for charged particle has been achieved and their superior performance for tracking down short-lived particles in particle-physics experiments demonstrated. Since then silicon detectors also found many applications outside of particle physics. Most prominent are the applications of silicon pixel detectors for X-rays in astronomy and at synchrotron radiation sources. New accelerators, in particular the luminosity upgrade of the LHC (HL-LHC) and the European X-ray Free Electron Laser (European XFEL), will lead to much higher beam intensities and enormous data rates. This requires new techniques in data processing, i.e. the development of more complex readout electronics using micro-electronic technologies with smaller feature size. In addition, the high radiation doses damage the silicon crystal and the SiO_2 surface, change the sensor properties, and limit their life time. The topic of P2 was the study of radiation damage with the aim to develop radiation-hard silicon pixel sensors for use in the harsh radiation environments of the HL-LHC and the European XFEL.

The radiation damage mechanisms in particle physics and photon science differ. While in the former the degradation is caused by defects in the silicon crystal itself (bulk damage), in the latter it is the ionization in the covering SiO_2-layers (surface damage). In order to account for both kinds of radiation damage the project was split into two sub-projects: At the PSI the ESR studied the degradation of pixel sensors caused by irradiation with charged hadrons, and at the University of Hamburg the ESR investigated the X-ray-surface damage. This collaboration with frequent visits further strengthened the close links between the two institutes. Both are members of the CMS collaboration at the CERN LHC and build together the upgrade of the present CMS pixel detector, and both collaborate on the development of the AGIPD instrument for the European XFEL.

SILICON PIXEL DETECTORS FOR EXPERIMENTS AT LHC

The central feature of the Compact Muon Solenoid (CMS) apparatus is a superconducting solenoid. The silicon tracker, the electromagnetic calorimeter (ECAL), and the hadron calorimeter (HCAL) are contained within the solenoid. Muon detectors are embedded in the steel return yoke. The CMS apparatus has an overall length of 22 m, a diameter of 15 m, and weighs 12,500 tons. In addition to the barrel and end cap detectors, CMS has extensive forward calorimetry. A more detailed description of CMS can be found elsewhere [1].

The CMS pixel detector consists of silicon sensors and readout chips (ROC), which are bump bonded together. The sensor of the barrel part of the pixel detector (BPIX) is made from 285 μm thick diffused-oxygen float-zone (DOFZ) silicon, as oxygen-enriched silicon has been shown to have superior radiation hardness [2]. They were produced by CiS, using silicon with the ⟨111⟩ orientation and a resistivity of 3.7 kΩ·cm [3], resulting in a depletion voltage of 50-60 V. The n^+-in-n sensors consist of highly doped n^+-implants in an n-type substrate, and the p^+n junction on the backside along with a multiple guard ring structure. This design requires double-sided processing, which increases the cost, but allows the edges of the sensor to be at ground potential so that the detector can be operated at high bias voltages (up to 600 V). The pixels have a size of 150×100 μm^2. A

photograph of four adjacent pixels is shown in Figure 1. The n-type pixels were chosen in order to collect electrons, which have a higher mobility than holes. This reduces the effects of charge trapping, and thereby ensures a substantial signal even after high hadron fluences. More details about the design and construction of the pixel detector can be found elsewhere [1, 4].

For 2016 an upgrade of the CMS pixel detector is foreseen. A reduction of the radius of the innermost layer as well as an increase of LHC luminosity will lead to an increase of the radiation damage. The innermost pixel layer is specified to remain operational for an integrated luminosity of at least 250 fb^{-1} which translates to a fluence of about 1.5×10^{15} n$_{eq}$/cm^2. In contrast to photon science the radiation damage in particle physics are dominated by bulk effect dominantly caused (in the case of the CMS pixel detector) by charged pions. The macroscopic changes
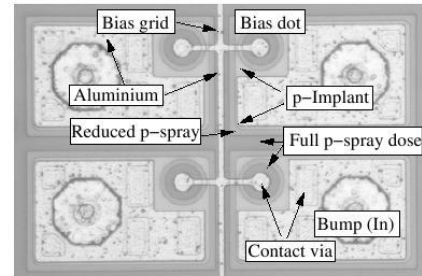

Figure 1: Top view of the n$^+$ side of the CMS pixel sensor.

are an increase of the leakage current and of the electric field, both requiring a higher operating voltage, and charge trapping causing a loss of signal. In order to investigate if the CMS barrel pixel sensors stay operational for its projected life time, and to study the degradation of charge collection, a number of samples consisting of a small sensor bump bonded to a single ROC were prepared. Some of the samples were irradiated to fluences between 4×10^{14} and 5×10^{15} n$_{eq}$/cm^2 to investigate how the properties of the sensor change with increasing fluence. The samples were irradiated after the ROCs were bump-bonded to the sensors.

Charge collection efficiency

The charge collection efficiency of an irradiated sensor is defined as the ratio of amount of charge collected from a minimum ionizing particle (MIP) in the irradiated sensor compared to the amount of charge collected from a MIP in an unirradiated sensor. As a reference several unirradiated sensors were tested under the same conditions as the irradiated sensors. The test setup consisted of an insulated cold box with dry nitrogen flow, a sensor and ROC sample, a ^{90}Sr β-source, and the electronics to read out the signal. The endpoint energy of the β particles is about 2.3 MeV, which pass through the sample and approximate a MIP.

The measurements were done at approximately - 20 $^{\circ}$C. A current-voltage (IV) curve was taken for each sample to ensure that it was working properly. Then the bias voltage was scanned through a range of values, starting from well below the depletion voltage, and ending well into the depletion plateau. At each bias voltage value, data was collected for 15 seconds using random triggers.

The charge deposited in a silicon sensor is described by a Landau distribution, while the measurement error introduces a Gaussian. Therefore, the measured charge distributions were fit by a Landau curve convoluted with a Gaussian. Figure 2 shows a typical fit. This distribution was fit to the measurement for each applied bias voltage. The peak value, which is the most probable value, was taken as the charge collected in the sample by a MIP at that voltage. The fluences to which the samples were irradiated ranged from 4×10^{14} to 10^{15} n$_{eq}$/cm^2, which represent the number of particles accumulated at the LHC for an integrated luminosity of 130 fb^{-1} (in the present inner pixel barrel layer) to about 750 fb^{-1} (in the upgraded detector). Presently it is foreseen to replace the innermost pixel layer after accumulating an integrated luminosity of 250 fb^{-1}. The most probable value of the signal as a function of fluence for each sample at a bias voltage in the plateau region is shown in Figure 3. The decrease in the total collected charge due to charge trapping with increasing fluence is clearly visible, but there is still a substantial signal at fluences on the order of 10^{15} n$_{eq}$/cm^2, provided that a high bias voltage can be applied. In CMS the limiting factors in the bias voltage are the cables and connectors to supply the voltage

to the sensors. These measurements show that the lifetime of the sensors is not limited by the amount of charge collected, but by the reduction in the spatial resolution due to the increase in bias voltage needed [5]. Two samples irradiated to $5\times10^{15}\,n_{eq}/cm^2$ were tested. The amount of charge collected for these samples is at the nominal threshold level, and does not seem to change with bias voltage. As the hit detection efficiency was strongly reduced in this samples we believe that the peak of the Landau distribution is below the threshold of the ROC. It is demonstrated that the sensor and ROC can be operated after such a high fluence, but a bias voltage of 600V is not sufficient.
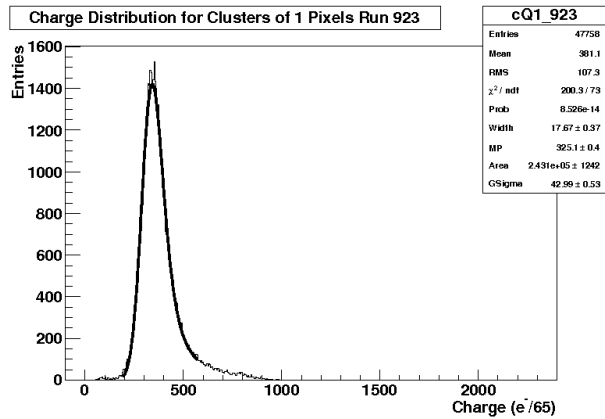

Figure 2: Example of a measured charge distribution fit by a Landau distribution convoluted with a Gaussian.
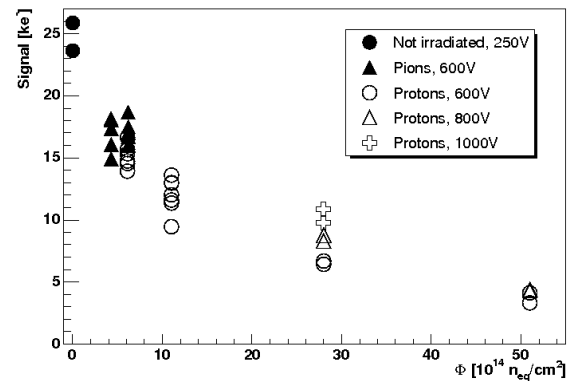
Figure 3: Most probable value of the signal for MIPs as function of fluence for each sample at a bias voltage in the plateau region.

Inter-pixel capacitance

The capacitance between individual pixels and their neighbours influences the noise and the cross-talk in the sensor, and has an impact on the analog power of the ROC. The capacitance depends on the gap between pixels. Pixels with a larger gap have a smaller inter-pixel capacitance, but a less homogeneous drift field in the sensor. Therefore it is important to find an optimum between capacitance and gap size.

The current CMS-barrel pixel sensors have small gaps (20 μm), and accordingly a relatively high inter-pixel capacitance. In order to test whether reducing the inter-pixel capacitance by increasing the gap would be beneficial, several samples were produced with a gap of 30 μm, hereafter referred to as "gap-30". The inter-pixel capacitance was measured as function of bias voltage for both the standard and the gap-30 samples. As the capacitance is mostly affected by changes of the surface properties, the samples were then irradiated with a ^{60}Co γ-source and measured again.

The small value of the capacitance, combined with the small pixel size, makes measuring the inter-pixel capacitance a challenge. A new method to measure the inter-pixel capacitance was developed: a simple chip was bump bonded onto the sensor instead of the ROC. This chip is referred to as the "readout-replacement chip." The concept of the measurement method is to form a basic unit cell of one pixel surrounded by the eight adjacent pixels, which are connected together. Then the capacitance can be measured between the central pixel and the eight connected neighbour pixels. This basic unit is repeated over the entire chip. The central pixels of each cell are connected together and routed to a pad on the edge of the chip. The eight neighbouring pixels of each cell are also connected together over the whole chip and routed to a second pad on the edge of the chip. These two pads can be contacted, and the capacitance can be measured.

The results of the measurements are shown in Figure 4. The solid lines are the measurements of the samples before irradiation, and the dashed lines the measurements of the samples after irradiation. The capacitance of the gap-30 samples is indeed lower than the capacitance of the standard samples. The inter-pixel capacitance after irradiation is lower than before irradiation. This is likely due to the build-up of positive charges at the surface after irradiation. This layer of positive charges begins the depletion of the p-spray earlier than in the unirradiated samples, so the capacitance decreases faster. It was found that the larger gap size did not have any substantial impact on the noise or crosstalk, so the gap size remains unchanged for the sensors for the Phase 1 upgrade of the CMS pixel detector.
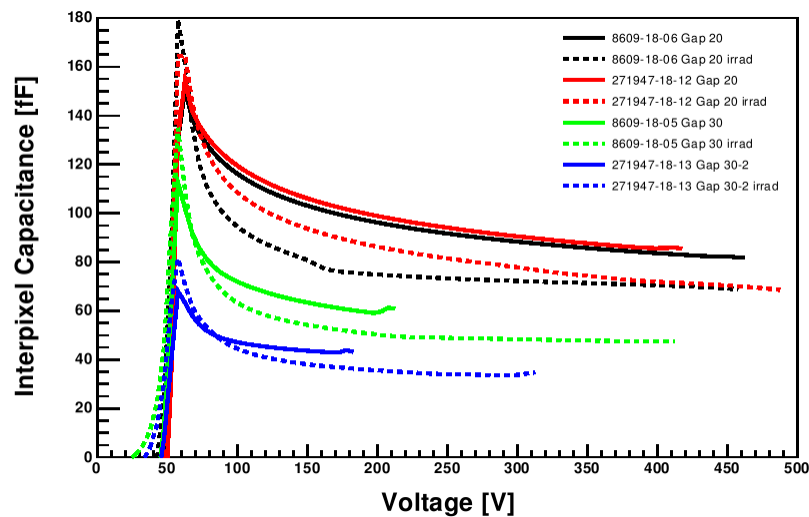

Figure 4: Measurements of inter-pixel capacitance as a function of voltage. Solid lines: Results obtained before irradiation. Dashed lines: Results after irradiation.

Conclusions on silicon detectors for experiments at the LHC

The MCPAD project allowed for a study of the radiation induced degradation of the sensor performance of the CMS barrel pixel sensors. It was found that the life time of the detector will not be limited by the decrease of charge collection efficiency. In addition, a novel method of measuring the capacitance of the single sensing elements, the pixels, has been developed. It was shown that it is possible to considerably decrease the capacitive load on the read out electronics by increasing the gaps between the pixel implants.

SILICON PIXEL SENSORS FOR THE EUROPEAN XFEL

The European X-ray Free Electron Laser (XFEL), planned to be operational in 2015, will provide fully coherent shorter than 100 fs long X-ray pulses, each with up to 10^{12} 12 keV photons. The high brilliance of the XFEL poses unprecedented requirements for the detection systems: a dynamic range from single 12 keV photons to 10^{5} photons deposited in less than 100 fs, a time between XFEL pulses of 220 ns, and radiation doses up to 1 GGy for 3 years of operation [6]. To optimize sensors for these requirements demands a good understanding of the radiation damage caused by X-rays, which was the main aim of this part of P2.

X-ray radiation damage

There are two kinds of radiation damage: bulk damage and surface damage. The former is due to the non-ionization energy loss (NIEL) of incident particles, i.e. protons, neutrons, electrons and high-energy gamma-

rays, which damage the silicon crystal; the latter is due to the ionization-energy loss of charged particles or X-rays, which causes the build-up of positive charges and traps in the SiO_2 and at the Si-SiO_2 interface. The threshold energy for X-rays to cause bulk damage is about 300 keV. Therefore, the main damage in silicon sensors at the European XFEL, where a typical energy is 12 keV, is surface damage.

The mechanisms of surface damage are as follow: X-rays (or charged particles) produce electron-hole pairs in the SiO_2. Depending on the strength of the electric field in the SiO_2 and the type of incident particle, a fraction of the electrons and holes recombine. The remaining electrons and holes either drift to the electrode or to the Si-SiO_2 interface where they are captured by oxygen vacancies (most of the vacancies locate in the SiO_2 close to the Si-SiO_2 interface) and form trapped positive oxide charges. During the transport of holes, some react with hydrogenated oxygen vacancies resulting in protons. Those protons, which drift to the interface, break the hydrogenated silicon bonds at the interface and produce dangling silicon bonds, namely interface traps with energy levels distributed throughout the band gap of silicon. The energy levels close to the mid-gap of silicon cause the surface current.

The main parameters related to the surface damage are the oxide-charge density, N_{ox}, the interface-trap density, N_{it}, and the surface-current density, J_{surf}. To extract N_{ox} and N_{it}, capacitance/conductance-voltage (C/G-V) and thermal dielectric relaxation current (TDRC) measurements have been performed on MOS capacitors. The measured TDRC signal, I_{tdrc}, as function of temperature, T, allows determining the distribution of the density of interface states, $D_{it}(E_{it})$, in the silicon band gap [7]. The total density of interface traps, N_{it}, can be estimated by integrating the TDRC signal divided by the heating rate β and the elementary charge q_0: $N_{it} = \frac{1}{\beta \cdot q_0} \int I_{tdrc}(T) dT$. To extract the oxide-charge density, N_{ox}, a model describing the irradiated MOS capacitor by an RC-network is used. The model allows calculating the capacitance and conductance of a MOS capacitor as function of gate voltage for different frequencies using as input D_{it} from the measured TDRC signal and N_{ox}. N_{ox}, which just shifts the C/G-V curves along the voltage axis, is obtained by adjusting its value till the calculated C/G-V curves describe the measurements. Figure 5(a) shows the comparison of the measured to the calculated C/G-V curves (parallel mode) of a MOS capacitor irradiated to 5 MGy after annealing for 120 minutes at 80 °C for frequencies between 1 kHz and 100 kHz. The model has been described in detail in [8]. In the model calculations, all interface traps within the silicon band gap are assumed to be acceptors, which gives the maximal estimate for the oxide-charge density induced by X-rays.
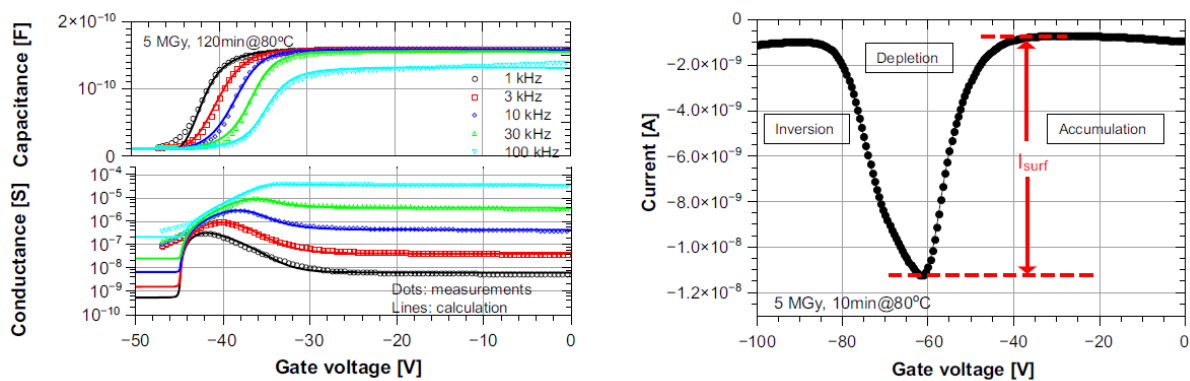
Figure 5: C/G-V and I-V curves of irradiated MOS capacitors and gate-controlled diodes. (a) Comparison of the measured and calculated C/G-V curves (parallel mode) of a MOS capacitor irradiated to 5 MGy for frequencies between 1 kHz and 100 kHz using the model described in [8]. The extracted values of N_{ox} and N_{it} are both 2.5×10^{12} cm^{-2}. (b) I-V curve of a gate-controlled diode irradiated to 5 MGy annealed at 80 °C for 10 minutes. The figures shown have been published in [9].

To determine the surface-current density, J_{surf}, current-voltage I-V measurements have been done at room temperature for the gate-controlled diodes. Figure 5(b) shows the I-V curve of a gate-controlled diode irradiated to 5 MGy after annealing for 10 minutes at 80 °C. The surface current, I_{surf}, is extracted from the

"maximum" current measured in depletion of the 1st gate ring and the average value of the currents obtained in accumulation. The measured surface current has a strong dependence on temperature. At room temperature its value changes by about 8 % for a temperature change of 1 ^{o}C. All measured surface currents have been scaled to 20 ^{o}C using the scaling formula discussed in [9]. The surface-current density, J_{surf}, is calculated from the surface current scaled to 20 ^{o}C and the area of the 1st gate ring: $J_{surf} = I_{surf}/A_{gate}^{1st}$.
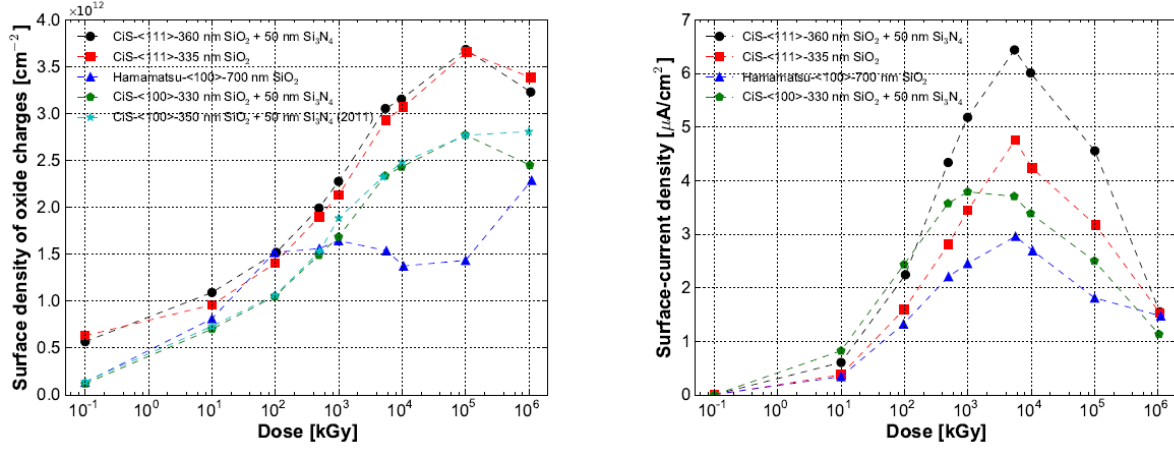

Figure 6: Dose dependence of the oxide-charge density N_{ox} and the surface-current density J_{surf} scaled to 20 ^{o}C after annealing at 80 ^{o}C for 10 minutes. (a) N_{ox} vs. dose. (b) J_{surf} vs. dose. The figures shown have been published in [9].

From the dose dependence of the oxide-charge density N_{ox} and the surface-current density J_{surf} it is found that: (1) N_{ox} and J_{surf} for <100> silicon are lower than that for <111> silicon. (2) Little difference in N_{ox} is observed for the MOS capacitors with an insulating layer made of SiO_2 and one made of SiO_2 and Si_3N_4. (3) The values found for samples fabricated by CiS and Hamamatsu differ by a factor of 2, which indicates some dependence of radiation-induced defects on crystal orientation and technology. (4) N_{ox} and J_{surf} either saturate or even decrease at high irradiation doses.

Optimization and design of the AGIPD sensor

One of the detector projects under development for the XFEL is the Adaptive Gain Integrating Pixel Detector (AGIPD), which is a collaboration of DESY, PSI, Bonn University and Hamburg University. The Hamburg group is responsible for the AGIPD sensor. To meet the challenges and requirements for the XFEL the specifications for the AGIPD sensor, listed in table 1, have been defined.

Parameter	Value
Pixel size	200 μm × 200 μm
Thickness	500 μm
Type	p$^+$-n
Bulk resistivity	3 - 8 kΩ·cm
Full depletion voltage	< 200 V
Nominal operating voltage	> 500 V
Inter-pixel capacitance	< 0.5 pF
Leakage current	< 1 nA/pixel

Table 1: Specifications of the AGIPD sensor.

Based on the radiation-damage studies, the extracted parameters related to the surface-radiation damage have been used as input for Synopsys TCAD simulations with the aim to optimize the sensor performance. The parameters which have been optimized in the design of the sensor to fulfil the specifications of table 1 are

inter-pixel gap, metal overhang, curvature of the p$^+$-implants, thickness of the oxide, junction depth and guard ring layout. For the simulation results, we refer to [10].

Parameter	Value
Pixel size	200 μm
Gap	20 μm
Metal overhang	5 μm
Radius pixel implant	10 μm
SiO$_2$ thickness	250 nm
No. guard rings	15
Distance last pixel to cut edge	1,200 μm
Bulk resistivity	5.1 kΩ·cm
Junction depth	2.4 μm

Table 2: Geometrical parameters based on simulation results.

Table 2 shows the optimized parameters and their values for the AGIPD sensor. The optimized values have been used in the sensor layout design, and the sensors are presently fabricated by SINTEF.

Conclusion on silicon pixel sensors for the European XFEL

Within P2 studies on surface radiation damage have been performed: Results on the oxide-charge density and the surface-current density from MOS capacitors and gate-controlled diodes built on high-resistivity n-type silicon with orientations <100> and <111> produced by two vendors, CiS and Hamamatsu, as function of X-ray doses up to 1 GGy have been determined. In addition, the influence of the electric field in the oxide on the formation of oxide charges and interface traps, and the annealing of the X-ray induced oxide charges and the surface current due to interface traps have been studied. The main results are published in [9]. Based on the damage-related parameters, an optimized layout of the AGIPD sensor has been designed [10].

CONCLUSIONS

The aims of P2, determine up to which maximum radiation dose the CMS pixel sensors deliver adequate signals, and investigate X-ray radiation damage of silicon sensors in a new dose regime, have been achieved. The results obtained provide essential information for the phase I upgrade of the CMS pixel detector, and are the basis of the design of the pixel sensors for the AGIPD instrument at the European XFEL.

In addition to achieving the important scientific goals which are the bases of the PhD theses of the two researchers, the ITN MC-PAD provided a unique educational experience for both researchers and supervisors. The generous support by the European Union through the Marie-Curie Program is warmly acknowledged.

References

[1] The CMS Collaboration, *The CMS experiment at the CERN LHC*, JINST **3** (2008) S08004.

[2] M. Moll, *Radiation damage in silicon particle detectors – microscopic defects and macroscopic properties*, *PhD thesis University of Hamburg*, **DESY-THESIS-1999-040** (1999) ISSN 1435-8085.

[3] Y. Allkofer et al., *Design and performance of the silicon sensors for the CMS barrel pixel detector*, *Nucl. Instr. Meth.* A **584** (2008) 25-41.

[4] S. Koenig et al., *Building CMS pixel barrel detector modules*, Nucl. Instr. Meth. A **582** (2007) 776-780.

[5] A. Dorokhov et al., *Tests of silicon sensors for the CMS pixel detector*, Nucl. Instr. Meth. A **530** (2004) 71-76.

[6] H. Graafsma, *Requirements for and development of 2 dimensional X-ray detectors for the European X-ray Free Electron Laser in Hamburg*, JINST **4** (2009) P12011.

[7] J.G. Simmons and G.W. Taylor, *Dielectric Relaxation and Its Effects on the Thermal Electric Characteristics of Insulators*, Phys. Rev. B**6** (1972) 4804-4814.

[8] J. Zhang et al., *Study of radiation damage induced by 12 keV X-rays in MOS structures built on high resistivity n-type silicon*, J. Synchrotron Rad. **19** (2012) 340-346, arXiv: 1107.5947.

[9] J. Zhang et al., *Investigation of X-ray induced radiation damage at the Si-SiO$_2$ interface of silicon sensors for the European XFEL, accepted for publication in JINST*, arXiv: 1210.0427.

[10] J. Schwandt et al., *Optimization of the radiation hardness of silicon pixel sensors for high X-ray doses using TCAD simulations*, JINST **7** (2012) C01006, arXiv: 1111.4901.

PROJECT 3: RADIATION HARD CRYSTALS/3D DETECTORS

Project Coordinator: Robert Klanner, University Hamburg

Marko Milovanović, ESR, Jozef Stefan Institute, Ljubljana, Supervisor: Gregor Kramberger

Cristina Pirvutoiu, ESR, University of Hamburg, Supervisor: Robert Klanner

Roxana Radu, ESR, University of Hamburg, Supervisor: Robert Klanner

INTRODUCTION

Since the early 80-ies position-sensitive silicon detectors have found many applications in science, as well as in technical and industrial applications. Today practically all large particle-physics experiments depend heavily on this technology. For their use in future high energy physics experiments, like in the HL-LHC, the high-luminosity option of the CERN LHC, radiation damage is presently the main limitation. The expected fluences of up to 10^{16} hadrons/cm^2 by far exceeded the radiation hardness of silicon sensors at the time the proposal was submitted.

Radiation damage causes three effects: An increase in dark current, resulting in noise and power dissipation, an increase in required operating voltage, causing practical problems, and charge trapping, resulting in signal reduction. There are two strategies to improve the radiation hardness of silicon sensors:

(1) Defect engineering, the intentional introduction of impurities into the silicon crystal.

(2) Design engineering, the choice of a design, which minimizes or overcomes the deterioration due to radiation damage.

Within P3 both approaches have been pursued and significant progress has been achieved. For defect engineering, first of all, the radiation-induced defects and their properties have to be understood. The studies aim at understanding the differences between point and cluster defects. With respect to design engineering, the electric field in the sensors and the charge collection has been measured using the novel technique "Edge-TCT" and the phenomenon of charge multiplication, has been investigated. In addition, the performance of the newly developed 3-D sensors for different irradiation doses has been characterized.

RADIATION-INDUCED POINT AND CLUSTER DEFECTS

It is well known that the causes of radiation damage are radiation-induced isolated point defects (silicon vacancies and impurities) and extended cluster defects (high density of vacancies). Whereas there is quite some knowledge about point defects [1], cluster defects are poorly understood. 1 MeV electrons produce only point defects, whereas at 15 MeV cluster defects dominate. Thus a comparative study of defects induced by electron irradiation with different energies allows investigating separately point and cluster defects. In order to identify the most radiation-hard material we have irradiated test structures fabricated on silicon crystals with different impurities and production techniques with electrons with energies between 1 and 15 MeV.

Two kinds of investigations were performed: electrical characterization of the irradiated sensors by their I-V, C-V characteristics, and spectroscopy of electrically active defects by the DLTS and TSC methods. These techniques allow to characterize the irradiated sensors with respect to their macroscopic and microscopic properties and to understand the consequences of defect generation on sensor performance. While the defect

generation depends on the electron energy and thus the identification of the defect type (point or cluster defects) is possible directly after irradiation, structure identification requires annealing studies at elevated temperatures. Therefore annealing experiments were done: at 80^0C for a direct correlation of the defect generation/transformation with sensor performance for the operating conditions of LHC experiments, and at temperatures above 80^0C, to follow the defect kinetics with respect to the impurity content. These studies bring information about the defect reactions and thus information about the chemical structure of the defects.

Comparative studies of the defects induced by electrons with energies of 1.5, 3.5, 6 and 15 MeV were done. High-resistivity n-type silicon with different carbon and oxygen concentrations was chosen: Standard Float Zone (STFZ), Diffusion-Oxygenated Float Zone (DOFZ) and Epitaxial Silicon on a Czochralski substrate (EPI). To characterize the macroscopic properties of the diodes built from these materials, the Current-Voltage (IV for information on dark current and homogeneity of current-generating defects) and the Capacitance-Voltage characteristics (CV for determining the depletion voltage, V_{dep}, and the capacitance at full depletion, C_{end}, for evaluating the sensor thickness and effective doping concentration) were measured.
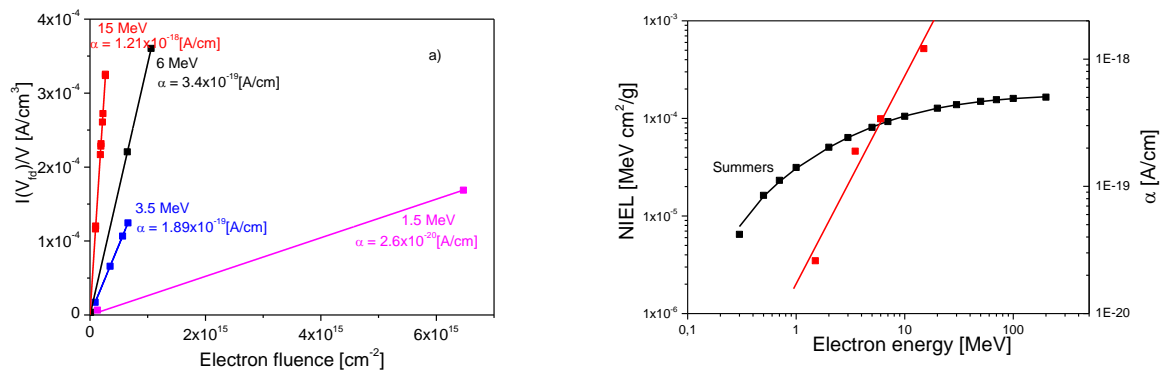

Figure 1. (a) Fluence dependence of dark current from EPI-ST (electron energy: 1.5 MeV) and DOFZ (3.5, 6, and 15 MeV) directly measured after irradiation. The values of the current-damage constant α are indicated.   (b) Comparison of the electron-displacement damage α with NIEL values as function of electron energy.

The IV/CV characteristics were measured at room temperature at a frequency of 10 kHz. The measured dark current was scaled to 20^0C. As seen in Fig. 1 a, the dark current increases proportional to the fluence, and the proportionality factor α has been determined. α shows a strong increase with energy. In Fig. 1 b the measured values of α are compared with NIEL (Non Ionizing Energy Loss) values from [2]. NIEL is the rate of energy loss due to atomic displacements when a particle traverses a material. These displacements create energy levels in the silicon band gap, which cause the radiation-induced deterioration of the sensor properties. Fig. 1b shows that for electrons with energies in the range 1.5 to 15 MeV the classical NIEL does not describe the measurement. The reason is that primary-produced Frenkel pairs can recombine and transform in stable defect clusters. Thus the current related damage parameter α is a better estimation of the radiation damage for electrons than the classical NIEL, which does not take into account recombination processes.

Using the techniques Thermally Simulated Current (TSC) and Deep Level Transient Spectroscopy (DLTS) the following properties of the defects induced by the electron irradiation have been determined: concentration (N_T), activation energies (E_a), capture cross sections (σ), and the effective space charge concentration (N_{eff}). DLTS, based on measuring the capacitance transients with temperature, is used on samples irradiated with lower fluences. TSC, based on measuring the current released by charged defects versus temperature, allows determining the defect concentrations of medium- and highly-irradiated samples. The temperature is related

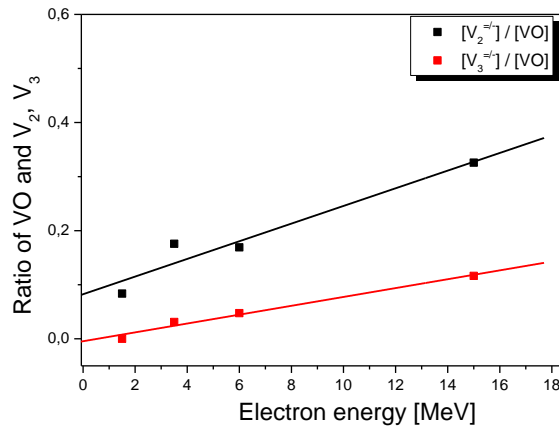to the position of the Fermi level in the band gap and thus allows determining the energy of the defects.

Figure 2. Ratio of single vacancies and di-vacancies, tri-vacancies with electron energy

Using the DLTS measurements the formation of point and cluster defects as function of electron energy was analyzed by determining the concentration ratio of the single-vacancy defect VO, the double vacancy V2 and the tri-vacancy defect complex V3 shown in Figure 2. The main damage by 1.5 MeV electrons is due to introduced point defects, which originate from primary generated interstitials and vacancies. Single vacancies (VO) are mobile at room temperature. Therefore vacancy defects will be distributed uniformly in the bulk. For 3.5 MeV electrons the recoil energy is sufficiently high to knock out secondary atoms frequently. This does not lead to more single vacancies, but di-vacancies and tri-vacancies (V2, V3) are directly generated (Fig. 2). This effect becomes more dominant when irradiating with higher-energy electrons. It results in a decrease of the VO introduction rate and an increase of V_2 and V_3. Also the direct correlation of tri-vacancies (V_3) with the dark current could be established [3, 4]. To separate the contributions of the different cluster defects to the dark current, their concentrations for different annealing steps were determined and compared with the current. By performing isothermal and isochronal annealing studies it was found, that the cluster related defect (V_3) are responsible for the increase of the dark current.
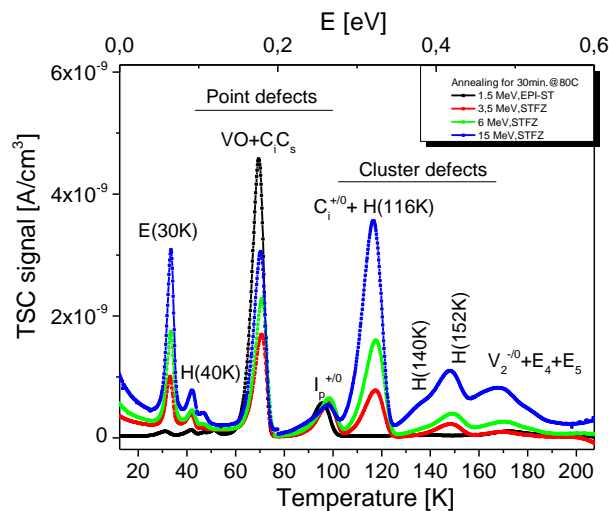

Figure 3. Results of TSC measurement after annealing for 30 Minutes at 80^{0}C after irradiation with electrons for a normalized fluence Φ = 6x10^{14} cm^{-2}. See text for a discussion of the results.

Using TSC measurements (Fig. 3) the introduction and development of cluster related deep hole traps and a shallow donor were investigated. It was found that the concentration of cluster-related deep hole traps, independent of the oxygen concentration, and of the shallow donor increase with increasing electron energy [5]. The kinetics of these defects was investigated by isothermal and isochronal annealing. Four hole traps, labeled H (116K), H (125K), H (140K) and H (152K), which are acceptors in the lower half of the silicon-band gap were measured. The concentration of the H (116K) and H (125K) defects are less visible after annealing at 80^0C, while the concentrations of the H (140K) and H (152K) defects were found to increase with annealing time and temperature, reach a maximal concentration at 180^0C, and then begin to anneal out. The time constant for the in-annealing of H (152K) was found to be $\tau = 355$ min. The influence of the donor E(30K) is known from [1]: it contributes with positive charge to the effective doping concentration. From the electron irradiations it was found that the E (30K) concentration increases with energy, which indicates that it is a cluster defect. However, the identity of these defects has not yet been clarified by experiments. They have a direct impact at room temperature on the change of the effective doping of the silicon, N_{eff}, with fluence, and determine the time evolution of N_{eff} in n-type diodes [6]. The defect studies by TSC were used to predict the annealing effects of N_{eff} and to compare the results with values determined from CV measurements at room temperature. The evolution of the defect concentrations with time after irradiation does not fully describe the annealing of N_{eff} as determined from CV measurements after electron irradiation.

We conclude: silicon diodes fabricated on different silicon crystals have been irradiated by electrons with energies between 1.5 and 15 MeV. Using microscopic defect spectroscopy (DLTS and TSC) and measurements of macroscopic properties (I/V and C/V) it has been shown that the current generation does not follow the simple NIEL scaling. As expected, it has been found that the ratio of cluster to point defects increases with electron energy. With the help of annealing studies, the relation between specific defects and macroscopic parameters, like dark current and effective doping, and the defect kinetics could be established. This understanding and further studies are important for improving the radiation hardness of silicon sensors by defect engineering.

CHARGE COLLECTION AND CHARGE MULTIPLICATION STUDIES

For the detailed experimental study of the silicon sensor properties as function of dose and type of irradiation, a novel TCT-setup (Transient Current Technique) was developed and built in Ljubljana, with edge-on laser injection (Edge-TCT [7, 8]). In addition, a setup with a ^{90}Sr source has been built that uses an Alibava multi-channel readout system having two 128 channel Beetle chips [9] with LHC speed electronics (25 ns integration time of the current pulses). Both were used to measure signals and collected charge in silicon strip sensors.

In the Transient Current Technique electron-hole pairs are created near the surface of the sensor by a short pulse (~100 ps) of a laser beam with a wavelength of ~660 nm, would have a penetration depth of a few microns in silicon, or by alpha particles. In the electric field one type of charge carriers promptly reaches the close-by electrode, while the carriers of the other type drift to the opposite electrode and induce a current which depends on the drift velocity. The current is amplified by a wide band current amplifier and recorded by an oscilloscope, for multi-TCT for several electrodes. From the time resolved current pulses the drift velocity of the charge carriers and the charge collection properties are obtained. The TCT setup can also be used with an IR-laser beam of a penetration depth larger than the sensor thickness, which creates e-h pairs with a spatial distribution similar to that of minimum ionizing particles. After irradiation to very high fluences, the charges are quickly trapped; the induced current pulse is reduced and cannot be distinguished from noise. This limits the use of TCT for the extraction of drift velocities and electric field profiles.

In the framework of P3 a new technique, called Edge-TCT (see Fig. 4), was developed, which overcomes this difficulty. A focused laser beam of infrared light (1064 nm wavelength, 40 ps pulse width, 200 Hz repetition rate and absorption length of more than 1 mm in silicon at -20˚C) illuminates the carefully polished edge of the

sensor. The electron-hole pairs are created almost uniformly along the beam. The beam position and thus the depth, at which the carriers are created, can be controlled with sub-micron precision by moving stages. The scan along the y-axis, which is perpendicular to the surface, reveals the charge-collection efficiency for a given depth in the sensor. At the beginning of the pulse the current is not yet affected by trapping and thus proportional to the drift velocities of the carriers. Thus a model independent extraction of the velocity profile is possible. Moreover, the induced charge at a given depth reveals regions of high and low charge-collection efficiency in the sensor.
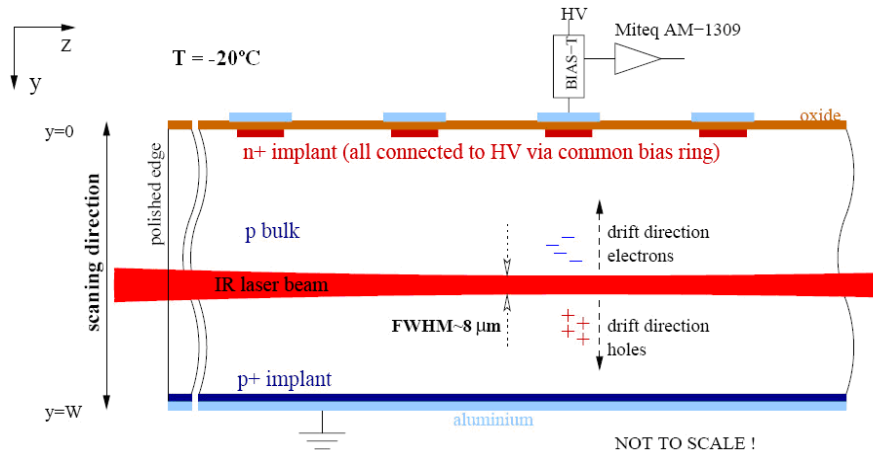

Figure 4: Schematic view of the Edge-TCT.

The measurement of the induced currents also gave the first direct observation of charge multiplication as can be seen in Fig. 5a. After the initial peak, which is due to the drift of the primary generated carriers, a second peak appears at a time which depends on the position of the beam. This peak is caused by holes which are produced by electrons which that reach the high field region close to the strips where they produce electron-hole pairs by impact ionization. The velocity profiles, shown in Fig. 5b, also demonstrate that at high operating voltages a substantial electric field is present in the entire sensor even after irradiation to high fluences.
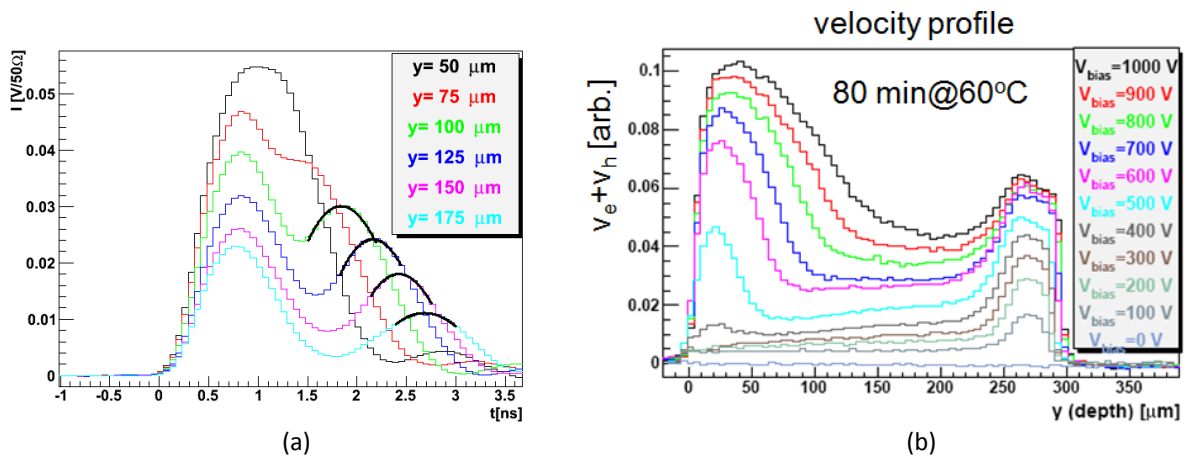

Figure 5: (a) Induced current pulses for different y positions of the laser beam in a FZ n+-p strip sensor, produced by Micron and irradiated by reactor neutrons to a fluence of Φ_{eq} = 5·10^{15} cm^{-2}. The detector was annealed for 80 minutes at 60°C and biased to 1000 V. (b) Velocity profile of the charge carriers for the same sensor.

During the course of the project systematic studies have been made with Edge-TCT on silicon strip sensors produced by Micron, Hamamatsu Photonics (HPK) and Max-Planck-Institut Halbleiterlabor (MPI/HLL), irradiated to hadron fluences of up to Φ_{eq} = 10^{16} cm^{-2}.

The most important observations are:

- Long term annealing enhances multiplication [10], for two reasons: an increase of the concentration of effective acceptors leads to a very high peak in the electric field, sufficient for initiating the charge-multiplication process, and the decrease of the effective trapping probabilities for electrons results in more electrons that get multiplied (see Fig. 6a).

- Measured amplification profiles and multiplication factors are moderate (few times) to high (10 to 15 times), depending on detector thickness and annealing times. The moderate increase of the multiplication factor with voltage points to a moderation of the field by trapping of the holes which reduces the negative space charge (see Fig. 6b). On the other hand, in thin sensors (75 and 150 μm) the field is very high due to large voltage applied over a small distance and charge multiplication is thus larger (see Fig. 6c).

- The increase of charge collection by multiplication is correlated with the increase of the dark current (see Fig. 6d) and the noise. However, their values are maintained or even improve during operation in the charge multiplication regime. At sufficiently high bias voltages it is observed that the signal-to-noise ratio remains much higher than at lower voltages, proving the beneficial effect.
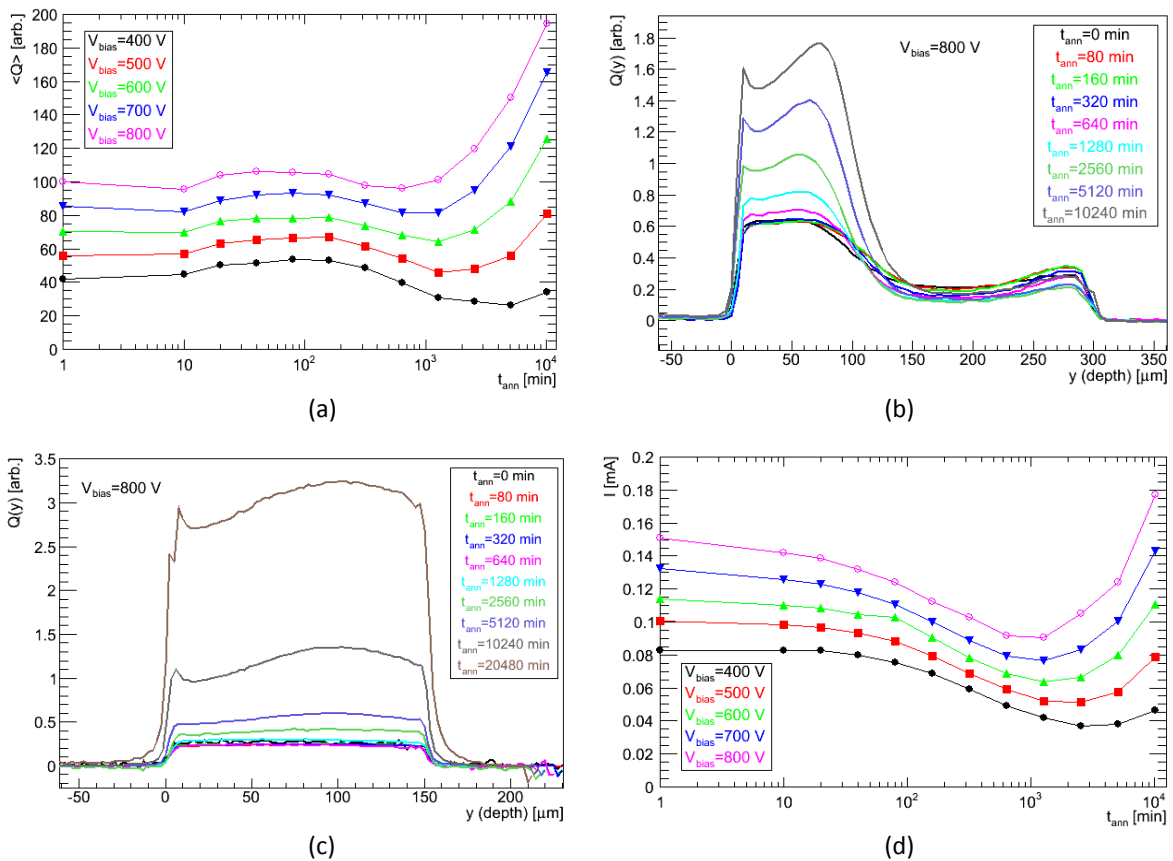

(a)

(b)

(c)

(d)

Figure 6: Influence of long term annealing at 60 ^{0}C; (a) Charge collected for a MIP-like e-h pair generation vs. annealing time at various bias voltages for a 300 μm thick n$^+$-p strip sensor produced on FZ silicon by HPK and irradiated to Φ_{eq} = 10^{16} cm^{-2}, (b) Charge collection profiles at V$_{bias}$ = 800 V for different annealing times for the same sensor, (c) Total charge collected vs. V$_{bias}$ for different annealing times for an MPP/HLL FZ n$^+$-p 150 μm thick strip sensor and irradiated to Φ_{eq} = 5·10^{15} cm^{-2}, (d) Dark current vs. annealing time at different bias voltages for the HPK sensor.
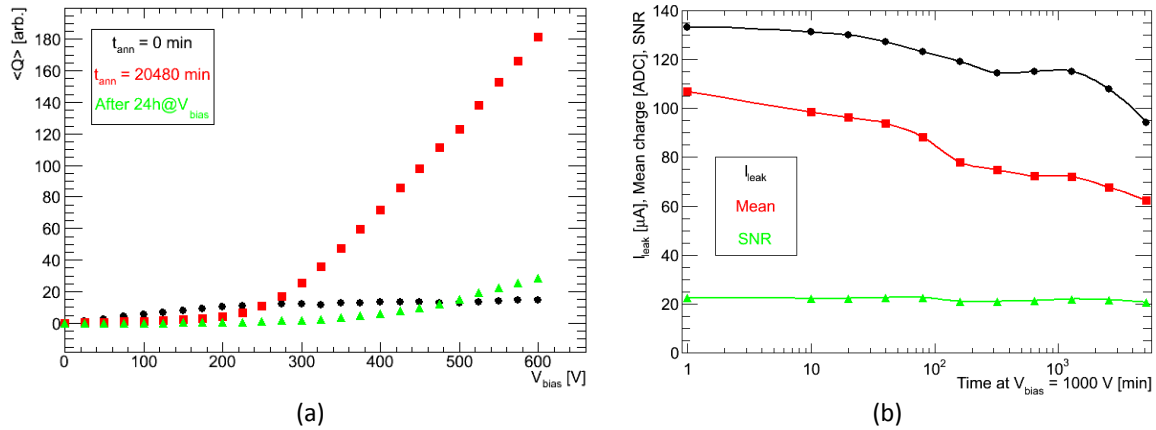
Figure 7: Influence of bias voltage (V$_{bias}$) after irradiation and long term annealing at 60˚C. (a) Total charge collected vs. bias at two different annealing times and after keeping the detector under bias for 24h, for an MPP/HLL FZ n$^+$-p 75 μm thick strip sensor, irradiated to Φ$_{eq}$ = 5·10^{15} cm^{-2} and annealed for 20480 min at 60˚C, (b) Charge collection, leakage current and SNR vs. time at V$_{bias}$ = 1000 V for an HPK FZ n$^+$-p 300 μm thick strip sensor irradiated to Φ$_{eq}$ = 5·10^{15} cm^{-2} and annealed for 10240 min at 60˚C.

- After long term annealing, if the sensor is kept under bias, charge multiplication quenches after a certain time, resulting in much smaller charge collection (see Fig 7a). This effect however can be overcome by operating the sensors at high bias voltages (V$_{bias}$ ≥ 1000 V). The signal-to-noise ratio (SNR) remains high as long as the multiplication signal increases faster with voltage then the noise (see Fig. 7b).

- In collaboration with the AIDA (EU FP7) project, Edge-TCT charge-collection measurements of a double-sided 3D silicon-strip sensor, produced by CNM Barcelona, were also conducted. After irradiation, the sensor showed an enhanced performance due to charge multiplication [11]. This is particularly pronounced in part of the sensor (along the line between the columns). An applied heat treatment (performed up to 600 minutes at 60°C) also proved to be beneficial.

We conclude: the Edge-TCT developed within P3 has proven to provide valuable information for the study of radiation-damaged silicon sensors. It has been used to measure the velocity profiles of the charge carriers and thus the electric field in highly irradiated sensors. In addition, thanks to the Edge-TCT a direct explanation of the charge multiplication process in irradiated sensors could be provided and the charge multiplication determined as function of applied voltage, dark current and annealing. Finally, using the Edge-TCT setup the charge multiplication could be demonstrated in double sided 3D silicon-strip sensors. The big impact of these measurements has led other research groups to set-up Edge-TCT setups in their labs.

SUMMARY P3

The aim of the P3 project has been to significantly contribute to the development of silicon sensors for charged particle tracking at the second operation phase of the Large Hadron Collider (now called HL-LHC) at CERN, where the sensors available at the start of P3 would fail because of radiation damage. One part of the proposal concentrated on understanding the relation between microscopic damage and sensor performance, and if an improved sensor performance can be achieved by doping the silicon crystal with impurities. The other part proposed to study 3D silicon sensors for their suitability for experiments at the HL-LHC.

In the first part the method of separating point from cluster defects by using irradiation by electrons with different energies could be established, and the relation between different defects and sensor-performance parameters like dark current and effective doping established. The study of the dependence on the impurities

on the introduction and kinetics of the different defects is still in progress. They are expected to be important for the decision on the optimal silicon crystals for the tracker for the HL-LHC experiments.

For the second part, the emphasis of the work has been changed with respect to the original proposal. 3D sensors were developed as it was expected that the signal from planar silicon sensors would degrade with irradiation to a level where the efficient tracking at the HL-LHC would become impossible. However, measurements done also at Hamburg and Ljubljana, on planar sensors with n$^+$ readout electrodes showed unexpectedly large signals, even at the highest HL-LHC fluences above 10^{16} hadrons/cm^2. As this is a promising alternative to 3D sensors, the study concentrated on this effect. With the help of the Edge-TCT set-up developed and constructed at Ljubljana, charge multiplication in high-field regions close to the n$^+$ electrodes could be identified as mechanism and studied in great detail for different sensor layouts. Based on these results, a number of groups have decided to embark on the design of silicon sensor with internal gain.

References

[1] I. Pintilie et al., Nucl. Instr. and Meth. **A** 611 (2009) 52.

[2] G.P. Summers et. al., IEEE Trans. Nucl. Sci., Vol.40, 6 (1993) 1372.

[3] I. Pintilie, et. al., Appl. Phys. Lett., 81, (2002) 165.

[4] M. Huhtinen, Nucl. Instr. and Meth. **A** 491 (2002) 194.

[5] R. Radu et al. **"**Radiation damage in n-type silicon pad diodes after electron irradiation with energies

between 1.5 MeV - 15 MeV", to be published in Nucl. Instr. and Meth. **A.**

[6] G. Lindström et al. (The RD48 Collaboration), Nucl. Instr. and Meth. **A.**466 (2001) 308.

[7] G. Kramberger et. al., IEEE Trans. Nucl. Sci. Vol. 57, 4 (2010) 2294.

[8] G. Kramberger, et al., Proceedings of Science , 021, Vertex 2010.

[9] R. Marco-Hernández et al., IEEE Trans. Nucl. Sci. Vol. 56, 3, (2009).

[10] M. Milovanović et al., 2012 JINST 7, P06007. (doi:10.1088/1748-0221/7/06/P06007).

[11] G. Stewart et. al., "Analysis of Edge and Surface TCTs for Irradiated 3D Silicon Strip Detectors", 20th RD50 Workshop (Bari), May 2012, accepted for publication in JINST.

PROJECT 4: MICRO PATTERN GAS DETECTORS

Project Coordinator: Leszek Ropelewski, CERN

Marco Villa, ESR, CERN. Supervisor: Leszek Ropelewski

Jing Dong, ER, INFN LNF. Supervisor: Giovanni Bencivenni

INTRODUCTION

Micro Pattern Gas Detectors (MPGD) are the subject of active R&D. The application of these precise and potentially cost effective gas detectors range from particle physics to applied areas related to X-ray or optical light detection. The GEM and MicroMegas detectors are well established and proven techniques. Their optimization and adaptation to larger sizes, special geometries and industrial production methods, which are required for future large scale applications, poses a number of challenging problems. Five MC-PAD Researchers worked on these topics. Two developments were grouped in project 4, the other two in project 5.

1 – LARGE AREA GEMS

Gas electron multipliers (GEMs) [1] are traditionally manufactured by laminating the base material between two negative tone photoresist dry films on which the hole pattern is subsequently transferred from photolithographic masks by exposure to UV light. The alignment of the masks with an accuracy of 10 µm or better is a prerequisite for good pattern matching and therefore good detector quality. Given the flexibility of both the base material and the two masks, and since the alignment is performed manually with the sole help of an optical microscope, the process becomes more and more involved and time consuming with the increase of the active area and it is not any more feasible when the linear dimensions of the sheet exceed about 30 cm.

In recent years, a growing demand for large area GEMs has arisen, frequently in combination with a need for large volume production capabilities. Instead of trying to improve the mask alignment over large areas, the chosen approach aims at simplifying the production process by using only one photolithographic mask [2], thus removing any needs for alignment. The idea at the base of single masking is to pierce the GEM from top to bottom, layer after layer, using the pattern produced in a stratum as a mask to etch the one right below it, until conical through holes are formed in the base material.

In this framework, I studied the effects of the hole geometry on the GEM behaviour using software simulations and I performed extensive tests on several GEM specimens to help enhancing their performance.

1.1 – Hole geometry study

The single-mask technology offers freedom of choice for almost all of the GEM geometrical specifications. However, it is not clear a priori what the optimal shape of the hole would be or what is the best orientation. Also, what is regarded as optimal depends on the properties that one wants to enhance.

In this context, numerical simulations can help to gain some knowledge on the influence that the hole geometry has on the GEM figures. The simulations proceed through three consecutive steps. ANSYS version

13.0 is used to define the geometry of the GEM elementary cell, fix the material properties and the applied voltages, set the symmetry and boundary conditions and solve the electrostatic problem by means of finite element analysis. Then Magboltz version 7.07 is exploited to model the properties of the selected gas mixture. Finally, Garfield version 7.43 is utilized to simulate the motion and the interaction of charges in the gas.

Figure 1 displays the simulated field lines (in yellow) and equipotential lines (in green) in a cross-sectional plane passing through the axis of a hole in a single-mask GEM. The 50 μm thick Kapton substrate is clad with 5 μm of copper on each side and pierced with conical holes, arranged in hexagonally packed configuration with a pitch of 140 μm. The diameter of the apertures on the two opposite faces is 85 and 55 μm, respectively. The foil is immersed in Ar:CO_2 70:30 at standard ambient temperature and pressure, biased with 400 V and surrounded by an external field of 3 kV/cm. The left frame shows that a GEM with wider holes facing the cathode has very good electron focusing properties, but a poor extraction efficiency. Conversely, the right frame indicates that wider apertures towards the anode result in a better extraction efficiency, at the cost of increased charge losses on the top electrode.
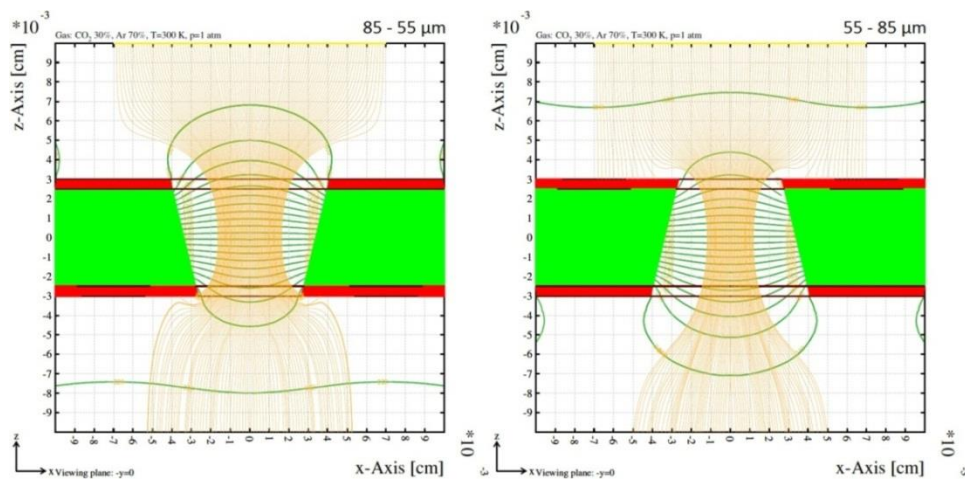

Fig. 1: Simulated field lines and equipotential lines in a hole of a single-mask GEM.

Figure 2 expands on these observations in a more systematic way. Different hole geometries are considered, reported in abscissa as top and bottom diameters, in microns. For every configuration, 1000 electrons are created, 70 μm above the GEM and with uniformly distributed x and y random position. Each electron is drifted with a microscopic tracking procedure that simulates every collision along the path, taking into account the cross sections of all possible interactions in the selected gas mixture. The ending point of the charges are then recorded and displayed in ordinate as per cent probability. Although the overall electron transparency is almost constant, the input and output charge transfer factors strongly depend on the geometry. Their concurrent optimization requires the combination of opposite geometrical properties, which can be achieved only by abandoning the conical shape in favour of a double-conical layout.
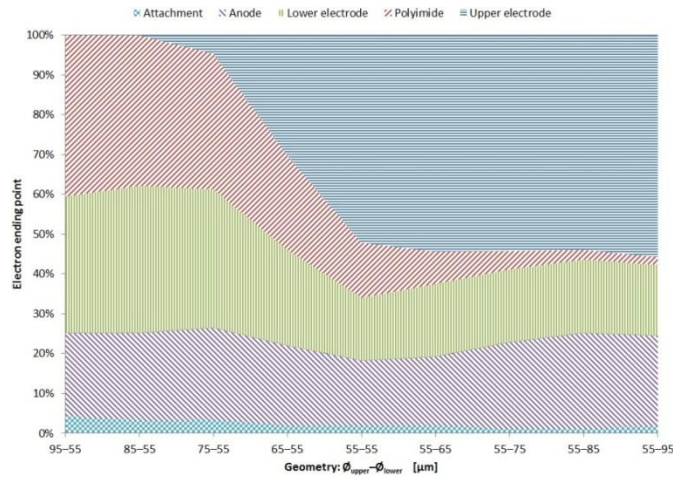
Fig. 2: Electron ending point for different hole geometries.

1.2 – Single-mask GEM technology optimization

Early single-mask GEMs had a rim around the edge of the Kapton holes, which degrades the time stability of the gain due to charging up of the exposed insulator. Several solutions have been tried; the most successful is the electrochemical active corrosion protection. One of the first samples realized with this technique can be seen in figure 3 (left), which shows the top and bottom faces of the foil, together with a hole cross section. The holes are neat and precise, with no over etching or spikes, and the electrodes are clean and polished.
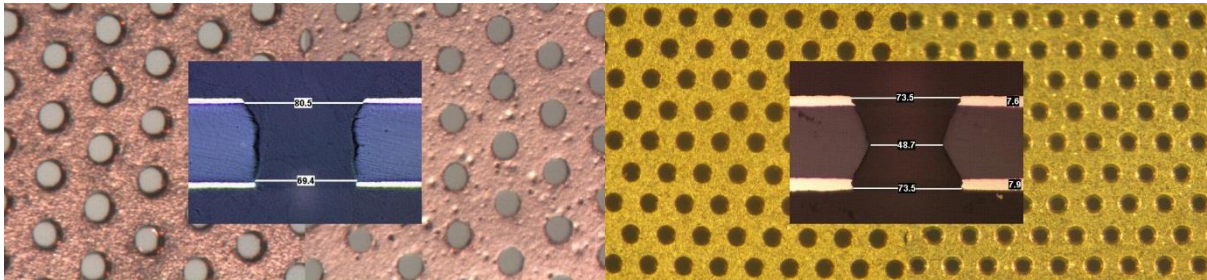

Fig. 3: Single-mask GEMs with electrochemical active corrosion protection.

However, experimental tests highlight low gas gains, as well as a not satisfactory gain stability over time. Additionally, the new foils appear to be easily damaged by discharges, unless small rims are reintroduced. All this is attributable to the conical shape of the holes and can be fixed by remoulding the apertures into a double-conical shape that resembles the one seen in double-mask GEMs, as displayed in figure 3 (right).

The additional dielectric in the openings drastically reduces the discharge probability and makes the foil more robust against the effects of sparks, enabling the use of zero-rim holes. High voltage tests performed on four specimens of 10×10 cm^2 active area in air at standard ambient temperature and pressure with 30 % relative humidity show no signs of discharges up to bias voltages of 510 V, with leakage currents not exceeding 0.3 nA. The new profile of the insulator also has better electric field lensing properties that greatly enhance the charge multiplication capabilities. At the same time, the *z* symmetry of the cavities leads to equal behaviour in the two possible GEM orientations, thus simplifying the detector assembly, while the rim-free apertures improve the time stability of the effective gas gain. A single-stage detector can be safely operated up to a voltage of 530 V, when flushed with Ar:CO$_2$ 70:30 at standard ambient temperature and pressure and illuminated with a collimated beam of monochromatic 8 keV copper photons at a rate of 20 kHz/mm^2. The corresponding

effective gas gain is about 1500, only slightly lower than for a double-mask GEM. The observed energy resolution, measured under the same conditions, is 18.6 % FWHM.

In conclusion, the novel single-mask GEMs perform similarly to the traditional foils, and the manufacturing method is scalable up to square metre size. The dimensions are in principle limited only by the size of the base material, which is delivered in rolls 24 inches (61 cm) wide and about a hundred metres long. Since the base material is the same as the one employed for traditional GEMs, one can expect outgassing, aging and radiation hardness to be as good. Moreover, the new process is reproducible, it has a high production yield and it is compatible with roll to roll equipment, thus enabling the production of large detector volumes in industry. In this scenario, a price drop of almost two orders of magnitude is expected.

2 – DISCHARGE TOLERANT MICROMEGAS

During the second long LHC shutdown, the ATLAS experiment plans the installation of a new pair of small muon wheels, replacing the current ones. The intervention is meant to significantly improve the performance of the muon system in the forward region, enhancing the level-1 trigger and the tracking precision. Requirements for the new chambers include a MIP detection efficiency of more than 98 % per plane, trigger capability, a rate capability of 16 kHz/cm^2, good resistance to radiation and good aging properties.

All these requirements can be met with micro mesh gaseous structures (Micromegas)[3]. The bulk technique[4] is scalable up to square metre size and, relying on standard photolithographic methods, it enables large volumes production in a commercial company. However, the considerable discharge probability due to the highly ionizing particles created in the ATLAS environment may limit the use of Micromegas-based detectors. For this reason, in 2007 the muon ATLAS Micromegas activity (MAMMA) collaboration has started an R&D effort, aimed at enhancing the Micromegas technology to make it spark tolerant, while maintaining the performance and the compatibility with industrial processing.

Within the MAMMA collaboration, I explored the idea of a preamplified Micromegas and I performed in-depth analysis of beam-test data from resistive chambers.

2.1 – Preamplified Micromegas

A possible solution is the introduction of a charge preamplification structure above the Micromegas mesh, with the purpose of distributing the required gas gain over two stages. The effect is that of reducing the number of sparks for a fixed effective gain, by extending the dynamic range of ionization charge in which the detector can be safely operated, to include the high charge deposition events.

The idea is explored with a 10 × 10 cm^2 test chamber equipped with a standard bulk Micromegas, on top of whose mesh a stretched GEM foil can optionally be fitted. The Micromegas is at first characterized in standalone configuration in Ar:CF$_4$ 90:10 at standard ambient temperature and pressure and the tests are then repeated in combination with the preamplification GEM under the same experimental conditions. The gas gain is gauged by measuring the counting rate and the anodic current while illuminating the detector with a collimated beam of 8 keV copper photons from an X-ray tube. The discharge properties, on the other hand, are probed with 6.5 MeV alpha particles emitted by ^{220}Rn unstable gas nuclides, that are produced by a ^{228}Th radioactive source sitting outside the chamber, coalesced with the employed mixture and transported into the active volume by the gas flow. For operative purposes, a spark is defined as a high charge depositing event that initiates a streamer in the gas volume and creates an electrical short between two or more electrodes, triggering a voltage trip of the power supply. The time between consecutive discharges is recorded and averaged over about 10 times. The reciprocal of the mean value, normalized with the alpha rate, gives the searched spark probability.

The results, expressed in terms of discharge probability vs. total effective gas gain for the two detector configurations, are summarized in figure 4. The red triangles trace the behaviour of the standalone Micromegas, taken as benchmark chamber. The green circles refer instead to the combined detector, where the transfer field is tuned for maximum signal amplitude and the gain of each amplifying structure is varied by the same relative amount throughout the voltage scan, to avoid overloading one specific station. Sparks are reduced by more than one order of magnitude already at a gain of 10^3, and the suppression factor increases even more at higher gains.
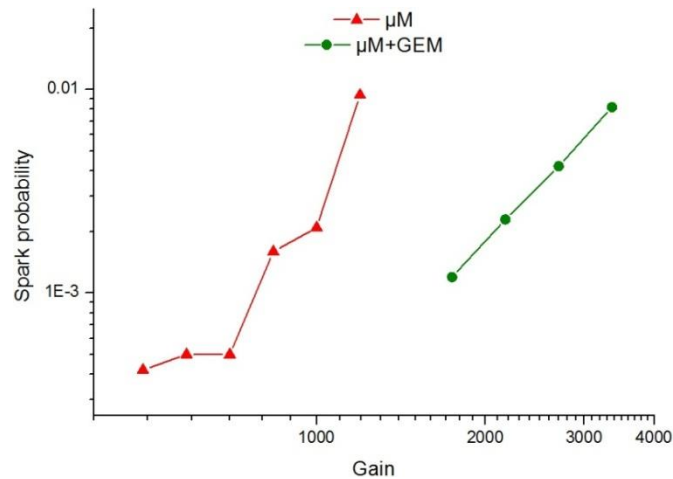

Fig. 4: Spark probability vs. total effective gas gain for a standalone and a preamplified Micromegas.

2.2 – Resistive Micromegas

The exploitation of a charge preamplification structure above the Micromegas mesh, although effective in decreasing the absolute number of sparks, requires additional power lines and internal support structures in case of extended active area, thus complicating the chamber services and mechanics. Moreover, the GEM stretching and gluing heavily rest on the manpower cost in the assembly phase, which is otherwise very low for single amplification stage Micromegas. For all these reasons, research has focused on developing the original Micromegas technology to make it immune to the undesired effects of sparks.

Many different approaches have been tried, and the most successful one is that of grounded resistive strips Micromegas [5], which is schematically presented in figure 5. The 10×9 cm^2 anode active area, patterned with one dimensional copper trails of 250 μm pitch, is coated with an insulating layer consisting of a sheet of DuPont Pyralux PC 1025 photo-imageable coverlay. This stratum is then topped with resistive traces matching the geometry of the readout pattern and having a resistance per unit length that ranges from 0.5 to 5 MΩ/cm in the different test chambers. The resistive structures have no ohmic contact to the anode elements, to which they are only capacitively coupled, but are connected to the detector ground through high value resistors which range from 15 to 45 MΩ in the various chambers. The Micromegas is completed by the amplification mesh, laminated in bulk technique at a distance of 128 μm from the resistive readout.
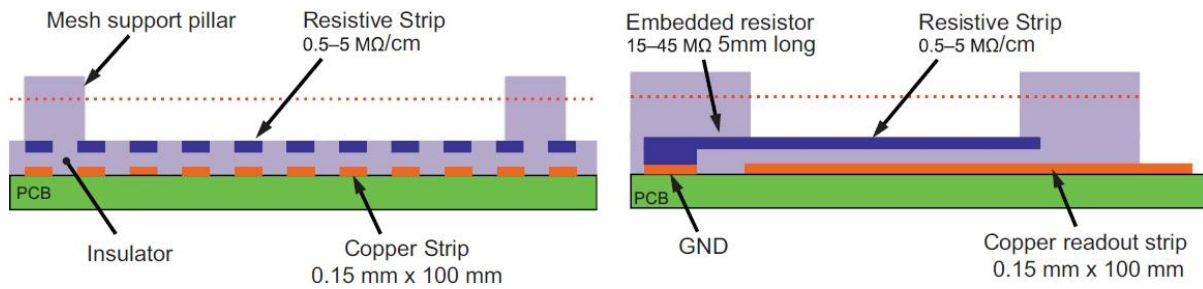
In a grounded resistive strips Micromegas there is no attempt to reduce the discharge probability, which is the same as in a non-resistive chamber. In case of sparks, the resistive structures limit the current flowing to ground, thus quickly and effectively quenching the streamers before they can cause any significant drop of the mesh voltage. Moreover, the segmentation of the resistive layer allows containing the area affected by the discharge. The overall effect is that of drastically reducing the dead time and boosting the detection efficiency.

The signals generated in two different gas mixtures by the conversion of 5.9 keV photons from a ^{55}Fe source have been measured for three resistive chambers and compared to the response of a standard Micromegas with the same geometrical parameters, which is taken as benchmark detector. For a given bias voltage, the effective gain of the resistive chambers is lower than for the non-resistive detector. This is not due to a poor charge multiplication, but rather to the different AC and DC couplings of the resistive structures to ground and to the anodic elements. Larger values of the grounding resistors result in smaller relative impedance to the readout, and thus give rise to stronger signals. The strip resistivity, on the other hand, doesn't seem to play a significant role and is chosen as to minimize the surface resistivity for high rate capability.

Figure 6 shows the MIP detection efficiency for a resistive chamber and for the benchmark non-resistive detector, as measured in a beam test with 120 GeV muons and pions. The standard bulk Micromegas performs well in muon beams, showing efficiencies close to 100 % even at gas gains exceeding $2 \cdot 10^4$. When operated in a pion beam, however, the efficiency drops considerably, with greater degradation at higher gains and particle rates. A hit position analysis reveals that the inefficient events are uniformly distributed over the trigger area, while a mesh power monitoring highlights tall current spikes and significant voltage drops in correspondence to the beam spills. All this finds explanation with the production of highly ionizing particles in the hadronic interaction of the pions with the chamber. The streamer following a high charge density deposition creates a short between the mesh and the readout, causing a drop of the amplification field over the entire active area and making the whole detector blind for some time. In the grounded resistive strips Micromegas, the resistive structures limit the current flowing to ground and thus quench the spark, allowing for pion detection efficiencies above 98 % over a wide gain window. No mesh voltage drop is observed, and a hit position plot shows that the remaining inefficiencies are due to the small dead area introduced by the mesh support pillars.
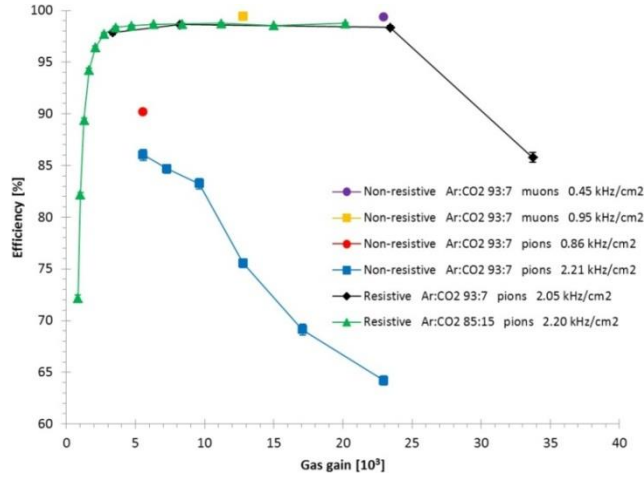
Fig. 6: MIP detection efficiency for standard bulk and grounded resistive strips Micromegas.

For space resolution, accurate studies reveal that the non-resistive chamber achieves 60 μm in Ar:CO$_2$ 93:7, while the resistive Micromegas reaches 35 μm in the same gas mixture, and goes down to 27 μm in Ar:CO$_2$ 85:15. Such a significant improvement is attributable to the larger cluster size that is in turn a consequence of the different detection efficiencies and of the capacitive couplings between resistive trails and neighbouring anodic traces, which contribute to spreading the signal in the direction perpendicular to the strips.

In conclusion, grounded resistive strips Micromegas are a promising technology for the new ATLAS small wheels. They solve the efficiency problems of standard Micromegas in hadron environments and offer a better space resolution. Moreover, the technology is scalable up to square metre size and is fully compatible with bulk processing, thus enabling large volume production in a commercial company.

4 R&D ON A CYLINDRICAL GEM AS THE INNER TRACKER OF THE KLOE-2 EXPERIMENT

The proposal of a new data taking campaign with KLOE-2 [6], at an upgraded DAφNE machine, has been accepted. The physics program [7] will focus on neutral kaon interferometry, study of the decays of K_S, η and $\eta^{□□}$ and searches for exotics. In the present KLOE apparatus, the tracking is provided by a huge and transparent Drift Chamber [8], filled with He:iC$_4$H$_{10}$ 90:10. The chamber has a vertex resolution of ∼ 6 mm and a resolution on transverse moment of $\sigma_{p\perp}$ / $p_\perp$ ∼ 0.4%. In order to improve the resolution on the vertices close to the interaction point, a new tracking sub-detector, the Inner Tracker (IT) [9], will be installed in between the Drift Chamber inner wall and the beam pipe. The requirements for the Inner Tracker can be summarized as: (1) $\sigma_{r□}$ ∼ 200 μm and σ_z ∼ 500 μm spatial resolution, (2) 5 kHz/cm^2 rate capability, (3) < 2% X_0 material budget. The adopted solution is the Cylindrical-GEM (CGEM), a triple-GEM detector composed by concentric cylindrical electrodes : 1 cathode, 3 GEM foils and 1 anode, acting also as the readout circuit. The IT will be composed by four layers of cylindrical triple-GEM 700 mm long, each of them equipped with a two-dimensional readout, with radius of the layers ranging between 13 cm and 23 cm. Including the carbon fibres support, the detector has a material budget of ∼ 1.5% X_0. According to simulations, the IT will improve by a factor of 3 the spatial resolution on the K_s → $\pi\pi$ (presently ∼ 6 mm). The Inner Tracker is under construction and is planned to be accomplished and ready for the installation by the end of 2012. In the training period we concentrated our activity on the following items:

1. The study of the final XV strip readout configuration. This was performed at the H4-SPS beam CERN facility with a telescope composed by small, 100×100mm^2, planar GEMs in magnetic field with the first version of the GASTONE chips.

2. Construction and test of the large area planar GEM with single-mask GEM foils and with an active area of 480×700mm^2.

3. Construction of the first two layers of the Inner Tracker.

5 SMALL PLANAR GEMS FOR READOUT STUDIES AT THE H4-SPS BEAM CERN FACILITY

A typical orthogonal X-Y readout cannot be used for the Inner Tracker due to its cylindrical geometry, therefore a more suitable solution for the final design of the detector is a 2-D readout segmented with 650 μm pitch XV patterned strips (see Fig. 7). A dedicated test [10] of the functionality of this readout was done at SPS-H4 North Area beam line at CERN. Since the IT needs to operate inside KLOE magnetic field of 0.52 T, the effects on the readout and on the formation of cluster of fired strips have also been studied. The H4 area is equipped with the GOLIATH magnet which provides a B field adjustable from 0 to 1.5 T, perpendicular to the horizontal beam-plane (X- Z). For the test we used a 150 GeV/c π^+ beam. The X-V readout was tested with a tracking telescope constituted by 5 100×100 mm^2 planar triple-GEMs detectors with 650 μm pitch readout strip plane: four chambers were equipped with standard X-Y readout while the fifth one with the X-V readout under investigation. The setup was 1 meter long with detectors placed equidistantly and the XV chamber placed in the centre. The GEMs were partially equipped with 22 digital readout GASTONE boards with 32 channels each, four on each XY chamber and six on the XV chamber. This was enough to fully cover the area illuminated by the SPS beam. We have used the same working point as for the CGEM prototype: Ar/CO$_2$ (70/30) gas mixture and operating voltages V$_{fields}$ = 1.5/2.5/2.5/4 kV/cm and V$_{GEM}$ = 390/380/370 V (ΣV$_G$ = 1140V). The spatial resolution obtained as a function of the magnetic field is shown in Fig. 8, while in Fig. 9 the plot of the residuals at B = 0 T is reported. A clear effect on the resolution is observed as a function of increased magnetic field, due to the Lorentz force. In our test-beam setup, this affects only the X coordinate (that corresponds to the bending plane). The resolution on the X coordinate ranges from 200 μm at B=0 T up to 380 μm at B=1.35 T. The resolution on the V coordinate is ∼ 280 μm corresponding to ∼ 370 μm on the Y coordinate, Fig. 10.
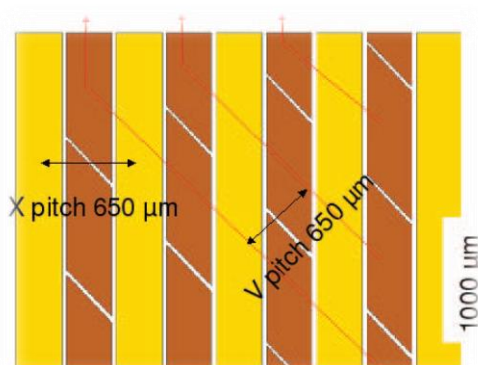

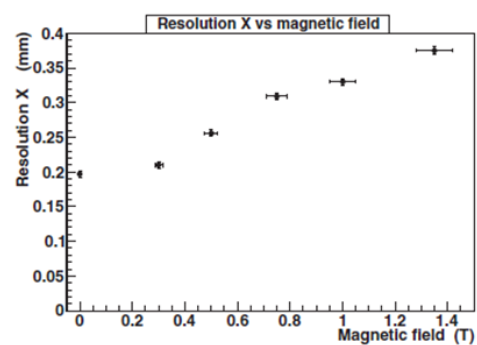Figure 7: Scheme of the X-V readout configuration.

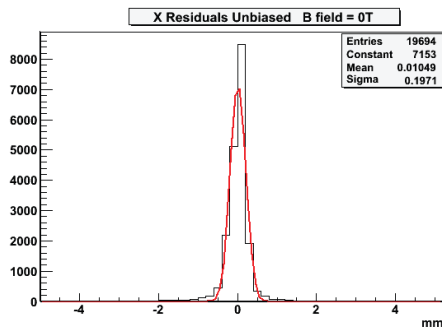Figure 8: X coordinate resolution as a function of B field.
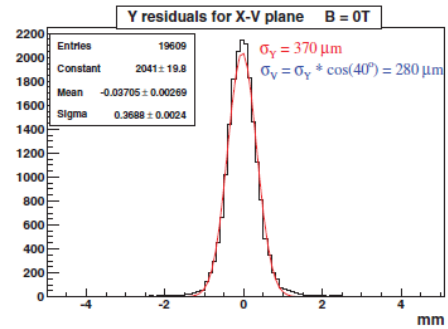
Figure 9: Residuals in the X view for B=0.

Figure 10: Resolution of the V coordinate X-V readout GEM without B

In the same test, we have also found that the increase of the magnetic field, leading to a larger spread of the charge over the readout strips, causes a reduction of the charge seen by each single pre-amplifier channel, with a consequent efficiency drop. So that the increase of the magnetic field requires for higher gains in order to efficiently operate the chamber.

6 LARGE AREA GEM

The outermost layer of the IT requires a 1440 × 700 mm2 GEM foil which is obtained splicing three 480 × 700 mm2 foils. The request for large GEM foils led to a change of the manufacturing procedure by CERN TS-DEM-PMT laboratory, switching from the double-mask (requiring a very fine alignment of the two masks) to single-mask etching [11]. The holes of the new GEMs have quasi-cylindrical shape and for this reason a new characterization was necessary. A triple-GEM was realized with the new large foils and tested with a 137Cs source (660 keV photons). The measured current was normalized to the one obtained by a 100×100 mm2 double-mask manufactured triple-GEM. The measurement (Fig. 11) shows that the gain for the new hole shape is ∼20% lower than in the double-mask case at a fixed HV. The large area triple-GEM has then been tested at the T9 area, using the same external tracking used in the previous test beam. The chamber was equipped with the final X-V readout. The test beam allowed validating the final DAQ and FEE chain, composed by the GASTONE64 chip, interface boards, General Intermediate Boards and the Software Interface. The detection efficiency as a function of the voltage applied to the GEM foils is shown in Fig. 12 (right).
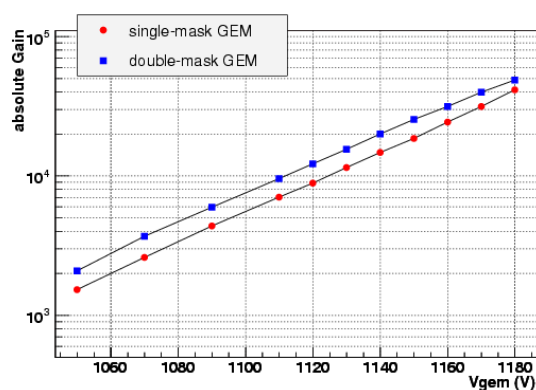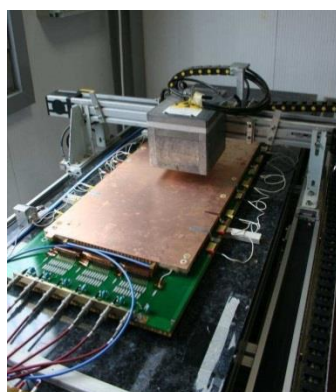

Figure 11: Setup for the measurement with the 137Cs on the large planar triple-GEM and comparison of the gain measured with a double-mask and a single-mask manufactured GEM as a function of the applied voltage.
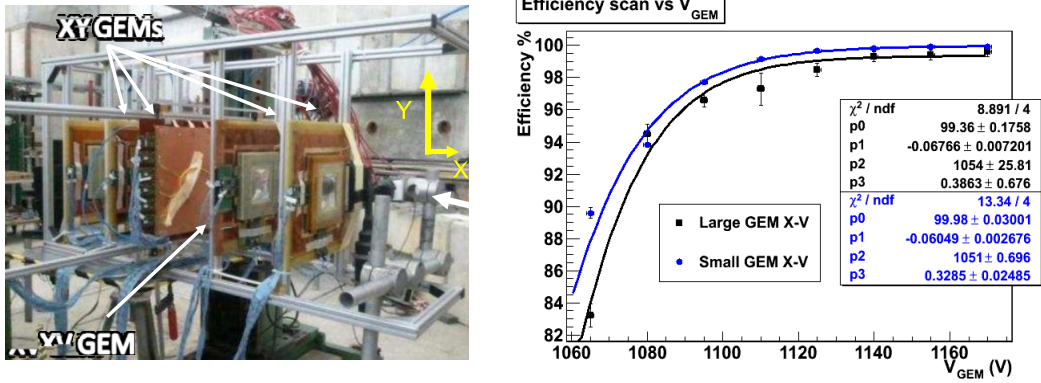
Figure 12: Setup of the Large Area GEM test beam (left) and detection efficiency as a function of the sum of the voltage applied to the GEM foils of a triple-GEM (right). Blue points are obtained by the double-mask manufactured GEMs while the black ones refer to the GEM realized with the new single-mask technique. The fit is obtained by Fermi-Dirac functions.

7 CONSTRUCTION OF THE INNER TRACKER SYSTEM

The Inner Tracker system will be composed by four concentric layers of CGEM detectors (Fig. 13). The technology used to build the cylindrical electrodes does not require the presence of internal frames as a support and therefore allows us to realize an intrinsically dead- zone-free detector. Indeed, thanks to the cylindrical shape itself, the typical sag of the electrodes it is found to be negligible: < 5 μm for an overall stretching mechanical tension of ∼ 50 kg applied at the detector ends. The detector construction has been entirely carried out in a class 1000 clean room: it is a clean procedure and protective clothing are always worn. The clean room includes: (1) the storage areas for GEM and readout circuit foils apart those dedicated to the storage of the fiber-glass components, (2) the GEM testing areas, for optical inspection and HV test, (3) the cleaning area for fiber-glass components, (4) the planar and cylindrical gluing stations, (5) the detector assembly area and the area for the final detector test: gas leak and HV test.
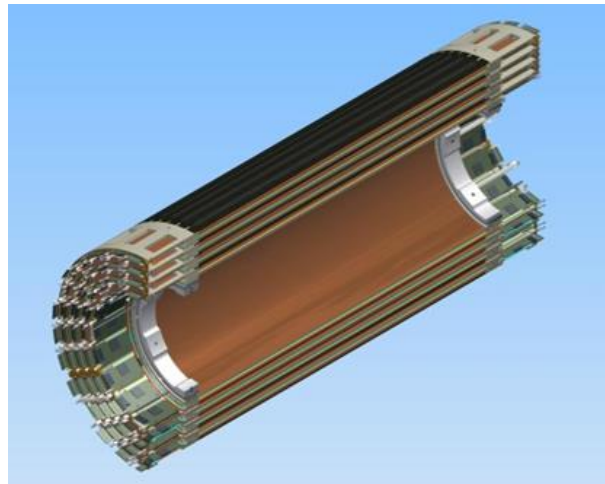
Figure 13: Inner Tracker global view

Each of the 4 layers of the IT will be a Triple-GEM independent detector composed by: the cathode, the 3 GEM foils for the multiplication stage (gain ∼ 10^4) and the anode read-out circuit. These electrodes are obtained from very light polyimide foils (100 μm thick for cathode, 50 μm for GEMs, 150 μm for Anode) rolled up to a cylindrical shape. The cylinders are then inserted one into the other and fiberglass annular flanges are

glued at the ends, acting as spacers for the gaps and as supporting mechanics. The Front-End Electronics for the IT is based on the new dedicated GASTONE ASIC, a 64 channels chip specifically developed for the GEM detector. The closed detector will be then moved to the laboratory where it will be tested first with X-rays, in current mode, and then with cosmics, after the installation of the front-end electronics.

7.1 Material preparation & Quality controls

Before the final assembly of the different parts of the detector, each component follows a well defined preparation procedure that includes a global optical inspection, a cleaning and an HV test.

GEMs are produced by the EST-DEM Workshop at CERN. A GEM foil realized for the construction of the full scale detector and the detail of a sector are shown in Fig. 14: clearly visible is the sector's structure realized on one side of the foil with the aim of reducing the energy stored and then released in case of discharge through the GEM hole. A first quality check is done at CERN by the producer: besides a global optical survey each sector is supplied with a voltage up to 500 V and checked for leak current that should be smaller than 5 nA. This test is performed in clean room at ambient temperature and relative humidity, which is without putting the GEM foil into a nitrogen flushed gas box. GEMs are delivered to LNF inside a rigid clean plastic plates, each foil protected between clean soft papers. In our laboratory they are stored in a dedicated cabinet inside the clean room and always handled by operators suitable worn with clean clothing, facial mask, gloves and hat. GEMs do not require any special cleaning procedure, because in principle they are clean: the only allowed cleaning procedure is done with a light nitrogen flush that is used to gently remove possible dust. Any other procedure can instead damage the GEM and is strongly forbidden. A first optical inspection is done by eye to look for areas with possible defects. A more careful inspection of any evident spot is performed under microscope, equipped with digital camera to evaluate the dimension and type of defect .
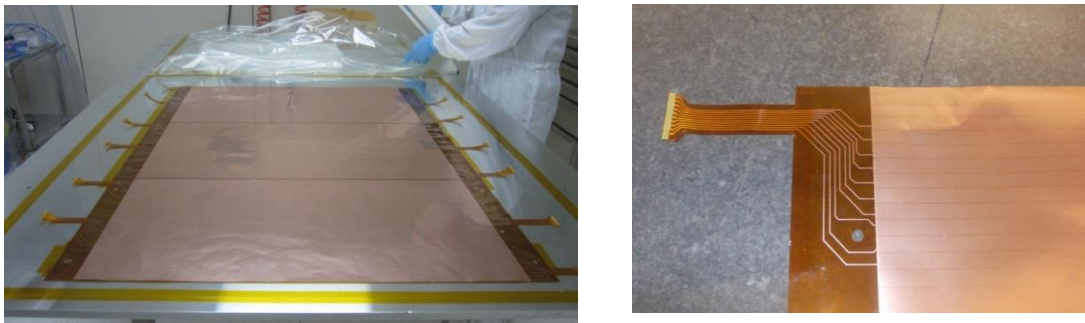

Figure 14: a large GEM foil (left), detail of the sector (right).

The G E M HV test is performed inside a gas tight box flushed with Nitrogen, in order to reduce the humidity down to 10% Residual Humidity (about 1 hour). The HV is applied individually to each sector through a 500 MΩ limiting resistor, to avoid GEM damages in case of discharges, while the non-sectored side is grounded. The HV is slowly increased with eighteen steps up to a maximum of 600 V. The GEM sectors pass the HV step if the current is less than 1 nA and no more than 3 discharges occurred during the test time. In case these acceptance requirements are not fulfilled the voltage ramp-up on the sector is suspended and the test is repeated later on.

The readout anode circuit is manufactured by EST-DEM CERN Workshop, on the basis of our design, starting from the 5μm copper clad, 50 μm thick polyimide substrate, the same used for GEM foils. The 650 μm pitch, 300 μm wide X strips are parallel to the CGEM axis, giving the rϕ coordinates;

while the V strips, realized connecting by vias a suitable pattern of parallelogram shaped pads, and forming an angle of about 40 degrees with respect the X- strips, gives the z coordinate.

A first check to look for shorts between both coordinates is performed by the producer. Connections test between pads and vias is also required. A useful validation consists of measuring the distance between first and last strip at different positions for both coordinates, requiring a maximum deviation from the nominal o n e not exceeding 100 μm. The cleaning procedure for the readout anode circuits is done with spraying alcohol and a nitrogen flush to remove possible dust. Any other procedure can instead damage the circuit and is forbidden. The anodes are stored in a dedicated cabinet in the clean room and handled by operators suitable worn with clean clothings, facial mask, gloves and hat.

The annular frames, defining the gaps between electrodes, are 3 or 2 mm (1 mm) thick and 35 mm wide. They are made of Perma-Glass and they are the only supports for the cylindrical electrodes. The cathode and anode frames contain the gas inlets and outlets respectively. The frames delivered by the machine workshop, before entering the clean room, are washed with isopropyl-alcohol and brush. Once a careful optical inspection is performed, to eliminate spikes and possible broken fibers, a two-cycles cleaning in a ultra-sonic bath with demineralized water for 30 minutes is done. After the cleaning, the Perma-glass components are dried in the air for 24 hours. The final cleaning is done with spraying alcohol and flushing Nitrogen.

7.2 Details of IT Construction

The main construction steps can be summarized as follows:

1. Three GEM, as well as the anode (Fig. 15, left) and cathode, foils are preliminary glued together to obtain a single large foil needed to realize a cylindrical electrode. For this operation we exploit a precise Alcoa plane and the vacuum bag technique.

2. The large foil is then rolled on a very precise aluminum cylindrical mould (Fig. 15, centre) covered with a 0.4 mm machined Teflon film for easy and safe extraction of the cylindrical electrode. The mould is then enveloped with the vacuum bag, and vacuum is applied for the glue curing time (about 12 hours).

3. The final assembling of a CGEM layer is performed by means of the Vertical Insertion System (VIS), a tool that allows a smooth and safe insertion of the cylindrical electrodes one after the others (Fig. 15, right). The system is designed to permit a very precise alignment (0.1 mm on 1 m global length) of the cylindrical electrodes along their vertical axis. The bottom electrode is fixed on its mould, while the top one is slowly moved downwards by a computer controlled step-motor, coupled with a reduction gear system. The operation is performed with the help of a web-camera, thus allowing the monitoring of the radial distance between the electrodes (2-3 mm typically). The up-down rotation of the assembly tool allows an easy sealing of the detector on both sides.
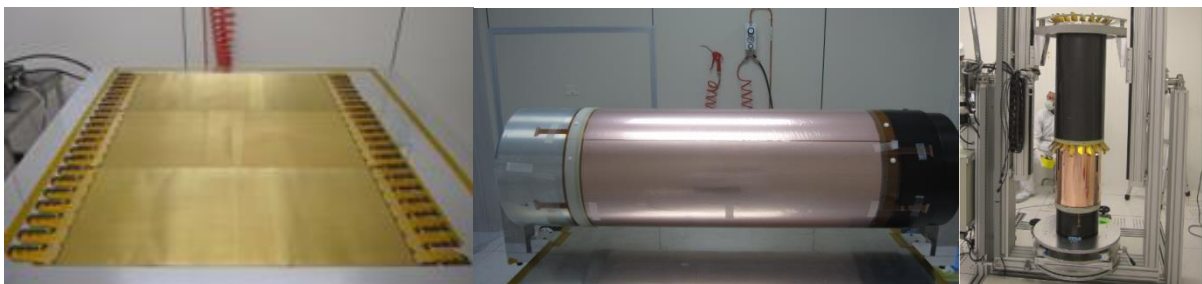

Figure 15: Planar gluing of the three anode foils (left), A C-GEM (centre), Insertion of a C-GEM into the anode (right). (right).

CONCLUSIONS

The final readout configuration was validated with the test of small planar prototypes operating in magnetic field. The results match the final IT requirements. A large planar GEM prototype was realized with the new single-mask technique: a characterization with X-rays revealed that the gain is ~20% lower than using the double-mask technique. The large GEM was then tested with the final DAQ and FEE chain. Construction has started and will be completed in spring 2013.

Rε

[1]   F. Sauli, *GEM: A new concept for electron amplification in gas detectors*, Nucl. Instr. and Meth. A 386 (1997) 531

[2]   M. Villa et al., *Progress on large area GEMs*, Nucl. Instr. and Meth. A 628 (2011) 182

[3]   Y. Giomataris et al., *MICROMEGAS: a high-granularity position-sensitive gaseous detector for high particle-flux environments*, Nucl. Instr. and Meth. A 376 (1996) 29

[4]   Y. Giomataris et al., *Micromegas in a bulk*, Nucl. Instr. and Meth. A 560 (2006) 405

[5]   T. Alexopoulos et al., *A spark-resistant bulk-micromegas chamber for high-rate applications*, Nucl. Instr. and Meth. A 640 (2011) 110

[6]   F.Bossi et al. , *Precision Kaon and Hadron Physics with KLOE*, Rivista del Nuovo Cimento, Vol. 31, N. 10 (2008)

[7]   G. Amelino Camelia et al., *Physics with the KLOE-2 experiment at the upgraded DAFNE*, Eur. Phys. J. C 68 619 (2010)

[8]   M. Adinolfi et al., *The tracking detector of the KLOE experiment*, NIMA 488 (2002) 51

[9]   KLOE-2 collaboration, *TDR of Inner Tracker for KLOE-2 experiment*, LNF-10/3(P) INFN-LNF, Frascati, 2010

[10] E. De Lucia at al., *Status of the cylindrical-GEM project for the KLOE-2 Inner Tracker*, NIMA 628 (2011) 194

[11] M. Alfonsi et al., *Activity of CERN and LNF groups on large area GEM detectors*, NIM A 617 (2010) 151

PROJECT 5: TPC WITH MPGD READOUT

Project Coordinator: Ties Behnke, DESY Hamburg.

Rahul Arora, ESR, GSI. Supervisor: Christian Schmidt.

Stefano Caiazza, ESR, DESY. Supervisor: Ties Behnke.

Rolf Schön, ESR, NIKHEF. Supervisor: Els Koffeman.

INTRODUCTION

Time projection chambers are used in many areas of physics. They are used as tracking detectors in high energy physics experiments, for example at the ALICE experiment at CERN or at the proposed ILD experiment at an linear collider. They also find applications in other areas of science where the tracking of charged particles over large volumes with excellent precision and efficiency is required.

In recent years the use of micro-pattern gas detectors (MPGD) in time projection chambers has received significant attention. A readout based on MPGD offers a number of advantages. Typical feature sizes of the MPGDs are of order of the spatial resolution of the TPC, around 100 µm, or about an order of magnitude smaller than in a conventional wire based readout. Thus potential systematic effects introduced by local field inhomogeneity are reduced. Electrons drifting towards the amplification structures need to move perpendicular to the electrical field only by a distance of order of the feature size.

Two approaches are followed: In the conventional approach the gas amplification system is mounted on a pad plane. The charge is collected by the pads, routed to a charge sensitive preamplifier, and digitised. Such systems are studied by two of the researchers in this project, for experiments at the GSI and for the ILD experiment. An alternative ansatz is followed by the third project. Here a micro pattern gas detector is produced on the surface of a pixelated chip through post processing techniques. The result is a compact and fully integrated gas detector with very fine pixel readout. The technology for this is still in its infancy, but first very promising results have been obtained and are shown here.

A GEM BASED TPC FOR FAIR AT GSI

The Project P5 at GSI is about the development of a prototype Time Projection Chamber (TPC) with GEM (Gas Electron Multiplier) [1] as amplification stage. The main objectives of this project are the central tracker upgrade of the FOPI experiment [2] at GSI, Crystal Barrel experiment at ELSA/Bonn and it was also the central tracker candidate for the PANDA experiment [3] at FAIR (Facility for Antiproton and Ion Research) at GSI. In order to evaluate the feasibility of such a detector system, a prototype detector was built and commissioned in the FOPI experiment and tested with cosmic and different beam conditions.
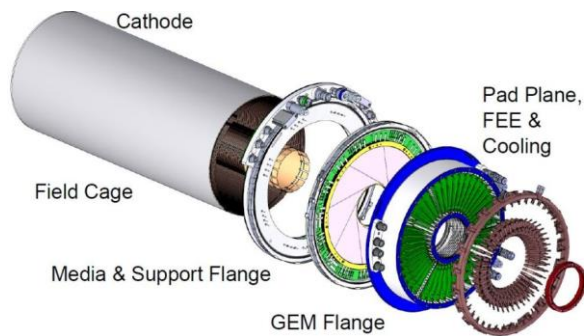
A Time projection chamber (TPC) is an ideal detector for tracking with its excellent charge particle tracking capabilities along with very low material budget for preserving the energy and mass resolutions. A truly three-dimensional reconstruction of an event can be made by recording both the radial (r) and azimuthal (θ) coordinates at which a charged particle enters and leaves a gas filled chamber. The arrival times of the electrons at the end-plates determine how far they have travelled and hence the axial (z) coordinate of the charged particle, thus allowing it to be tracked along its journey through the chamber. Owing to the modern beam requirements for experiments, the TPC has to operate at high particle rates and in a continuous mode, i.e. without gating. For a number of running and future particle-physics experiments, studies on the readout of Time Projection Chambers (TPCs) based on the Gas Electron Multiplier (GEM) foils are ongoing. This technology offers higher granularity and intrinsically suppressed ion feedback as the two major advantages compared to a conventional readout with Multi-Wire Proportional Chambers (MWPC).
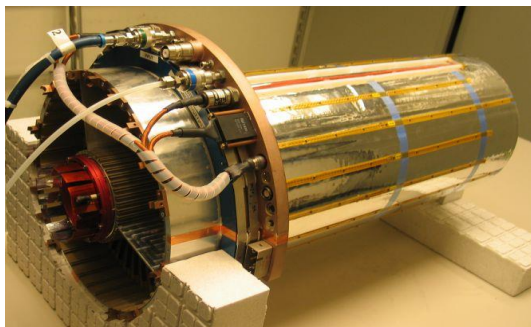
Prototype Detector System

The design and the actual detector prototype are shown above in Fig. 1. In order to evaluate the feasibility of such a detector system, a large prototype GEM-TPC [4] was built and commissioned inside the FOPI spectrometer. The detector system was tested with cosmic radiation and several ion beams. The large prototype GEM-TPC detector consists of several modular structures as shown in the design schematic in Fig. 1. Its overall size is $\varnothing$ 450 mm × 880 mm. It consists of two concentric cylinders forming the inner and outer field cage and a planar cathode of the drift volume, the media and support flange, the GEM flange, the pad plane, the front-end electronics and the cooling system. The active volume is contained between the inner diameter of 104 mm and the outer diameter of 308 mm, and has a drift length of 727.8 mm. The gas amplification stage of the prototype consists of a stack of three standard CERN GEM foils (Cu/Kapton® 5/50 µm of thickness with double-conical hole pattern 50/70/140 µm $\varnothing Cu/\varnothing K$/pitch). The gain recorded was of the order of several thousand with a gas mixture of Ar/CO_2 and Ne/CO_2 (90:10 mixtures). The GEM foils are segmented on one side

into eight iris-shaped sectors which limits the maximum charge and thus the damage done by an eventually occurring spark discharge.

Testing and Commissioning of the prototype in FOPI Spectrometer

Each GEM is first tested for the leakage current measurements at 600V in dry nitrogen with relative humidity below 1%. The currents were found to be in the ranges of few nA. After the satisfactory tests the GEMs are glued on frames and then assembled in the GEM Flange. After assembling the GEM Flange with Media Flange and a pad plane we get the GEM detector without the field cage. There were tests done on the detector for gas tightness, material stability in high voltage and out gassing. The results were promising and as expected. The detector was first tested without the field cage to check gain uniformity of the GEMs as well as the total gain of the detector. The first tests were promising with a gas mixture of Ar-CO2 (70:30) at a scaling factor of up to 1.07 of the nominal voltages. The source employed for the tests was Fe55 with 5.9 keV X-ray K-alpha line. The gain of the detector was about 5100 for scale factor of 1.02 and 10000 for 1.07. After the complete assembly of the detector with Field Cage, cooling for FE cards and other accessory sensors, the detector was commissioned in the FOPI experiment in the first week of Nov. 2010 and tested with heavy ion beams during several beams tests in last two years. At first, the data was taken with cosmic radiation and later with the ion beams. The picture above on the left shows the 2D noise distribution in the pad plane which was pretty uniform over the whole pad-plane.
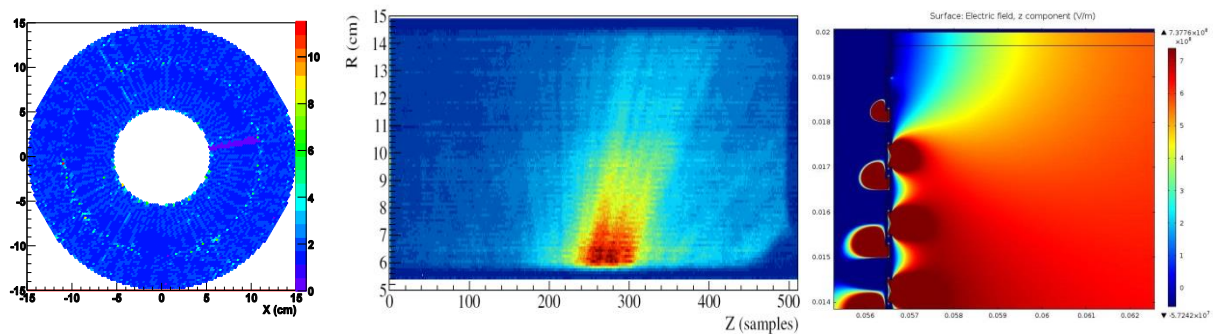

Figure 3:

Almost all of the ~10000 channels were readout. The picture in the middle is occupancy plot of the GEM-TPC detector taken with a pion beams and target placed in the middle of the chamber. The field inside the chamber is very uniform except the lower right corner as can be seen in the picture. The electric field simulations were done to determine the amount of distortion in the electric field due to the shortcuts in the initial 2-3 strips. The simulations agree with the experimental values for the amount of distortions in the radial direction. Picture on the right shows the surface plot of electric field distribution inside the field cage for a system with first three strips at the same potential as cathode. In summary, the prototype GEM-TPC detector system was built within the time frame of the project, tested and is still operational under the realistic environment at FOPI. The targets set in the start of the project were achieved. The application of the prototype in a running physics experiment has provided valuable data on the tracking performance of an un-gated GEM-TPC. Further design revisions are going on for the final version of the detector to be employed at the Crystal Barrel experiment at ELSA/Bonn. The work done has also generated valuable input for the ALICE TPC upgrade project. The analysis of the data taken during the physics runs is ongoing.

DEVELOPMENT OF A GEM BASED TPC READOUT MODULE

One of the two experiments proposed for the envisioned future Linear Collider (be it ILC or CLIC) will make use of a large TPC as the main tracking detector. This TPC will have a diameter of 3.6 m and aims to achieve a momentum resolution as good as $\frac{\Delta p_t}{p_t^2} \cong 9 \cdot 10^{-5} \frac{c}{GeV}$ [5]. To reach this goal the TPC must sample each of the tracks in more than 200 space point with a point resolution better than 100 μm over the complete drift distance.

To achieve this goal the usage of the most advanced MPGD technologies is envisioned. To test these technologies and develop them to be able to perform as required a Large Prototype TPC (LP) was completed and put in operation at DESY in 2008 [6].

The goal of this project was to develop a readout module with GEM based amplification and pad readout. A key point of the project was the development of a novel GEM support system based on thin ceramic frames. This module has been named the GridGEM module.
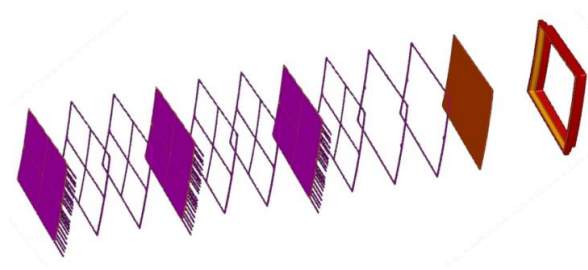

Figure 4: Sequential stack of the components constituting the GridGem readout module. From the right: back-frame, readout board, alternating groups of ceramic grids and GEMs

Module Design

The basic components of the GridGEM module (Fig. 4) are:

- An aluminium back-frame to ensure the mechanical stability and the gas tightness of the whole system, compatible with the LP module mounting system, providing the alignment of the sensitive area with the external references of the detector
- A pad based readout board. The board is designed to have 28 rows of equally sized pads $1.25 * 5.85 \ mm^2$. Each pad is independently routed to one of the connectors installed on the back side of the board. These connectors are compatible with the ALTRO based electronics [7] [8] [9] used to readout the system. This board also integrates the HV distribution system that provides power to the GEM foils
- A stack of up to 4 GEM installed in special ceramic structures that ensure the flatness of the foil. Each GEM foil is divided into 4 sections to reduce the energy available to a discharge event, to avoid that the discharges do destroy the foils. The ceramic grid is laser cut and provides a support lattice to which the GEMs are glued. The lattice cells are about 10 cm wide. The supports are only 1 mm wide thus limiting the dead area. Once glued together the stack of ceramic grid and GEM is a mechanically stable self-supporting system.

Module Construction

Before module assembly all components are individually tested. In particular the GEMs are installed in a test box and individually supplied with high voltage and tested for discharges. All components are measured for compliance with the specifications, and are visually inspected.

The ceramic frames are then glued to the GEM foils. With the exception of the top most GEM two frames are glued to one foil, on the top and on the bottom. The GEMs which have been custom produced at CERN have a gluing path on the surface which is 1.5 mm wide. Special care is taken to meter out a well-controlled amount of glue so that no glue spills onto the active area of the GEM. To this end a robotic glue dispensing system has been built which lays down a bead of glue on the ceramic frame. Using a precision jig the frames are then positioned on the GEM and glued. The glue is cured in an oven for a few hours.

After framing the GEMs are stacked up on top of the readout board. They are aligned with pins in the corners relative to the pad plane. At the moment and for the prototype module the stack is held together with simple non-conductive screws. This is fast and easy and makes the replacement of individual GEM foils possible. For the final version the GEMs will be glued on the pad frame to each other. The final step in the module assembly is the connection of the high voltage lines. They are all concentrated on one side of the module. Each GEM foil is individually powered on both surfaces. The design of the high voltage distribution system was particularly challenging as in total

Test of the readout module

To check the performances of the module after its final assembly and before any test beam campaign, I also developed and built a small TPC, called TestBox, that can accomodate a single readout module and allows to test its high voltage stability and, with an additional DAQ system not yet available, to measure the detector response using radioactive sources. This device is shown in Figure 2 with the first prototype module installed.

After the quality checking of the module inside the TestBox we organized and run a 2 week long test beam campaign at the DESY II electron beam station T24, installing the GridGEM module in the LP. During this campaign we collected about 2 million events with and without magnetic in different module and TPC configurations. This test-beam campaign and the following analysis of the acquired data helped us to identify the major points on which to intervene to improve the system

Data Analysis

The analysis of the data acquired during the test beam campaign was performed at DESY using the tools provided by the ILCSoft software framework. The raw data acquired were first converted to the LCIO format with an ad-hoc C++ program. The information contained in these data were reconstructed using the Marlin system and, in particular, the tools provided by the MarlinTPC system. The reconstructed data thus obtained were analyzed using an object oriented C++ framework specifically developed during the last year for the analysis of TPC test-beam data. This set of programs provides an extensible set of tools to perform the offline data quality monitoring and the analysis of the obtained data.

The charge collection efficiency measured across the module is shown in **Error! Reference source not found.**. steep drop in efficiency at the edges of the module is visible.

Based on a detailed electrostatic simulation of the fields the cause of the distortion was identified. The gap between modules exposes an electrically grounded surface to the field, which created significant distortions. For a future module the introduction of the guard ring next to this gap will reduce this problem significantly.

A second generation module has been constructed and tested in the meantime and addressed many of the problems found.
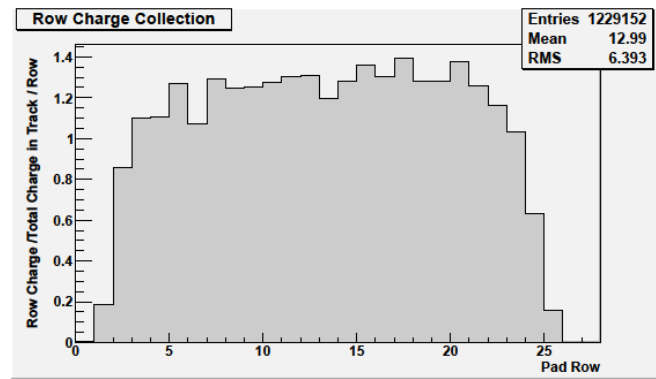
Figure 5: Charge collection efficiency of the different rows of the module normalized to the average charge collected in each track. This plot shows, the charge deficiency at the edges of the module, probably due to the charge distortions introduced by the gaps between the modules

A TPC WITH PIXEL READOUT

At the beginning of my project the GridPix detector was an already well-studied prototype [10]. It is a micro-pattern gaseous detector consisting of a Micromegas-like amplification mesh (grid) 50 μm above a pixel readout chip, the Timepix chip [11] with 65k pixels on an area of 14 mm x 14 mm. The integrated grid is produced by CMOS post-processing technique. The advantage over regular Micromegas meshes is that its holes are situated precisely over the pixels with a pitch of 55 μm. Pillars of SU-8 photoresist keep the grid at 50 μm above the chip surface

(see Figure 6). The chip is covered by a resistive layer of 8μm SiRN (silicon-enriched silicon nitride). Intensive studies have shown that this layer is capable of protecting the pixels against damage by discharges [12,13], which otherwise would destroy to the whole chip.
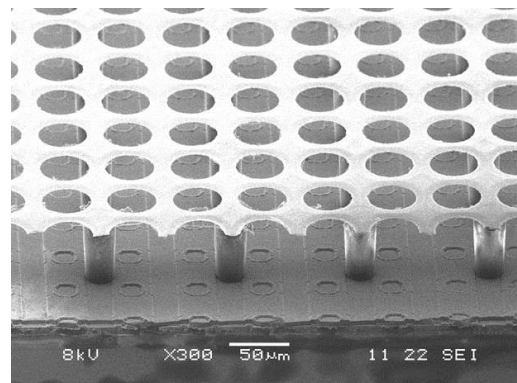

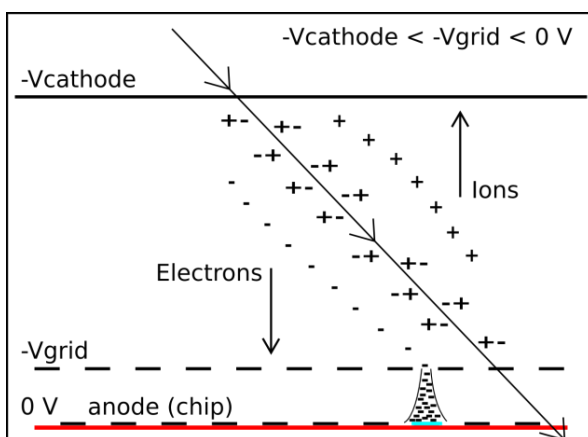**Figure 6: SEM picture of the GridPix detector.**

Figure 7: Function principle of the GridPix detector.

The functional principle of the amplification is illustrated in Figure 7: a charged particle or a photon crossing the gas volume ionises the gas and the drift field separates ions and electrons. The latter drift towards and through the grid into the amplification region. There the electric field is high enough for the electrons to multiply in an avalanche process. The charge of the resulting electron cloud is large enough to be detected by the pixels. The small pixel pitch leads to a competitive position resolution of less than 20 μm and the property of the Timepix chip allows to record the arrival time of incoming particles. With a known drift velocity in the gas one can calculate the z-coordinate. This allows for a full 3-D reconstruction of the track of the incident particle. Moreover the detector provides a high single electron detection efficiency when electrons enter different grid holes which is enhanced by the small pitch of the holes.

In my project I focus on how to use the GridPix's advantages in experiments searching for dark matter.

Dark matter Search with dual-phase Time projection chambers

The weakly interacting massive particle (WIMP) is a theoretically well-established candidate for non-luminous, cold dark matter [14]. It is supposed to interact with ordinary (baryonic) matter by elastic scattering. A resulting nuclear recoil in a preferably high-A material can reveal such an interaction. In dual-phase noble element time projection chambers (TPCs) the recoil energy leads to scintillation, a prompt signal S1, and ionisation of the scattered atoms. The ionisation charge is detected via proportional scintillation in the gas phase by photomultiplier tubes (PMTs) as a secondary scintillation signal S2. Experiments use the signal ratio of scintillation and ionisation to discriminate nuclear from electronic recoils. The loss-less drift of ionisation electrons in the liquid phase is assured by a high purity level (below ppb O_2 equivalent) of the employed noble gas. While current experiments use either liquid argon (LAr) or liquid xenon (LXe) as detection medium, the DARWIN (dark matter WIMP search with noble liquids) consortium [15] aims for a next-to-next generation multi-target experiment with both an argon and a xenon TPC, respectively, exploiting their complementary properties.

To avoid the energy conversion needed for the S2 signal detection via secondary scintillation we pursue a method of direct charge readout. We investigate how to apply GridPix as a charge sensitive detector, one candidate technology among the DARWIN R&D efforts on this subject.

Requirements on the GridPix detector for dark matter search

To use GridPix in a dual-phase argon or xenon TPC we have to study the influence of the constraining aspects inherent to this environment: the operation at the respective boiling temperatures T_{LAr} = 87 K or T_{LXe} = 165 K and the performance in quencher-free noble gas. The low temperature does not only affect the thermo-mechanical robustness of the detector, but also influences the electron multiplication, namely by increasing the gas density.

At Nikhef we performed studies of thermal robustness and outgassing properties of the used materials. This was to prepare for studying the GridPix's performance in an actual argon TPC suited for dual-phase mode, the ArDM [16] test cryostat at CERN, in cooperation with ETH Zürich. The details of the measurements are described in [17,18]. The results and implied follow-up studies are presented in the next section.

Operation in pure noble gas

We built a TPC inside a gas-tight stainless steel vessel to measure the amplification factor (gain) in different gases and at different pressures to mimic conditions in cold gas.

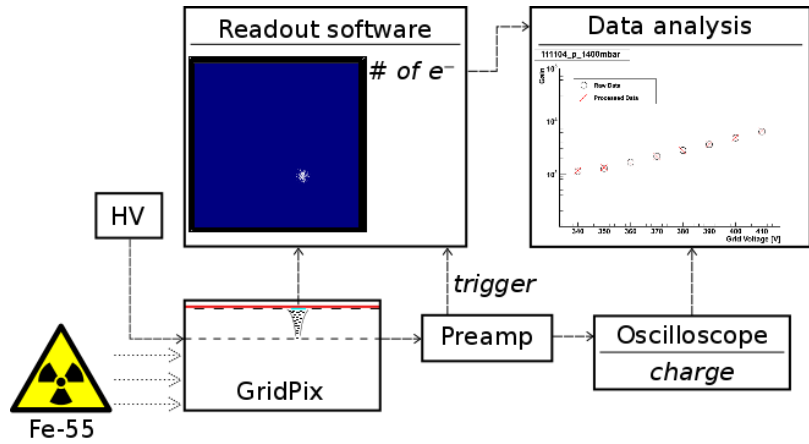Figure 8: Picture of the TPC mounted to the top flange of the vessel with data cable and preamplifier.

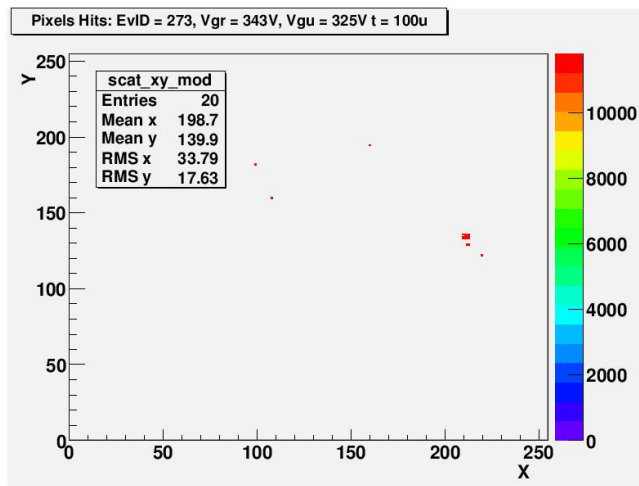Figure 9: Schematic of the procedure to measure the gas gain.

Figure 10: Display of the chip's pixel matrix with an α event at (210,130) measured in Ar 6.0.

The detector is irradiated with a radioactive source (^{55}Fe emitting 5.9 keV photons) and the events recorded via two channels: the digital signal using the chip's pixels and the analogue signal induced on the grid by an oscilloscope through a preamplifier (see Figure 8).Figure 3 shows a picture of the inner TPC containing the GridPix chip. The drift region between cathode at the bottom and guard electrode and GridPix detector at the top is 6 cm high. A 1 m long flat Kapton cable transmitting the data from the chip to the readout board outside the vessel is fed through a flange. A preamplifier is connected to the GridPix to read out the charge signal induced on the grid.

We measured the gas gain and the single electron detection efficiency for Ar/iC$_4$H$_{10}$ 90:10, our reference gas containing 10 % of quencher gas, and in Ar 4.7 (99.997 % purity). Even in absence of a quencher gas we were able to record signals implying a gain higher than 700 (the chip's sensitivity threshold). In the ArDM TPC we had the possibility to measure in argon with a purity of 99.99990 % (Ar 6.0). Triggering our acquisition on the PMT inside the TPC we were able to record events induced by 59.9 keV α's from an ^{241}Am source (see Figure 10).

Thermal robustness

After the measurement in the ArDM test cryostat we discovered that the grid ripped. Those damages were located at positions were the extremities of long (1/3 of the chip's edge) bars of the SU-8 photoresist lifted off the underlying SiRN layer. This is the result of excessive mechanical strain inside and between the layers composing the GridPix structure because of their different coefficients of thermal expansion. This could be confirmed (see Figure 11) in a controlled thermal cycle under dry nitrogen atmosphere down to a temperature of 140 K (closer to T_{LXe} than to T_{LAr}). We concluded that designing the SU-8 photoresist structures smaller and could reduce the effect of shrinking material. Moreover, placing thin SU-8 structures also all over the chip's

surface (without covering any pixels) should yield a more homogeneous strain distribution inside the aluminium grid. As a result, the exerting forces on the edges of the SU-8 can be significantly reduced. This also predicted by simulations using the finite elements method. We propose a new design of the SU-8 configuration, and Figure 12 shows an example of the new structures that are currently under production.
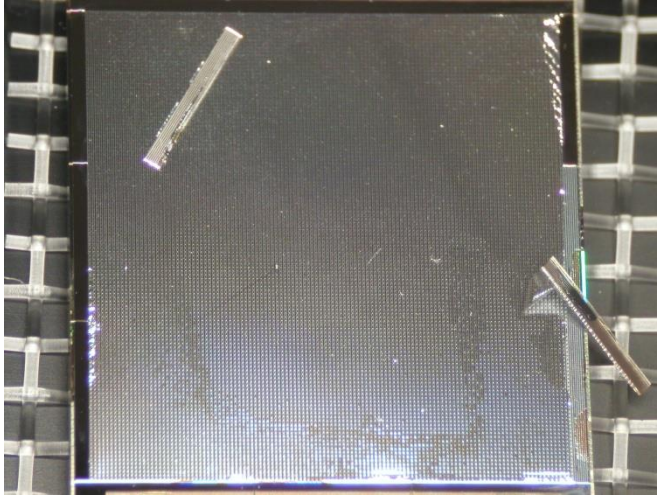

Figure 11: Picture of a damaged grid. The current SU-8 configuration leads to strong strain in the aluminium grid as well as the photoresist layer itself.
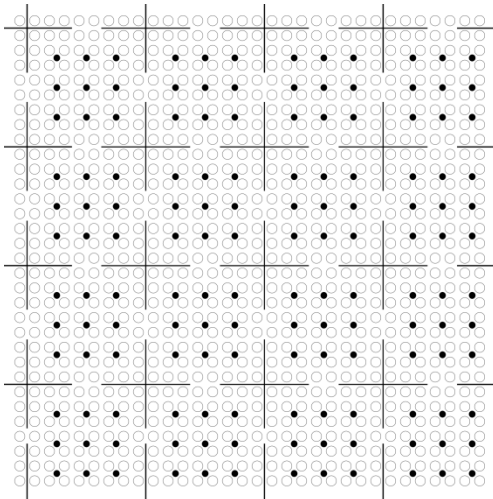

Figure 12: Detail sketch of an improved SU-8 design to withstand the thermal stress at low temperature. Open circles represent pixels, closed ones are SU-8 pillars.

Conclusion

The GridPix detector is a promising candidate for the direct charge readout in dual-phase TPCs. We showed that measurements in pure, thus quencher-free, argon are possible. We further proposed a new configuration of the layers that the GridPix is built of that will result in an improved robustness at low temperatures at the boiling point of the used noble gas. Measurements of the electron efficiency and the gas gain in pure xenon gas are part of ongoing studies at Nikhef. Their results will ultimately decide on succesfully applying GridPix in dark matter search experiments.

References

[1] F. Sauli, Nucl. Inst. Methods A, 386 (1997) 531.

[2] FOPI Collaboration, www-fopi.gsi.de

[3] PANDA Collaboration, Technical progress report, GSI FAIR, Technical Report, 2005.

[4] R. Arora et al., Physics Procedia 37 (2012) 491-498

[5] The ILD Concept Group, "The International Large Detector: Letter of Intent," 2010.

[6] T. Behnke, K. Dehmelt, R. Diener, L. Steder, T. Matsuda, V. Prahl and P. Schade, "A lightweight field cage for a large TPC prototype for the ILC," Journal of Instrumentation, vol. 5, no. 10, p. P10011, October 2010.

[7] D. Bertrand, G. D. Lentdecker, J. Dewulf, X. Jansen, C. V. Velde, P. Marage, L. Musa, L. J\"{o}nsson, B. Lundberg, U. Mj\"{o}rnmark, A. Oskarsson and E. S. amd L. \"{O}esterman, A prototype readout system for the LCTPC, 2008.

[8] R. E. Bosch, A. J. de Parga, B. Mota and L. Musa, "The ALTRO and Chip: A and 16-Channel A/D and Converter and and Digital Processor and for Gas and Detectors," in IEEE Transactions on Nuclear science, 2003.

[9] L. Jonsson and U. Mjornmark, Front-end electronics and data acquisition for the LCTPC, 2008.

[10] M. Chefdeville, Development of Micromegas-like gaseous detectors using a pixel readout chip as collecting anode, (2009), PhD thesis.

[11] X. Llopart et al., Nucl. Instr. and Meth. A 581 (2007), 485–494.

[12] V.M. Blanco Carballo, Development of Micromegas-like gaseous detectors using a pixel readout chip as collecting anode, (2009), PhD thesis.

[13] M. Fransen, GridPix: TPC development on the right track, (2012), PhD thesis.

[14] G. Steigman and M.S. Turner, Nuclear Physics B 253 (1985), 375–386.

[15] L. Baudis for the DARWIN consortium, Dark Matter Wimp Search with Noble Liquids, (2010), arXiv:1012.4764.

[16] A. Badertscher et al., Nucl. Instr. and Meth. A 641 (2011), 48–57.

[17] M. Alfonsi et al., 2011 IEEE NNS conference records, (2011), 92–98.

[18] R. Schön et al., Nucl. Instr. and Meth. A proceedings, (2012).

Project Coordinator: Wolfgang Lohmann, DESY Zeuthen.

Olga Novgorodova ESR, DESY. Supervisor: Wolfgang Lohmann

Jonathan Aguilar, ESR, AGH Cracow. Supervisor: Leszek Zawiejski, Marek Idzik

INTRODUCTION

Two calorimeters are foreseen in the very forward region of future Linear Collider detectors. The Luminosity Calorimeter (LumiCal) will perform a precise measurement of the luminosity and the Beam Calorimeter (BeamCal) will perform a fast estimate of the luminosity and assist beam tuning. Both extend the polar angle coverage of the detectors, important e.g. for tagging of high energy electrons.

A sketch of the design of the very forward region of the ILD detector is shown in Figure 1. A detailed description of LumiCal and BeamCal can be found in [1,2]. Both calorimeters are designed as compact cylindrical sandwich calorimeters.

At ILC and CLIC energies we have to tackle a new phenomenon - the beamstrahlung- leading a high radiation field at small polar angles. Sensors near the beam-pipe will be exposed to a dose of about one MGy per year. Hence very radiation hard sensors are needed. GaAs:Cr and CVD diamond sensors are under consideration[3].
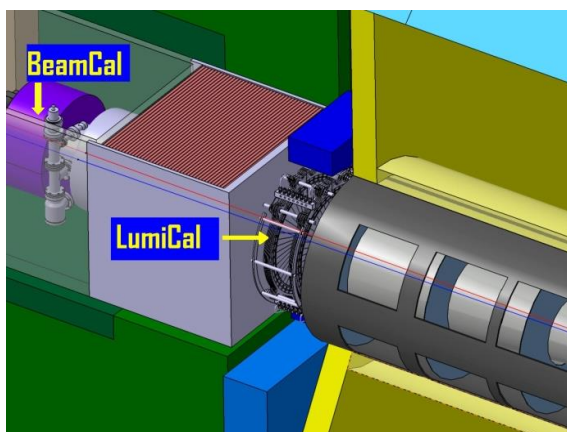
1. MONTE CARLO SIMULATION

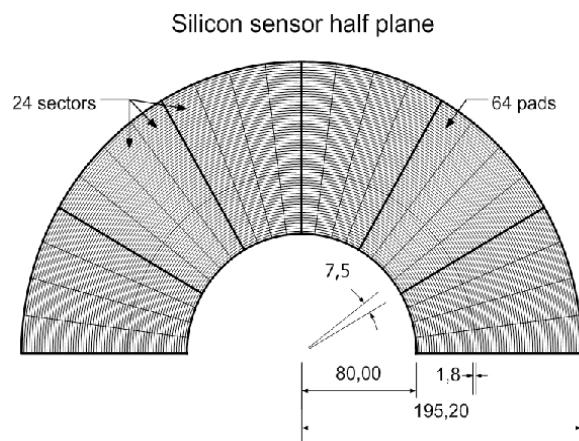**Figure 1: LumiCal and BeamCal in the ILC forward region.**

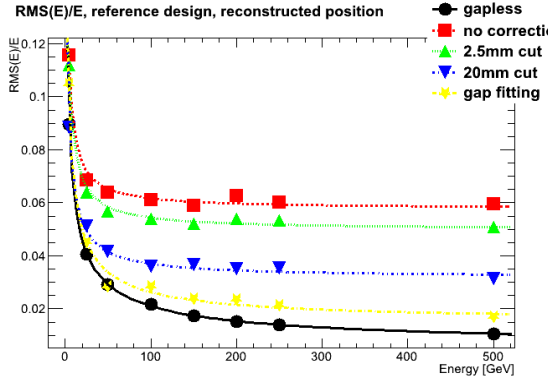**Figure 2: LumiCal sensor half-plane schematic.**

Figure 3: Comparison of the energy resolution for ideal and more realistic sensor layouts
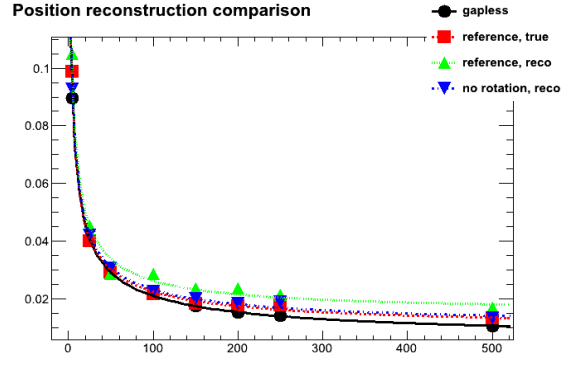

Figure 4: Comparison of the position reconstruction for different sensor layouts. "True" and "Reco" refer to whether the particle position was known from the simulation (true) or reconstructed from the calorimeter data (reco).

Dedicated simulation programs were developed for LumiCal (LuCaS) and BeamCal (BeCaS) using the Geant4 [4,5] software package. They were used to study the response of the calorimeter to electrons, originating from the interaction point of the detector.

1.1 LumiCal Simulations

The primary purpose of LumiCal is to count Bhabha scattering events to measure the luminosity of the collider. Each LumiCal barrel will consist of 30 layers of tungsten absorber disks interspersed with silicon sensors and electronics attached. The cylinder ring will be instrumented with sensors between radii of 80 mm and 195 mm. The sensor rings are divided azimuthally into twelve equal tiles, each covering 30°, as shown in Figure 2. Between each tile, there will be an uninstrumented 2.4 mm gap. Each tile is further divided azimuthally into four sectors, each covering 7.5°, and radially into 64 pads with a 1.8 mm pitch. The sensors are made from 300 μm-thick silicon with Al metallization, produced by Hamamatsu Photonics. They are described in detail in [2,6]. The primary goal of the Monte Carlo simulations was to understand the effect of the uninstrumented tile gaps on the energy resolution, given in equation 1:

$$\frac{\sigma_E}{E} = \sqrt{\frac{a^2}{E} + b^2}$$

Equation 1

The first term corresponds to the contribution from fluctuations due to the stochastic nature of showers. The second term corresponds to contributions that are independent of the energy of the incident particle; for example electronic noise or shower losses due to geometry. Here we consider the effect introduced by the tile gaps, which were not taken into account in previous studies.

A simple method of correcting for leakage in the tile gaps is to use the impact position and reject particles that are incident on or near the tile gaps. In the following analysis, this is referred to as the "gap cut" method. A more sophisticated approach is to plot the measured energy deposition as a function of the distance to the nearest tile gap (*d*), and fit the distribution as a function of d. The energy measurement can then be corrected for by a *d*-dependent scaling factor. The fitting function, given in equation 2, is an empirically determined superposition of a Gaussian distribution (to fit the peak) and a Lorentz distribution (to fit the tails).

$$1 - \frac{A}{1 + \left(\dfrac{x - C}{B}\right)^2} - D \cdot \exp\left[- F(x - C)^2\right]$$

Equation 2:

Figure 3 shows a comparison of the energy resolution for the following cases: ideal (gapless) sensor geometry; reference geometry, in which the sensors of consecutive layers are rotated by 15^{0} , without corrections; 2.5 mm-wide cut; 20 mm-wide cut; and gap-fitting correction. When the energy lost in the gaps is not corrected for the energy resolution becomes considerably worse in comparison to a gapless geometry. Applying the corrections to the shower energy measured in the gaps, the energy resolution approaches the value of an ideal calorimeter. The resolution of the position reconstruction is also studied for several designs of the LumiCal, as shown in Figure 4. The reference geometry is compared to a design without rotations. Here only a very small difference is found between the options.

Another important effect of the gap-fitting correction is that it also improves the error on the stochastic parameter. Table 1 compares the values and errors of the parameters for the different corrections. The detailed results of the MC simulations were presented in [7].

Table 3: Energy resolution parameters for the reference design.				
	Stochastic		Geometric	
	Value	Error	Value	Error
No correction	0,215	0,003	0,058	0,029
2.5mm cut	0,209	0,003	0,048	0,024
20mm cut	0,187	0,003	0,029	0,015
gap-fitting	0,201	0,001	0,010	0,005
gapless	0,203	0,001	0,006	0,003

1.2 BeamCal Simulations

BeamCal is a sensor tungsten sandwich calorimeter, positioned just outside the inclined beam-pipes. BeCaS includes its detailed geometry and material description of BeamCal and a simplified geometry of surrounding detectors. Beamstrahlung, simulated using the Guinea-pig package [8], creates after each bunch crossing a widely spread background of low energy electrons on BeamCal. The segmentation was optimized to get the maximum efficiency for single high energy electron identification and reconstruction on top of the background [9]. The example of the reconstruction efficiency as a function of distance is shown in Figure 5 (left). Electrons with 50GeV (triangles), 150 GeV (squares) and 250 GeV (dots) were reconstructed on top of beamstrahlung background. The efficiency is nearly 100% at larger polar angles and drops approaching the beam-pipe.

2 TEST BEAM MEASUREMENTS

LumiCal sensors are made by Hamamatsu Photonics of 300 µm-thick silicon wafer with n-doped bulk and p-in-n pad diodes. BeamCal sensors are grown from GaAs by LEC doped with a shallow donor and compensated with Cr. The sensor thickness is 500 µm.
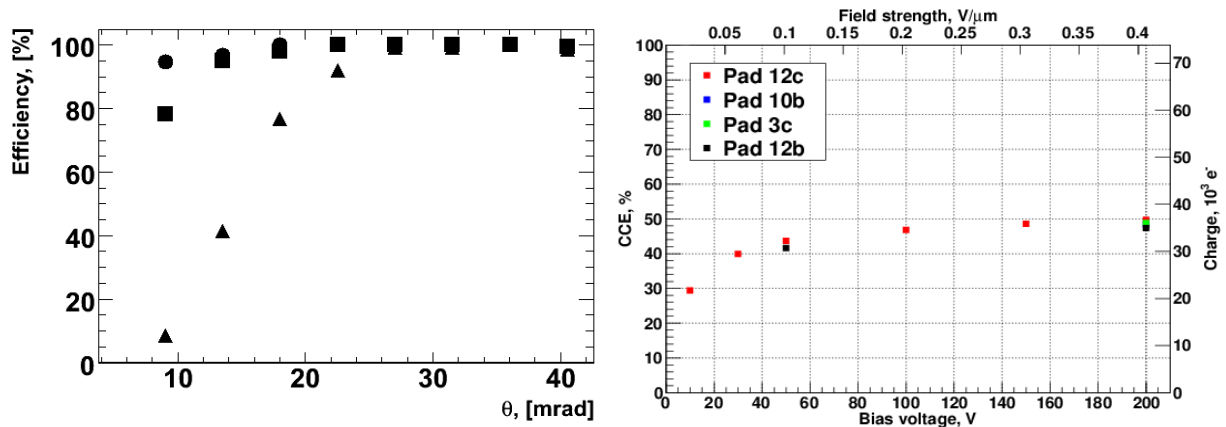
Figure 5: Left: The reconstructin efficiency for single high energy electrons in BeamCal as a function of the polar angle. Right: The charge collection efficiency of a GaAS sensor as a function of the applied voltage.

Sensors were first investigated in the laboratories in AGH-UST, DESY and IFJPAN. Using a probe-station the dark current and the capacitance of each pad was measured as a function of the applied voltage. For the silicon sensors full depletion was reached at voltages around 40 V. The measurements of the GaAs sensors show the characteristics of a resistor.

The charge collection efficiency (CCE), defined as the ratio between collected and created charge in the detector, was measured for GaAs sensors as function of the applied voltage, as shown in Figure 5(right). It shows saturation around 50 % CCE at 100V.

Front-end ASICs and ADC ASICs, as shown in Figure 6, were designed in AGH-UST, produced and tested. The performance was in agreement with the specifications [10]. Using special fan-outs the ASICs were connected with sensor pads. An assembled sensor plane with 32 pads connected to ASICs is shown in Figure 7. The functionality of the whole system was first tested in the laboratories [11]. The performance was then studied in a 4 GeV electron beam at the DESYII accelerator.

2.1 Test beam setup

The assemble sensor plane was positioned within a silicon strip beam telescope [12] as shown in Figure 8. Three telescope planes in front of the sensor plane under test were used to reconstruct the trajectory of each beam electron, allowing to predict the impact point on the sensor plane. The scintillators in front and after the setup form a trigger starting the readout of the telescope and the signals from the sensor plane. About 5 million events have been recorded for different areas on the sensors and with different settings of the front-end ASICs (low and high amplification of the preamplifier and shaper).
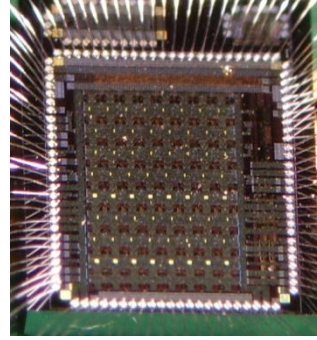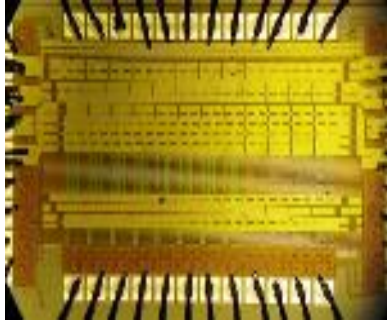
Figure 6:A front-end ASIC (left) and an ADC ASIC (right)

2.2: Test beam results

The signal from a sensor pad was split after amplification and digitized both with an external flash ADC and with the ADC ASIC on board. The result is shown in Figure 9. Apart of the different sampling rate, the results are identical.

From the amplitude and noise spectra, as shown in Figure 10 (left), the signal-to-noise ratio was determined. It amounts to about 20 for all channels on LumiCal and BeamCal sensors, as shown in Figure 10 (right).

The telescope is used to predict the impact point on the sensor plane. In case the signals on the corresponding pads are above a threshold, a certain color is assigned. As an example, the distribution of the impact points on

Figure 8: Experimental setup used for beam test measurements (left). The BeamCal sensor (right).

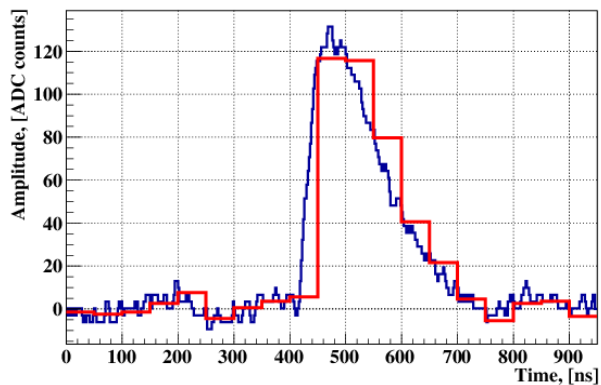**Figure 7 A sensor plane assembled with front-end and ADC ASICs**

Figure 9. A signal digitised with an external 500 Ms/s ADC (blue) and with the ADC ASIC on board (red)
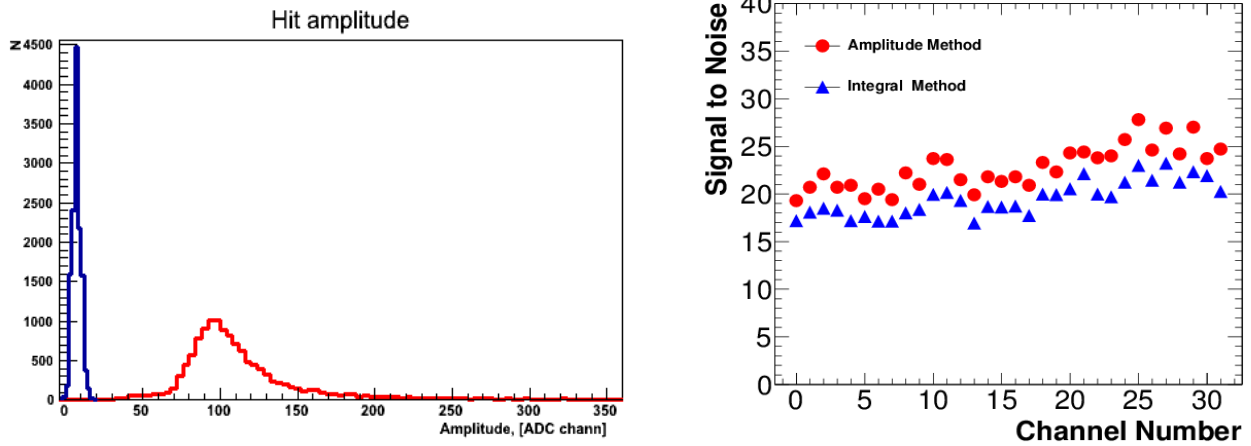
55

Figure 10: Left:Amplitude spectra of the noise (blue) and signals from electrons (red), Right: The signal-to-noise ratio of 32 pads readout from a sensor.

the BeamCal sensor is shown in Figure 11 (left). The pad structure of the sensor is nicely visible.

In the gap between pads the electric field is distorted which may have impact on the charge carrier drift and hence the signal size. In Figure 11 (right) the signal size is shown as a function of the coordinate crossing the pad boundary. A reduction of the signal size of about 10 % was observed at the position of the gap.

Data were also taken with tungsten plates of different thickness installed in front of the sensor planes to measure the shower profile as a function of the absorber thickness.

Figure 12 shows, as an example, the energy deposited in the instrumented area in a depth of 2 X_0 and 4 X_0. The measurement results (red) were compared with prediction of Geant4 Monte Carlo simulations (blue). Good agreement was found between them. The average charge deposited in instrumented area as a function of tungsten thickness is also shown in Figure 12. Again, good agreement with Monte Carlo was found.

2.3 Deconvolution Method

The deconvolution method allows a reduction of the amount of data and recovery of pile-up signals, keeping precise time and amplitude measurement. Here the deconvolution method is used to decompose the signal from the sensor by assuming a known pulse shape. The deconvolution method is applied in the data analysis [13]. Data taking was synchronized with the beam clock. From the deconvoluted information the signal amplitude and the charge has been reconstructed and compared to the measurement of the full signal.
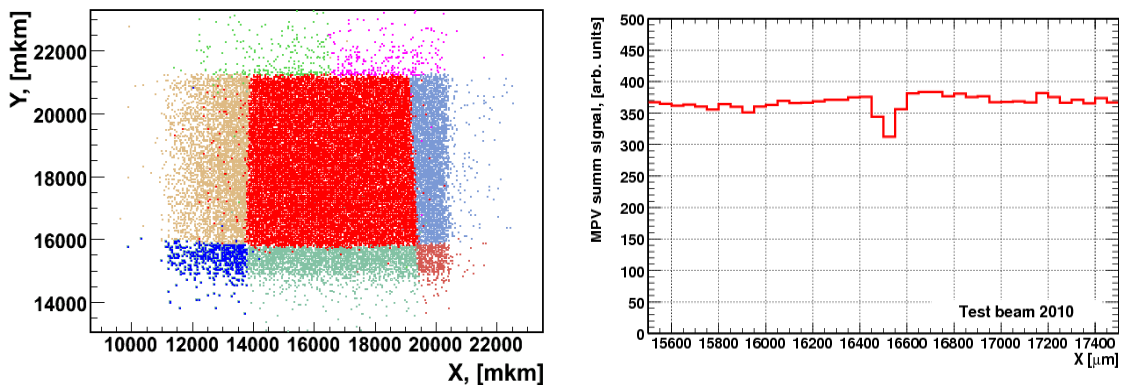

Figure 11: Left: The BeamCal pads structure obtained using the telescope at 2010 test beam . Right: The mean value of the sum of signals from two adjacent pads crossing the border between them at 16500 μm.

Excellent proportionality was found as shown in Figure 13. The signal-to-noise ratio was maintained.

3 CONCLUSIONS

Silicon and GaAs sensors were developed and characterized for the use in the forward calorimeters LumiCal and BeamCal. Using front-end and ADC ASICs developed in AGH-UST, prototype sensor planes for LumiCal and BeamCal were assembled and investigated in an electron beam. The system was operated very stable over several weeks in a joint effort of groups from AGH-UST, IFJPAN and DESY, and data were taken.

The signal-to-noise ratio for minimum ionizing particles was found to be around 20. The homogeneity of the sensor response is very good. In the gaps between pads a signal drop of about 10% was observed.

First estimates of the shower profile as a function of the absorber thickness were made and compared to a simulation with GEANT4. Good agreement was found. A signal convolution technique to reduce the amount of digitized data and cope with pile-up was successfully tested.
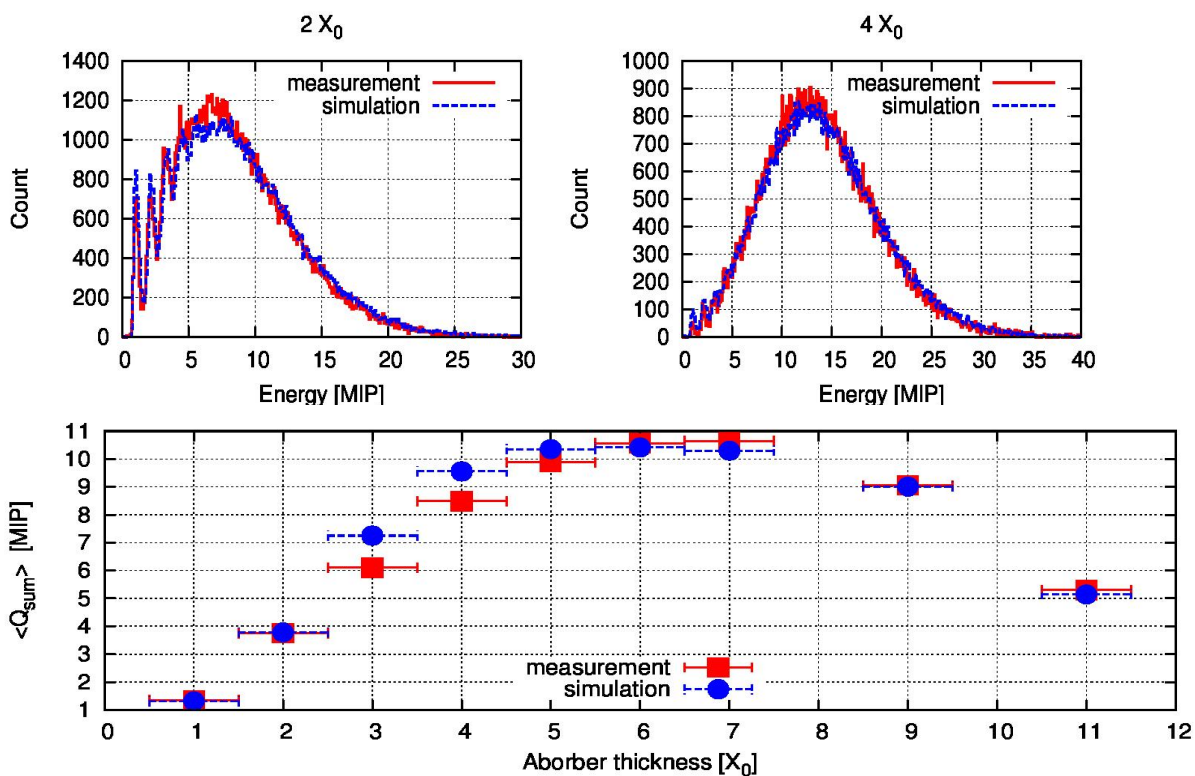

Figure 12: Energy deposition in instrumented area under the 2 X_0 (up left) and 4 X_0 (up right). Average charge deposited in instrumented area as a function of tungsten thickness (bottom).
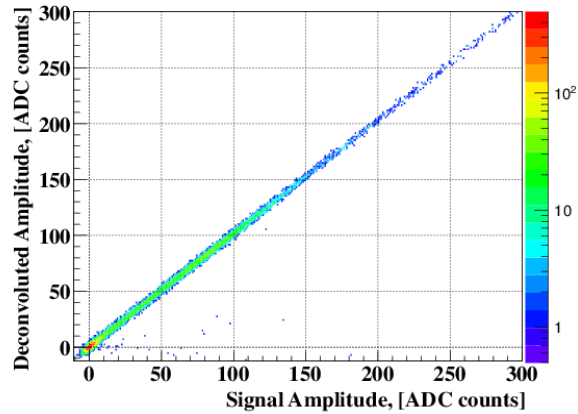
Figure 13: Comparison of the amplitude obtained after deconvolution with the amplitude measured by the flash ADC.

REFERENCES

[1]   W. Daniluk, E. Kielar, J. Kotula, A Moszczynski, K. Oliwa, B. Pawlik, W. Wierba, L. Zawiejski, and J.A. Aguilar. Redesign of LumiCal mechanical structure. Eudet-Memo-2010-06, 2010. Available at http://www.eudet.org/e26/e28/.

[2]   H. Abramowicz et al. (J. Aguilar, P. Ambalathankandy, M. Idzik, W. Lohmann, O. Novgorodova) , Forward instrumentation for ILC detectors, 2010 JINST 5 P12002..

[3]   K. Afanaciev (O. Novgorodova) et al. , Investigation of the radiation hardness of GaAs sensors in an electron beam ,JINST 7 (2012) P11022, Ch. Grah et al., Polycristalline CVD diamonds for the Beam Calorimeter of the ILC, IEEE Trans. Nucl. Sci.56, 462, 2009.
[4] J.Allison et al. Geant4 developments and applications. IEEE Transactions on Nuclear Science, 53(1):270–278, 2006.

[5]   S.Agostinelli et al. Geant 4 - a simulation toolkit. NIM-A, 503(1):250–303, 2003.

[6]   J. Blocki, W. Daniluk, E. Kielar, J. Kotula, A. Moszczynski, K. Oliwa, B. Pawlik, W. Wierba, L. Zawiejski, and J. Aguilar. Silicon sensors prototype for LumiCal calorimeter. Eudet-Memo-2009-07, 2009. Available at http://www.eudet.org/e26/e28/.

[7]   Jonathan Aguilar. Luminomiter for future International Linear Collider – simulation and tests results, TIPP 2011, 8-14 June 2011 Chicago, USA.

[8]   D. Schulte, Beam-beam simulations with guinea-pig, CERN-PS-99-014LPCLIC-note 387, 1998.

[9]   O. Novgorodova, et al. , Forward calorimeters for the future electron-positron linear collider detectors, PoS QFTHEP2010 (2010) 030.

[10]   M. Idzik et al., Development of front-end electronics for the luminosity detector at ILC, Nucl. Inst. And Meth. A 608, 169, 2009; A 10-bit multichannel digitizer ASIC for detectors in particle physics experiments, IEEE Trans. Nucl. Sci. 59, 294, 2012.

[11]   S. Kulis, et al. , A general purpose multichannel readout system for radiation detectors , JINST 7 (2012) T01004. [12] S.

[12]   MVD telescope web resource. http://www.desy.de/~gregor/MVD_Telescope/short_intro.html

[13]   Kulis and M. Idzik, Triggerless readout with time and amplitude reconstruction of event based on deconvolution algorithm , Acta Phys.Polon.Supp. 4 (2011) 49.

PROJECT 7: ADVANCED PHOTODETECTORS

Project Coordinator: Christian Joram

Paolo Beltrame, ER, CERN. Supervisor: Christian Joram

Matthieu Heller, ER, CERN. Supervisor: Christian Joram

INTRODUCTION

The project comprised the conception, the performance evaluation and the full characterization of two detection systems using photo detectors and scintillating materials. Two ER's based at CERN have successively worked on these two detectors in the different development and operation phases.

The first detection system called Axial-PET (AX-PET) is dedicated to positron emission tomography (PET). This detector is a novel concept in terms of geometry and composition for PET imaging systems where long crystals are arranged axially with respect to the scanned object. It allows for a full decoupling of sensitivity and spatial resolution and provides a parallax error free reconstruction. When joining the project, the design and conception phases of these detectors were completed and the characterization phase was starting. Today, four years later, a demonstrator scanner has been fully characterized and it has shown its great potential towards a real application.

The second system is the ALFA (Absolute Luminosity For ATLAS) detector. It is a sub-detector of ATLAS, one of the four major experiments of the LHC project. It aims to measure the luminosity, a crucial quantity to know in order to measure production cross sections of particles, such as e.g. the Higgs boson. The ER's have participated to test beam campaigns and commissioning work inside the LHC tunnel. The detectors behaviour has thus be thoroughly understood before any physics analysis was done. Absolute luminosity measurement requires the LHC to run in a very particular mode. This could not yet be achieved in the first two and a half years of operation. As intermediate step, however, the total cross section of proton-proton scattering could be determined.

In the following we will present the two detection systems, focusing on their characterization and the latest results.

1   THE AX-PET DEMONSTRATOR

Excellent spatial resolution and high sensitivity are crucial aspects for PET imaging devices. In addition, the combination with Magnetic Resonance Imaging (MRI) is becoming essential. The Axial-PET project aims to prove the feasibility and performance of a new PET instrument. This apparatus will be capable to produce biological images free from parallax error and to improve independently the sensitivity and the resolution – without the need to stoop to compromises, as it is the case in standard PET devices. As additional feature Ax-PET can also provide the possibility to discriminate Inter Crystal Scattering (ICS) events and operate in the presence of magnetic field, therefore together with MRI.

1.1 The detector principle

The basic principle of this novel detector consists in the axial arrangement of long scintillation LYSO crystals around the Field Of View (FOV) and Wave Length Shifter (WLS) strips orthogonally positioned to the crystal direction. The crystals are placed on different layers one behind the other and staggered for full coverage. They provide information on the x and y (transverse) position of the detected 511 keV gamma ray together with the energy released by the photoelectric interaction. Behind each crystal layer, a WLS strips array collects the light escaping from the crystal as shown on Figure 8. Via a centre of gravity clustering technique, the z (axial) coordinate is determined precisely. This novel geometry allows for a decoupling of sensitivity and spatial resolution. In fact the sensitivity can be improved by increasing the amount of layers and the spatial resolution by changing the crystal size.
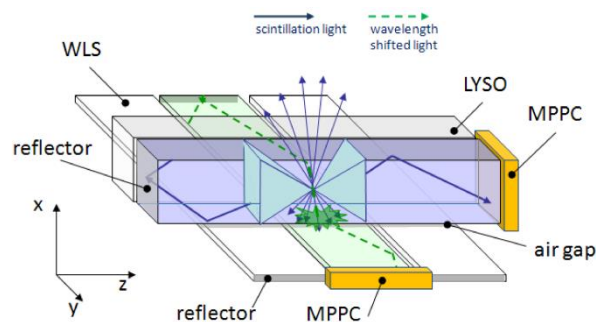

Figure 8: Scheme presenting the detection principle of the AX-PET concept. The photoelectric interaction releases scintillation light in the LYSO crystal. Part of this light is trapped inside and reaches the photodetector by internal reflections. Another part escapes and illuminates a set of WLS strips.

1.2 The project

The international AX-PET collaboration aimed at the construction of a fully operational two-modules demonstrator. Each module consists of 48 LYSO crystals (St. Gobain), 10 cm long with a cross section of 3×3 mm^2, assembled in a stack of 6×8 bars, and 6×26 WLS strips of 0.9×3×40 mm^3, placed behind each crystal layer. The optical photons in the LYSO are read out by Multi Pixel Photon Counters (MPPCs) from Hamamatsu (S10362-33-050C, 3600 cells of 50×50 μm^2) with an active area of 3×3 mm^2. The MPPCs for the WLS readout are custom designed (OCTAGON-SMD, 782 cells of 70×70 μm^2, dimension 3.22×1.19 mm^2). The signals are amplified and fed into a 128 channel self-triggering readout ASIC VATAGP5 (Gamma Medica-IDEAS), controlled by a VME DAQ system.

In order to mimic the performances of a full ring camera, the two modules have been mounted face-to-face, on a gantry with a rotating support holding the radioactive source in the middle (see Figure 9). Therefore, by rotating the source, it has been possible to reconstruct the image from different perspective angles. Moreover, to extrapolate the performances with an extended field of view, the second module of the demonstrator has been mounted on a horizontal rotating harm allowing a displacement of the module from the 180° alignment.
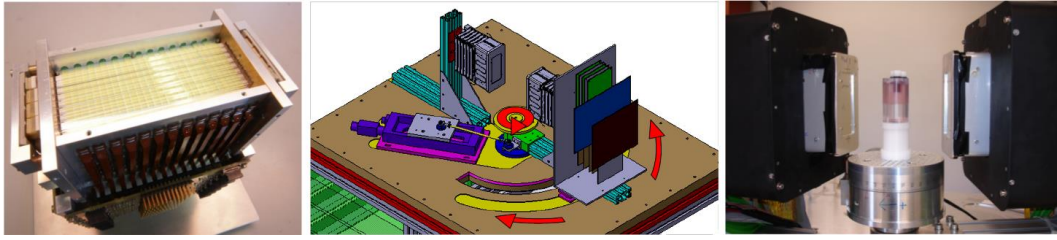
Figure 9: From left to right. View of a module after assembly; Scheme of the demonstrator gantry; View of the two modules facing each other with the NEMA phantom in between

1.3 Point-like source measurements and results

First measurements with ^{22}Na point-like radioactive sources have demonstrated the validity of the detector design principle and of the set-up. The main performance figures are:

- Average energy resolution of the 128 LYSO crystals: $\Delta E/E = 11.8\%$ FWHM
- Spatial resolution:
  - Axial:
    - Single module $\Delta \square \approx 1.8$ mm FWHM
    - Module in coincidence (confocal resolution), both in face-to-face and oblique configuration: $\Delta z \sim 1.35$ mm demonstrating a parallax-error free reconstruction
  - Transaxial $\Delta x, y \approx 2$ mm FWHM

The characterization of the AX-PET modules has been summarized in a detailed article [1].

Dedicated Monte Carlo code for the detector simulation has been developed and an excellent agreement with data has been found. An article dedicated to the simulation studies will be published soon.

1.4 Extended source measurements and small animal imaging

The demonstrator performance has been further tested in measurement campaigns, in collaboration with the ETH-Zurich and the company AAA in Saint Genis (France), using extended sources, capillaries and phantoms.

On Figure 10, the reconstructed images of the three different regions of the NEMA phantom are shown. This mouse-like phantom aims to assess the performance of the detection system in terms of spatial resolution, homogeneity and contrast rendering. The smallest rod visible is 1 mm in diameter and is reconstructed with an apparent diameter of 1.6 mm FWHM. The results obtained are comparable to the best commercial scanners, which is a very promising achievement, considering the challenges related to the limited geometry of the demonstrator scanner.
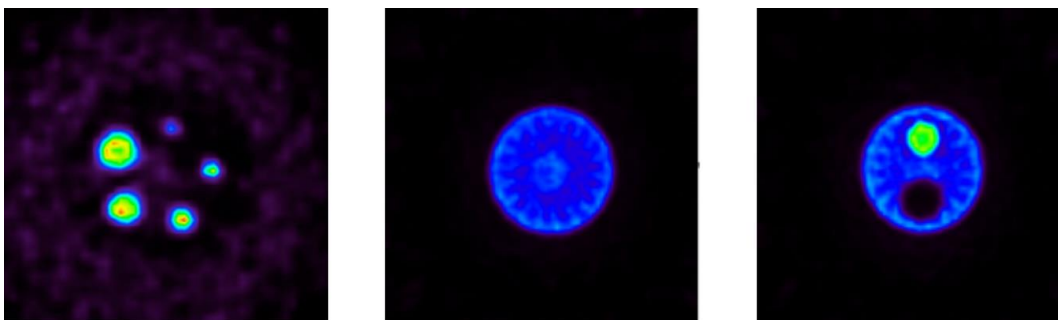

Figure 10: Views of the tomographic reconstruction of the NEMA phantom. From left to right: Spatial resolution assessment region, homogeneity region, contrast region

Finally, imaging of small animals (mice and rats) has been performed at the radio-pharmaceutical institute of the ETH Zurich. The same animals were scanned with a commercial device, the eXplore VSTA CT-PET scanner from GE health care. This comparison confirmed again the excellent capabilities of the AX-PET concept. Figures 11 and 12 display the reconstructed images of two rats, one injected with FDG and the other with 18F in aqueous solution. An article is in preparation summarizing the latest results in terms of reconstructed images. It is intended for publication in a journal for biomedical research.
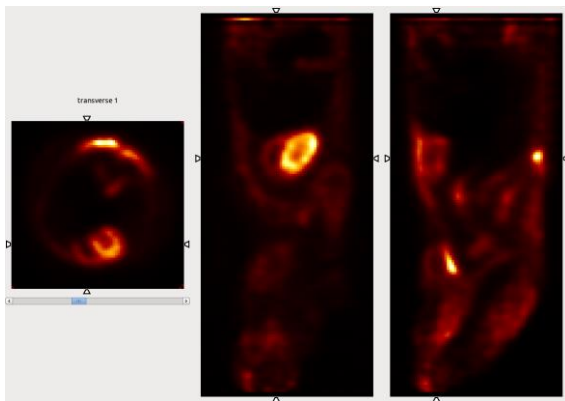

Figure 11: Different views of the tomographic reconstruction of a rat with FDG. The heart and one of its cavities are clearly visible.
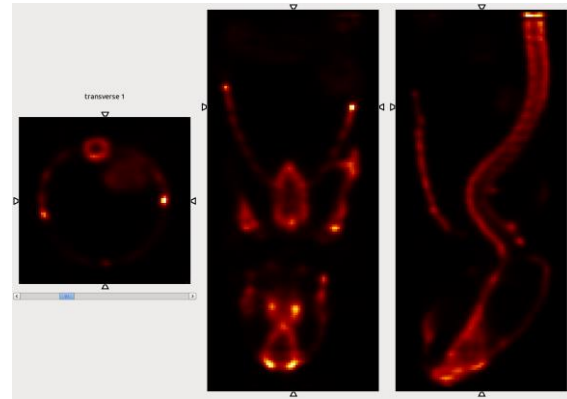
Figure 12: Different views of the tomographic reconstruction of a rat with 18F. The spine and the ribs are very well rendered.

1.5 Rates prediction

The system as described in the previous sections leads to several challenges for the tomographic reconstruction. These are for example the different nature of the transaxial (discrete) and axial (continuous) co-ordinates, the gaps in the geometry, and the long acquisition times. In this section we will only deal with the last part which consists in taking into account the decay of the source activity during the acquisition.

The operation of our demonstrator set-up with only two modules is compromised by the lack of azimuthal coverage and a limited data acquisition (DAQ) rate. As a consequence of the decaying phantom activity, we are confronted with changing operational conditions during the run. Dead time and saturation effects can mask the underlying geometrical information.

We have first developed a model of the DAQ rate as a function of the activity [2]. This proceeds via the understanding of the single module and the trigger rate (coincidence rate). All these rates are accessible via a VME scaler which is integrated into the DAQ system.

The hit rate of a single module depends on the phantom activity, the detection efficiency of the module and the solid angle of the respective phantom-module configuration. The behaviour is not completely linear as at high activity the system starts to be paralyzed due to pile up events. This affects in the same way the coincidence rate, which is derived from the single rate by a geometrical reduction factor.

The data acquisition rate brings some new features related to data processing. Each event takes a minimum amount of time to be processed, this is called the dead time. This time limits the maximum rate the acquisition

system can handle. This component is called non paralyzable as it cannot fully block the system. On the other hand, the fact that the processing time depends on the amount of channels to be read out, at high activity, the dead time will increase due to pile-up and tend to paralyze the system. The time constants related to these two components where measured and match the result of the fitted values. Figure 13 shows the fit of the DAQ rate as a function of the activity.

χ² / ndf	8.45 / 381
$\tau_{p, Sgl}$	3.896e-07 ± 0
$A\in^2$	0.003943 ± 3.884e-05
τ_p	6.411e-06 ± 6.585e-08
τ_{np}	5.734e-05 ± 2.235e-07

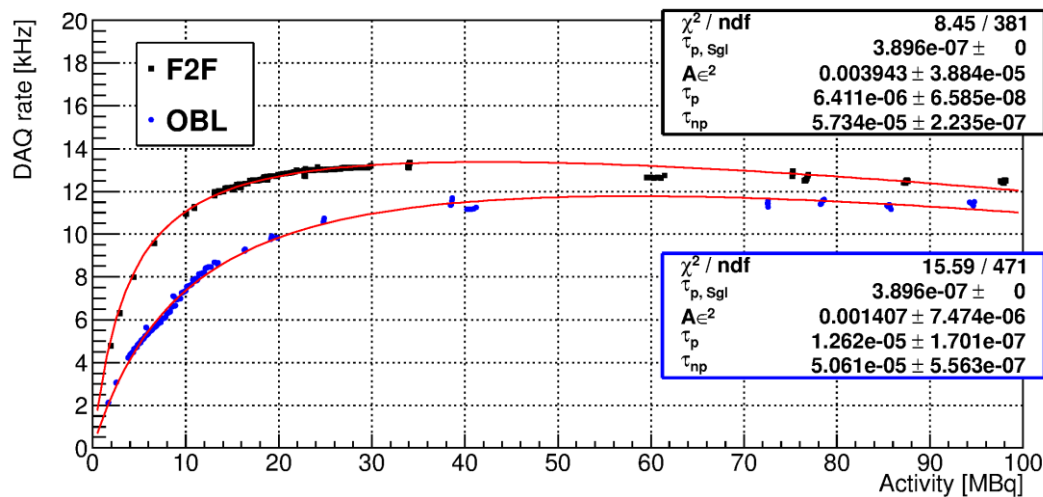| χ² / ndf | 15.59 / 471 |
$\tau_{p, Sgl}$	3.896e-07 ± 0
$A\in^2$	0.001407 ± 7.474e-06
τ_p	1.262e-05 ± 1.701e-07
τ_{np}	5.061e-05 ± 5.563e-07

Figure 13: DAQ rate as a function of the activity for the face to face and the oblique configuration. The paralyzable behaviour is clearly visible as the rate start to decrease at activities > 50 MBq

In order to extract the geometry from the data without artefacts, a short scan of ten second per step is performed. In such a way, only the geometrical component remains and is responsible for rate variations. However, not all the recorded events are useful for the reconstruction. Indeed only events where one and only one 511 keV photon was detected per module and properly associated to a WLS strip cluster are used. This type of events is called golden events and one need to calculate their fraction as a function of the activity. Once this is done, the various pieces of information are combined and the optimum step times of the entire scan can be calculated. This was used to optimize the scan duration in the last phantom imaging campaign.

1.6   Using digital Silicon Photomultipliers (dSiPM) from Philips

Since 2005, the Philips Company has developed a new type of photodetectors. These detectors also consist in arrays of G-APD, but instead of giving an analogue output signal, a digital output is provided.

The device has consequently several features which are new compared to standard analogue photo detectors. In particular, a trigger network and a so-called state-machine deal with the acquisition logic. It allows for instance to trigger on the first detected photon enhancing the timing capabilities. These new detectors are very promising for application in PET, in particular Time-Of-Flight PET. The goal of using these detectors was to demonstrate that we could reach the same performances as before but with a significant gain in terms of coincidence time resolution. The most important results will be described in this section.

The first part of the characterization was conceived to reproduce the tests done on the AX-PET demonstrator, with a very similar test protocol. Figure 14 shows various setup used for this purpose.

The advantage of a digital device is that the output is directly the amount of photo-electrons. Even though the output always has to be corrected for saturation, it is straight forward to measure the light yield. With these photo-detectors, an average of 1500 photo-electrons is detected for 511 keV photo-interactions. This result is

slightly better than the one obtained with the analogue devices. This is due to the better photo detection efficiency of the digital devices.

An energy resolution around 12 % (FWHM) reading the LYSO from a single side was found. When the aluminium coating is removed and a second detector is connected at the other end of the crystal , the energy resolution improves and reaches around 10 %.
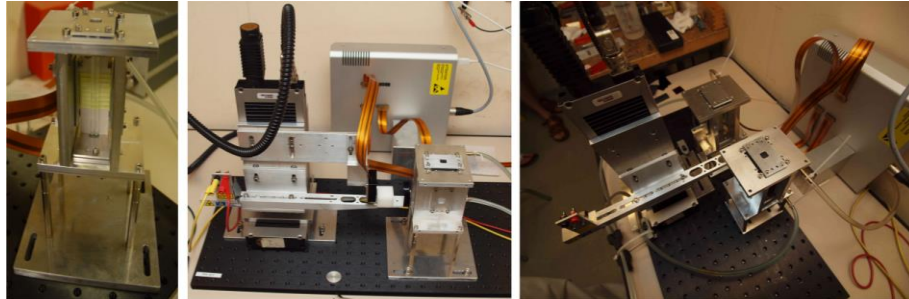

Figure 14: From left to right: view of the mini AX-PET module using dSiPM, setup for single module characterization, setup for characterization of two modules in coincidence

As far as the spatial resolution is concerned, it has to be mentioned that the WLS strips positioning slightly differs from the original AX-PET set-up. Instead of having a pitch of 3.2 mm, 4 mm is now in use. In this respect we do expect some differences in term of axial resolution. Indeed, what was not observed in AX-PET was the fact that depending on where the photoelectric interaction occurs in the LYSO crystal, the resolution changes. When the interaction takes place in between two WLS strips, the resolution is worse than if it occurs centred on one WLS, ranging from 1.2 to 1.8 mm FWHM. In coincidence a confocal axial resolution of 1.15 mm FWHM was obtained.

The timing performance has been assessed using two different set-ups. The first one uses the same principle as the AX-PET demonstrator, i.e. reading the crystal at one extremity while the other end is coated with an aluminium reflective layer. In the second set-up, as explained in the previous paragraph, the coating is removed and replaced by another dSiPM tile.

In the first setup, the time difference between the two modules must be corrected taking into account the location of the photo-interaction on the z-axis. The further the interaction occurs from the tile, the longer it takes for the first photon to be detected. Measuring the position with the WLS strips allows compensating for this effect and reaching a coincidence time resolution around 265 ps (FWHM).

With dual sided readout, the path length effect described above is compensated by averaging the times measured at the two extremities. This results in an improvement of the coincidence time resolution towards an average value of 200 ps. This latest result is highly competitive and very encouraging for a time-of-flight PET application of the AX-PET concept.

1.7   Conclusion and future

All the measurements and imaging test campaigns have demonstrated the great capabilities of the AX-PET concept. They have not only proven the expected decoupling of spatial resolution and sensitivity but also revealed an overall performance which is comparable and in several respects better than commercially available device. The difficulties related to an incomplete angular coverage and limited readout electronics could be overcome. In addition, the axial geometry leads to a parallax error free detector. Lately, a simulation of a hypothetical full ring scanner made of AX-PET modules has been set up in order to predict its

performance. As the simulation model was validated before with experimental results, its outcome will help the collaboration to extrapolate all results found to a realistic geometry.

In parallel to this simulation work, the tests using the dSiPMs from Philips are still on-going and the very promising results have encouraged the company to collaborate even closer. These devices represent a very promising solution towards TOF-PET applications.

2   THE ATLAS-ALFA DETECTOR

An accurate knowledge of the LHC luminosity is crucial for a precise determination of Standard Model processes and New Physics discoveries, and for precision measurements involving the Higgs boson. The ALFA (Absolute Luminosity For ATLAS) [3] detector consists of a high-precision scintillating fibre tracker designed to determine the absolute LHC luminosity at the ATLAS interaction point (IP1) with a precision at the level of ~3%. Such precision can be reached measuring the differential elastic cross section of proton-proton scattering at very low scattering angle where the Coulomb forces dominate. However, the luminosity measurement is the ultimate goal which will only be fulfilled after the long shutdown of the LHC in 2013-2014. Several intermediate steps are required to obtain the proper accelerator set-up. During these steps the proton-proton total cross section and the nuclear slope will be measured. In order to perform any of these measurements inside the LHC tunnel, a thorough understanding of the detector system is required and the two ERs have greatly contributed to it.

2.1   The detector principle

The ALFA detector is mounted in so-called Roman Pots (RP), which allows to approach the LHC beam to about 1 mm distance. The entire detection system is made of eight RPs. On each side of the IP1, two stations are located at 237 and 241 m. A station is made of an upper and a symmetric lower detector. A drawing of the ALFA detector installed down into the LHC tunnel is shown in Figure 15, together with a zoom of one RP and a more detailed view of the detector.
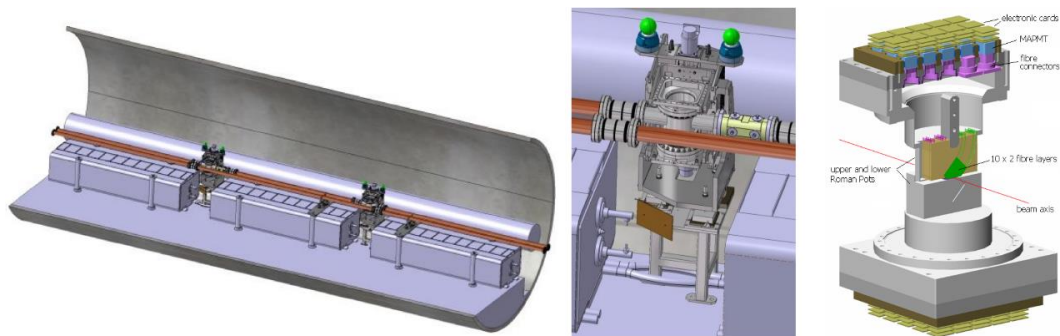
Figure 15: From left to right: View of two stations installed on side of the IP1, closer view to a single station, detail of an ALFA station and its main scintillating fibre tracker

Inserted in a RP, the main detector (MD) consists of ten plates. The plates are made of two layers arranged at +45° and -45° respectively, and each layer has 64 scintillating fibres of 0.5×0.5 mm^2 cross section. The layers are staggered such that the overlap is minimized in order to improve the spatial resolution. The fibres are then coupled to 64 channels Multi-Anodes PhotoMultiplier Tubes (MAPMT).

All detectors have two so-called Overlap Detectors (OD). Their purpose is to provide information on the relative vertical positioning of the two main detectors. The ODs consist of three layers of 30 scintillating fibres horizontally arranged, thus providing a vertical measurement only. When the upper and lower detectors are

brought to data taking position, the horizontal trackers of the upper and lower detectors overlap. Combining the two measurements allows determining the distance.

2.2 Test beam measurements campaigns

The detectors have been tested at CERN using a pion beam in 2009 and in 2010. The last campaign has involved six of the eight ALFA detectors installed currently in the tunnel and for the first time also the ODs have been put in operation together with the whole ALFA readout chain. These test beam periods have demonstrated a performance fully matching the expectations. The layer efficiency, which combines the fibre efficiency and the filling factor, was measured around 92% for all detectors. This high efficiency results in a reconstruction efficiency close to 100%. The spatial resolution was found to be better than 30 microns and uniform across the entire active area. Concerning the distance measurement with the ODs, a precision of 30 microns was reach on all stations. In order to be able to use the calibration constants determined during these test beam in the tunnel, all stations, with one exception, were installed in the exact same configuration as they were tested.

During the last test beam, the cross talk between adjacent fibres was found to be much higher than expected. The consequence of such a cross talk is a degradation of the spatial resolution. It was identified to be related to the light escaping at the lower edge of the detector, bouncing on the stainless steel window of the RP and entering in an adjacent fibre. This was solved by spraying a black light absorber on the inner surface of the RP.
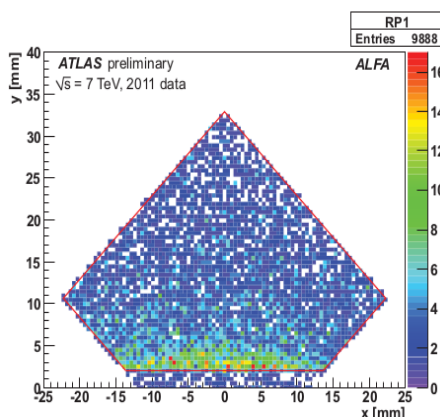
2.3 Installation in the tunnel and commissioning

Figure 16: Superposition of reconstructed tracks in garage position. The enhancement at the detector edge reflects the influence of the beam screen.

During the Christmas shutdown of 2010, all stations, electronics, and data acquisition systems were installed in the tunnel. The first results were obtained soon after, showing a perfect functioning of the entire detection chain. The first tracks were observed in the so-called garage position, i.e. when the RPs were fully retracted in the shadow of the collimator as visible in Figure 16.

However in this early phase, the detectors were not allowed to approach the LHC beam for safety reason. The positioning system had to be tested and validated. This was done early in 2011 in order to achieve a first physics run in June 2011.

2.4 Data taking and physics analysis

In order to detect the elastically scattered protons at 240 m from the interaction point, the settings of the magnets must be changed in order the separate these protons from the beam core. This is done using a so-called parallel-to-point focusing optics, which acts as a separator for protons having a larger angle than the average value (called beam divergence). This requires among other changes to increase the beam size at the interaction point and to force the particle to oscillate in the vertical plane by 90 degrees. As this mode is radically opposed to the nominal settings it requires machine development time and a dedicated time slot for the physics run. As the LHC is mainly dedicated to Higgs boson search, the specific ALFA runs are rare (2-3 per year) and must be exploited as efficiently as possible. The most important run taken so far was done in

October 2011 where around 800k elastic events were registered. The results presented in the coming sections are based on its analysis.

2.5   Alignment procedure

In order to measure the scattering angle at the interaction point it is necessary to measure the proton transverse position in the same reference system as the one in which they were scattered. This requires determining the relative position of all detectors with respect to the circulating beam.

The starting point of the entire procedure is the measurement of the distance between upper and lower detectors in the four stations. This is done using the ODs described earlier. Thanks to the calibration done during the test beams, this measurement is done with a precision in the order of 30 microns and fixes locally the relative position between the upper and lower detectors.

The next step is to align the stations in a unique reference system, the beam reference system. The main assumption to perform this operation is that the scattering picture is symmetric both in the horizontal and vertical planes. The horizontal alignment is by far simpler as the acceptance losses are small. The method consist in applying a linear fit to the distribution of all tracks in the (x, y) plane. The rotation and the offset from zero are then extracted. Once the tracks have been corrected, the vertical alignment is performed.
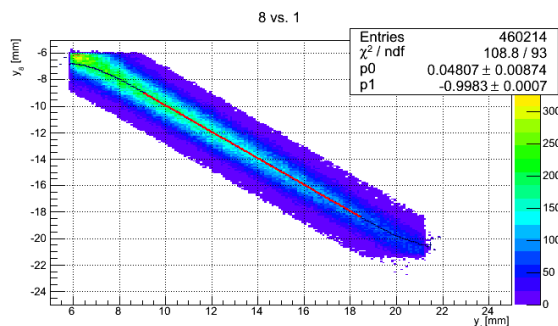

Figure 17: Correlation between vertical positions in opposite detectors
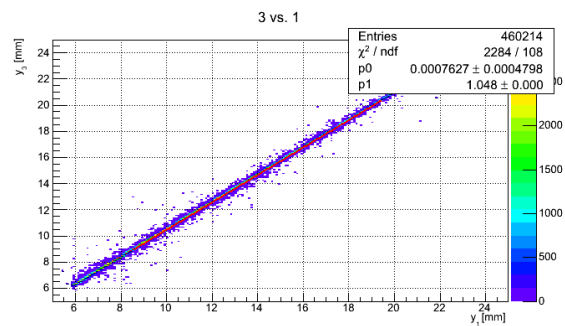
Figure 18: Correlation between vertical positions in detectors on the same side of IP1

The two back-to-back protons are then considered as a single track going through the four detectors constituting one elastic configuration, i.e. two upper (resp. lower) detectors on one side and two lower (resp. upper) detectors on the other side. As the vertical position in the detectors is, with a good approximation, proportional to the scattering angle, we can measure the ratio of these proportionality factors between all detector pairs. As shown in **Error! Reference source not found.** and **Error! Reference source not found.**, the rrelation plot between the reconstructed vertical positions in the different detectors is fitted to determine the slope. This slope is exactly the ratio needed to predict the position in all detectors using only one. This is used to perform the relative alignment between all detectors constituting an elastic arm. Each detector is used to infer the position in the others. The distribution of the difference between the reconstructed position and the prediction tells the offset between the two detectors considered (see Figure 19).

One station has to be taken as a reference for the alignment. The choice is driven by the precision of the distance measurement which differs from station to station due to statistics or simply by construction. The precision reached on the relative alignment is better than 5 microns. Concerning the absolute positioning with

respect to the beam, the offset is also calculated assuming the distributions to be symmetric. This measurement is not as accurate as the relative positioning due to statistics. An overall precision of 30 microns is achieved.

2.6 Physics analysis

In this section the principle of the physics analysis will be described. However, as the analysis is still on-going, the ATLAS publication policy does not allow to show any results.

The alignment was the first step of the entire chain. Once it was done, the topology of the elastic interactions can be used to distinguish signal from background and the kinematics can be calculated.
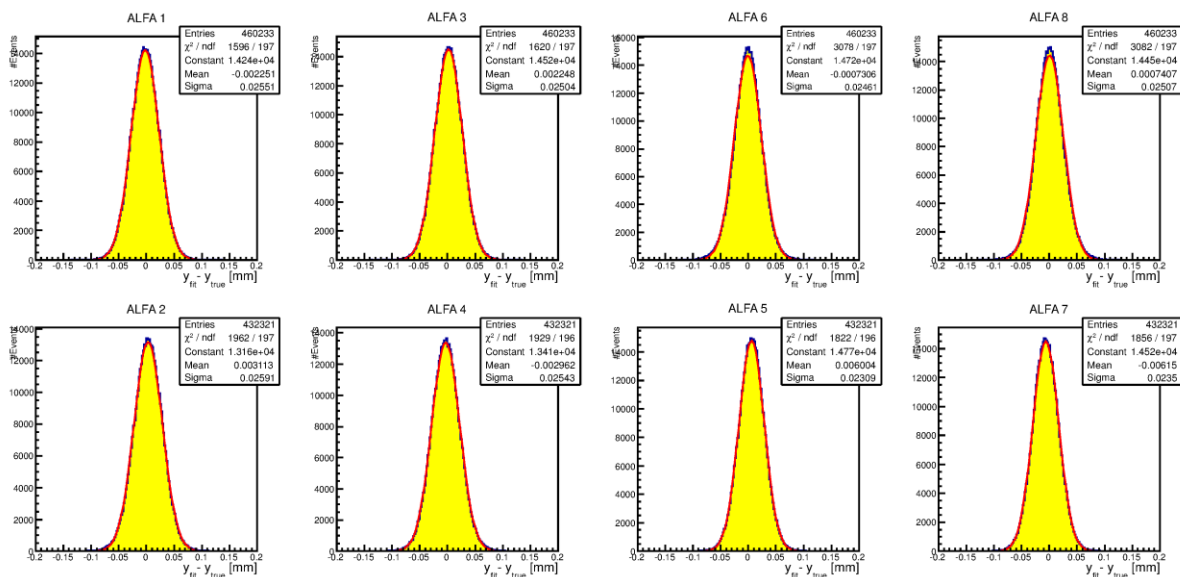

Figure 19: Residuals for all ALFA detectors after alignment. The remaining offsets are all smaller than 3 microns

In order to suppress the background, mainly composed of coincidences of halo particle, some cuts are applied to the data. These cuts rely on the event topology and are tuned on Monte Carlo simulation to keep more than 99% of the elastic events. Using only the selected events, the differential elastic cross section spectrum is calculated. However, in order to fit it and extract the nuclear slope and the total cross section, various corrections must be applied.

The first one is the acceptance correction. Not all particles scattered at the interaction point will reach the detector. Some of them, with small vertical scattering angle will go in between the upper and the lower detector. Others will be lost during the transport from the interaction point to the roman pots either by intra-beam scattering, beam gas scattering or simply by hitting the beam screen. The acceptance is calculated using a particle transport program called MadX.

The second one is the efficiency of the elastic events. A golden event is composed of four detectors in which a trigger signal has been detected and where the track was reconstructed. However in some cases, despite a trigger signal, no tracks where reconstructed. In that case, in order to evaluate the fraction of elastic events, some selection cuts have to be applied. The detectors providing a reconstructed position are used to decide if the event was elastic or background. Obviously, the lower the number of detectors with reconstructed tracks, the harder it is to discriminate signal from background. These losses are mainly related to hadronic showers

occurring in the inner station. This results in a large activity in the outer station which makes the reconstruction of the event impossible.

The overall efficiency of elastic reconstruction is around 90% and is independent of the scattering angle showing no physics dependence.

The last correction called unfolding is meant to account for all effects leading to a deformation of the initial physics distribution. Mainly due to divergence and detector resolution, the measured momentum transfer differs from the real one. The bias introduced by these effects as a function of the scattering angle has to be corrected. In the case of the ALFA detector, the momentum transfer can be measured using either the position or the angle measured between the two stations. The relatively small distance (4 m) separating the inner and outer detectors leads to a poor angular resolution. The unfolding corrections reflect this as they are about 1% for the position method and up to 40% for the local angle method.

Once all these corrections have been calculated, there is still one ingredient missing to measure the total cross section: the normalization factor, i.e. the integrated luminosity. The luminosity is measured using the central detector of ATLAS. Several sub-detectors are specifically designed for luminosity measurement whereas others deliver it just as a side product. In fact, every detection system which is able to count events whose rate varies linearly with the luminosity, they by definition consist in a luminosity monitor once calibrated. The very precise calibration method used at CERN is named Van Der Meer scan and provides a precision better than 2% in normal running. In the conditions needed for the ALFA measurement, due to a very low intensity, the precision is slightly worse, around 3%.

Up to now, due to a discrepancy between the various reconstruction methods, no results were published. This discrepancy has been attributed to a wrong description of the beam line. Indeed the differences observed indicate that the quadrupole strength and their longitudinal position are not nominal resulting in a wrong optics implying a bias reconstruction of the scattering angles. In collaboration with LHC experts, a strong effort has been put in place in order to improve the understanding of the beam optics. The combination of the ALFA constraints together with the optics measurements start to pay off and a suitable optics is expected to be available soon.

2.7 Conclusions and future

The knowledge of the ALFA detector developed during the characterization phase as allowed the ERs to participate actively in the installation, the commissioning and the operation of the ALFA detector. The detector oriented approach has been a great help in order to set the bases of the data analysis. Despite the very challenging environment in which the detectors are operated, the performance has been found to match the one demonstrated during various test beam campaigns.

Even though the physics analysis has encountered serious difficulties related to understanding of the LHC optics, the collaboration between the ALFA community and the accelerator experts points toward an imminent solution. The next step will be the publication of the proton-proton total cross section at a centre-of-mass energy of 7 TeV. The understanding of the optics and all the tools developed in this respect will ease the future analysis. In addition, all the software required to compute the necessary steps for the analysis has been developed and can be used at any energy or optics.

During the long shutdown, the LHC will be prepared for increased energy and luminosity. The ALFA detector will require a cooling system to be developed in order to cope with the temperature increase of the detector. The roman pot stations act as a resonant cavity with the dissipated radio frequency power heating up the detector posing a threat to its long term operation.

References

[1] P. Beltrame et al., The AX-PET demonstrator—Design, construction and characterization, Nuclear Instruments and Methods in Physics Research Section A, 10.1016/j.nima.2011.06.059

[2] E. Bolle et al., AX-PET: A novel PET concept with G-APD readout, Nuclear Instruments and Methods in Physics Research Section A695 (2012) 129–134, 10.1016/j.nima.2011.12.114

[3] ATLAS Forward Detectors for Measurement of Elastic Scattering and Luminosity, Technical Design Report, CERN/LHCC/2008-004.

Project Coordinator: Samo Korpar, JSI Ljubljana.

Ruben Verheyden, ESR, JSI Ljubljana. Supervisor: Samo Korpar.

INTRODUCTION

Photo-detectors in high energy particle physics experiments and related applications often have to operate in magnetic fields exceeding 1 T and are required to efficiently detect single photons. While the traditionally used photomultiplier tubes (PMTs) do not work in high magnetic fields, standard semiconductor light sensors (photo-diodes, avalanche photo-diodes (APDs)) are not sensitive to single photons. Novel photo-detectors were developed that allow efficient single photon detection while operated in a magnetic field: Geiger Mode Avalanche Photo-Diode (GM-APD), and Micro-Channel Plate Photomultiplier tube (MCP-PMT).

The aim of this project is to use these novel high magnetic field compatible photo-detectors and to investigate their application for multimodal medical imaging (e.g. MRI-PET) and particle identification. The sensors under study are Geiger mode APDs (also known as silicon photomultipliers, SiPMs) and micro-channel plate (MCP) PMTs with multi-anode read-out. Two main activities can be distinguished within the project: one concentrates on the characterization of SiPMs and aims to construct a depth of interaction (DOI) encoded PET module suitable for use in time-of-flight PET, while the other aims to construct a ring imaging Cherenkov (RICH) detector prototype using aerogel as radiator and MCP-PMTs or HAPDs for the detection of Cherenkov photons.

POSITRON EMISSION TOMOGRAPHY

The use of SiPMs as photon detectors in PET modules offers several advantages over conventional light sensors, including applications in a magnetic field, more compact design and easier operation [1]. SiPMs from different manufacturers were assessed in a characterization set-up, and a PET prototype apparatus [2], consisting of LYSO scintillation crystals coupled to a silicon photomultiplier array, was constructed and tested.

A special crystal array was designed to provide depth of interaction encoding based on the principle of light sharing over the channels of the SiPM module. Simulations were performed to understand the behavior of such a DOI-PET module, and to find suitable parameters to extract the depth of interaction information. Experiments with a test module were performed to verify the proof of concept.

SiPM Characterization

Single SiPMs were tested in a characterization set-up consisting of a pulsed picosecond laser (Pi-Las, 34 ps FWHM) to determine device properties including gain, geometrical efficiency, response linearity and timing resolution. Extensive tests have been performed with SiPM prototypes from STMicroelectronics with an active area size of 3.5×3.5 mm^2 and 4900 micro cells [3]. The SiPM characterization set-up was placed in a temperature controlled environment allowing characterization in the range of -20°C to 15°C.
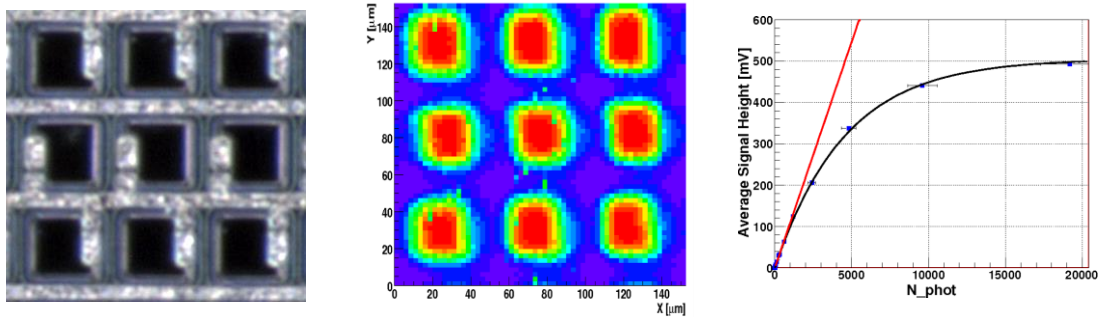
Figure 1: Comparison between a microscope picture (left) and a scan made with the PiLas laser (middle) for the STM SiPM prototype. Right plot depicts for the same sensor the typical non-linear
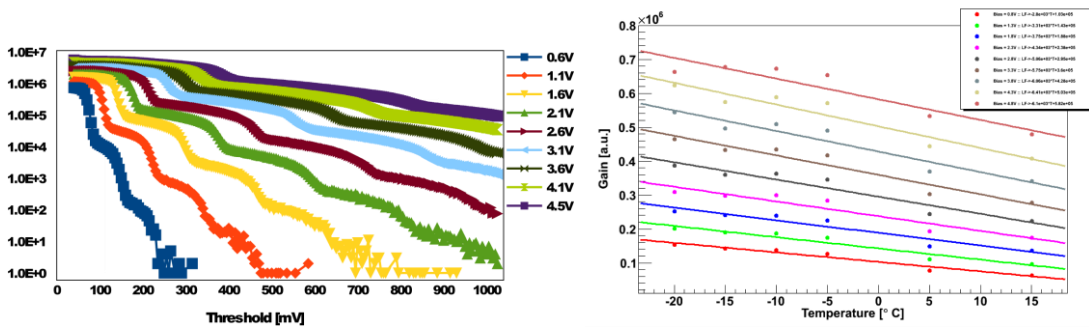

Figure 2: Dark count rates as a function of overvoltage (left). Temperature and applied overvoltage dependencies of the gain for the overvoltage from 0.8 V in light red to 4.8 V in dark red (right).

From the measurements at room temperature we have determined the surface sensitivity, and have investigated the dynamic range and dark count rates as a function of applied overvoltage, the difference between bias and breakdown voltage, $\Delta V = V_{Applied} - V_{Breakdown}$. The surface scans showed that the active area follows the internal structure of the SiPM which can be seen in Figure 1. The obtained geometrical efficiency of 33% agrees with the simple estimate of 36% (30 μm x 30 μm micro-cells at 50 μm pitch).

Figure 2(left) shows the dependence of the dark count rates for various overvoltages. It is clear that choosing an appropriate overvoltage is important to minimize the dark count rates. Applying a higher overvoltage will result in considerable higher dark count rates, which in turn will negatively impact the single photon timing resolution of the device.

The gain dependence on temperature and overvoltage was determined with the characterization setup placed in the temperature controlled environment. From Figure 2(right) we see that the gain of the device increases by applying a higher overvoltage as can be expected for SiPMs where the gain is given by $M = C \times \Delta V/e_0$, where C is the micro cell capacitance and e_0 the elementary charge. We also observe that the gain increases by lowering the temperature. This effect is due to the variation of the breakdown voltage with the temperature which results in the change of the overvoltage and gain.
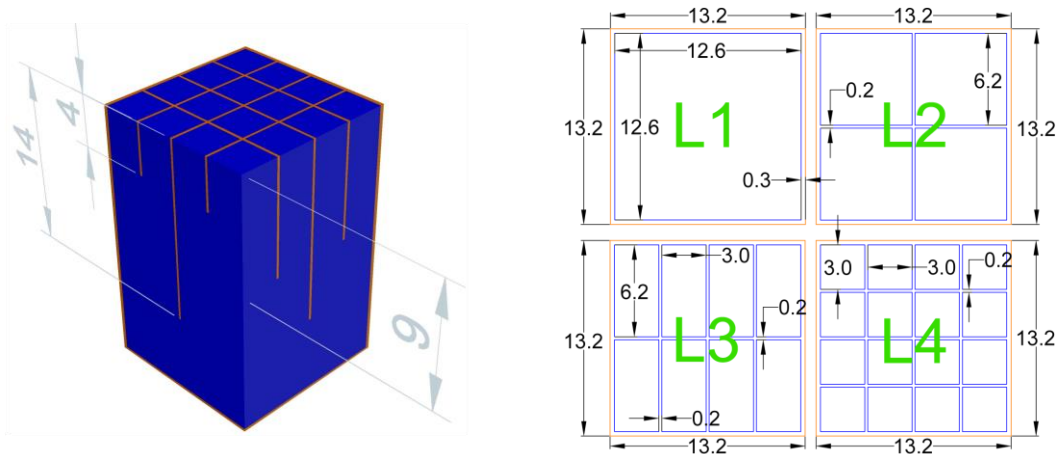
Figure 3: 3D model of the segmented crystal array (left), blue area represents LYSO crystal, while orange represents a white BaSO4 reflector. In this picture layer 1 is on the bottom, while layer 4 (SiPM side) is on the top. Schematic of the various layers of the segmented crystal array (right).

Basic TOF-PET performance

A single SiPM PET detector was assembled by coupling a LYSO crystal from Saint-Gobain (Prelude 420TM, $3 \times 3 \times 30$ mm^3) to a STMicroelectonics SiPM to determine its feasibility for use as a time-of-flight PET (TOF-PET) photo-detector module [4]. Energy and back-to-back coincidence timing resolution of this PET system were measured using the annihilation γ rays from a ^{22}Na source. The energy resolution of the PET system was shown to be correlated to the over-voltage applied to the SiPM and is in the range of 12.5% – 17% (FWHM). The back-to-back coincidence timing resolution was measured to be in the range of 330 ps – 400 ps (RMS). Obtaining an optimal timing resolution requires to work at single photo-electron signal heights. Because of the high dark noise rates of SiPM devices at the single photo-electron level (several 100 kHz per mm^2 of active SiPM area at room temperature), it is beneficial to lower the temperature of the device. At a temperature of -20°C it was possible to obtain a back-to-back timing resolution of about 330 ps (RMS).

DOI-PET module

A specially segmented crystal array was designed to provide a depth-of-interaction encoding. The dimensions of the crystal array were matched to the dimensions of a 4×4 channels array of SiPMs in a monolithic package (Hamamatsu MPPCs - multi pixel photon counter - model S11830-3344MT).

The crystal array consists of a monolithic block of a LYSO scintillation crystal which has several cuts with varying depths resulting in 4 layers with different segmentation. The cuts were made in such a way that the segmentation becomes finer along the depth of the crystal. Figure 3(left) shows a 3D model of the segmented crystal where layer 1 is on the bottom and layer 4 is on the top, where SiPMs are attached. A schematic of each layer is shown in Figure 3(right) with description of each layer below:

- L1: The first layer has no segmentation to allow light sharing over all the channels. It is also the layer closest to the source (i.e. furthest away from the SiPM). The thickness of this layer is 6 mm.
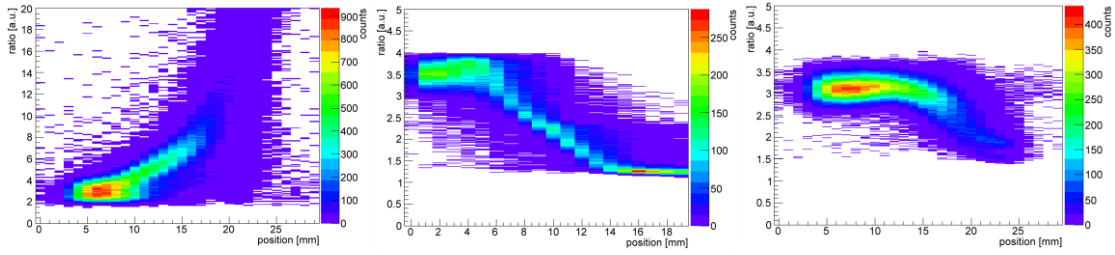
Figure 4: Experimental verification of the rough ratio showing the presence of the rough ratio structure as calculated (left). Simulation result of alternative ratio comparing the maximum quadrant signal with the maximum channel (middle). Experimental verification of the Qmax/CHmax ratio (right).

Layer	Q_{max}	Q_{min}	SQ_{max}	SQ_{min}	CH_{max}	CH_{min}	$\dfrac{Q_{max}}{Q_{min}}$	$\dfrac{SQ_{max}}{SQ_{min}}$	$\dfrac{CH_{max}}{CH_{min}}$
1	$\dfrac{1}{4}$	$\dfrac{1}{4}$	$\dfrac{1}{8}$	$\dfrac{1}{8}$	$\dfrac{1}{16}$	$\dfrac{1}{16}$	1	1	1
2	$\dfrac{5}{8}$	$\dfrac{1}{8}$	$\dfrac{5}{16}$	$\dfrac{1}{16}$	$\dfrac{5}{32}$	$\dfrac{1}{32}$	5	5	5
3	$\dfrac{10}{16}$	$\dfrac{2}{16}$	$\dfrac{9}{16}$	$\dfrac{1}{16}$	$\dfrac{9}{32}$	$\dfrac{1}{32}$	5	9	9
4	$\dfrac{20}{32}$	$\dfrac{4}{32}$	$\dfrac{18}{32}$	$\dfrac{2}{32}$	$\dfrac{17}{32}$	$\dfrac{1}{32}$	5	9	17

- L2: The second layer has a 2×2 segmentation by making 2 perpendicular cuts starting at layer 4 up to a depth of 14 mm. The thickness of this layer is 5 mm and it consists of 4 quadrants (Q).
- L3: The third layer has a 2×4 segmentation by making 2 additional, but parallel cuts. Location of the cuts is in the middle of the layer 2 segmentations. Again the cuts start at layer 4 and are 9 mm deep. The thickness of this layer is 5 mm and consists of 8 sub quadrants (SQ).
- L4: The fourth and final layer has a 4×4 segmentation by making 2 additional, but parallel cuts that are perpendicular to the additional cuts for layer 3. The location of the cuts is such that the result is 16 equal sized segments called channels (CH). The final cuts are 4 mm deep resulting in a thickness of 4 mm. This layer is coupled directly to the SiPM array.

The principle behind the DOI encoding is the difference in light sharing between the 16 SiPM channels depending on the layer in which the scintillation originated. By calculating ratios of signals between the various quadrants (L2 segments, Q), sub quadrants (L3 segments, SQ) and channels (L4 segments, CH) one can roughly estimate at what depth the interaction happened in the crystal.

In Table 1, the rough ratios are listed which are calculated by assuming uniform light distribution of reflected scintillation photons, and a perfect containment of direct photons within the layer dependent crystal segment. These rough ratios show that we can easily distinguish in which layer the interaction occurred based on the CH_{max}/CH_{min} ratio. Experimental verification of this rough ratio was obtained by using a PET trigger consisting of a single LYSO crystal coupled to a single SiPM and scanning the segmented crystal from the side using a 22Na
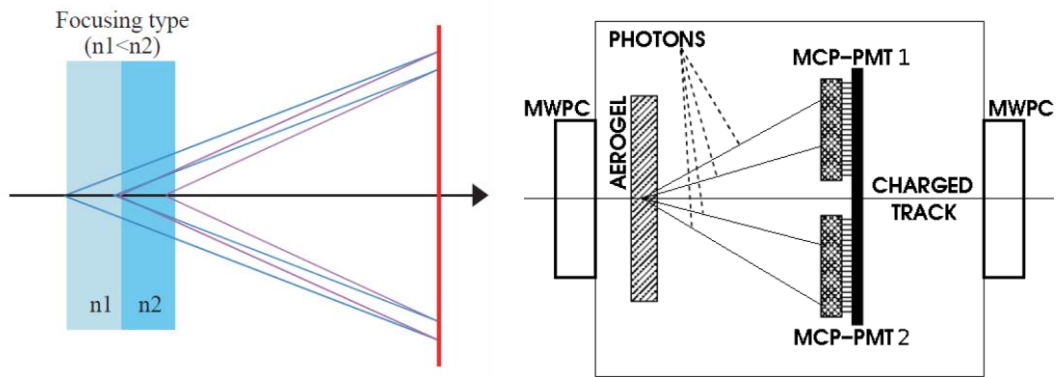
Figure 6: Schematic of the working principle of the proximity focussing Aerogel Ring Imaging Cherenkov counter (left). Setup used for the beam tests at KEK (right).

source. The result can be seen in Figure 4(a) and it is clear that the rough ratio structure is present. The broadening of the ratio versus depth is attributed to a combination of light sharing not being uniformly distributed, and to the particular acceptance angle of the PET trigger.

To assess the impact of DOI encoding, MC simulations using GEANT4 [5] were performed using a full ring constructed of the segmented crystals as shown in Fig. 3, and a full ring constructed of an array of simple crystals with no light sharing between channels. Reconstruction was performed by constructing a sinogram using the mean position and correcting it for the depth of interaction by using the Qmax/CHmax ratio in the case of the segmented crystal. For the basic crystal array the sinogram was calculated by using the center of the maximum channel. The sinograms were then passed to the STIR reconstruction software [6] to perform a filtered 2D back projection. A 1D projection was made of the obtained 2D reconstructed graphs to assess the position resolution. The position of the source in the simulation was moved in steps of 3 mm along the distance from the center (at X=0 mm) towards the edge of the field of view at around 69 mm.

The results for an extreme off-axis source location are compared in Figure 5 to illustrate the benefit of the newly designed segmented crystal array (Fig. 5, left) and the basic crystal array (Fig. 5, middle). Figure 5(right) contains the results for all the locations. The DOI reconstruction shows a stable resolution with a negligible bias.

PROXIMITY FOCUSSING RICH

The proximity focusing RICH counter prototype [7,8,9] utilizes a Cherenkov radiator consisting of two layers of silica aerogel with different refractive indices, the higher being downstream. Such an arrangement results in a focusing effect of the Cherenkov rings originating in each layer, as illustrated in Figure 6(left), and improves the angular resolution. An array of multi-anode MCP-PMTs is used as photo-detector and is placed after a short expansion gap of 20 cm from the radiator entrance surface.

Micro-Channel Plate Photomultiplier Tube

A multi-anode MCP PMT with 10 μm diameter pores developed by Photonis was investigated as a detector of single photons. The sensor was shown to perform well in the magnetic field up to 1.5 T. To evaluate its long-term stability in particle physics experiments, its performance was studied as a function of the charge,
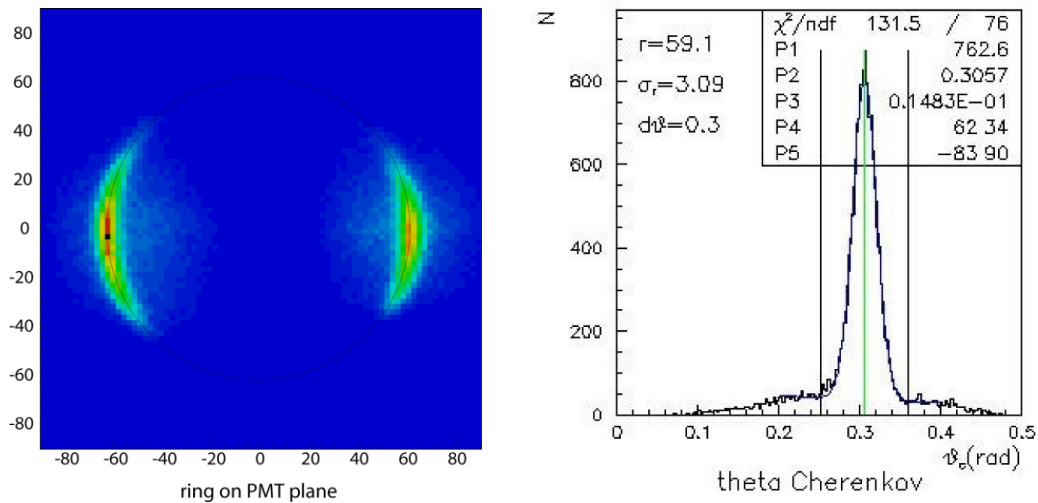
Figure 7: Cherenkov ring on the MCP-PMT plane (left), distribution of detected photons over the Cherenkov angle (right).

accumulated on the anode. During the test, the MCP-PMT was illuminated with a blue LED so that the single photon rate on each channel was around 1 MHz. A decrease of about 10% in quantum efficiency was observed after a total accumulated charge of 400 mC/cm^2.

Beamtest at KEK

Preliminary tests of the RICH prototype were carried out in November 2009 using a 2 GeV/c electron test beam at KEK in Tsukuba (Japan). The RICH counter consisted of an aerogel radiator and two Photonis multi-anode MCP-PMTs covering about 30% of the Cherenkov ring, as shown in Figure 6(right). Multi-wire proportional chambers were placed in front and behind the RICH counter to provide particle tracking information. The measured Cherenkov angle resolution (Figure 7) and the number of detected photons show that a pion/kaon separation at a 4 sigma level is possible at the particle momentum of 4 GeV/c.

References

[1]   D. Renker, E. Lorenz, Advances in Solid State Photon Detectors, JINST 4 P04004 (2009) 48.

[2]   H. Chagani et al., "Tests of silicon photomultiplier PET modules", Nuclear Science Symposium Conference Record (NSS/MIC), 2009 IEEE. 2009, pp. 1518-1520

[3]   R. Verheyden et al., "Performance study of silicon photomultipliers as photon detectors for PET", Nucl. Instrum. Meth. A628.1 (2011), pp. 381-384.

[4]   R. Verheyden et al., "Performance study of Silicon Photomultipliers as photon detectors for PET", Nuclear Science Symposium Conference Record (NSS/MIC), 2010 IEEE. 2010, pp.1494-1497.

[5]   J. Allison et al., "Geant4-a simulation toolkit", Nucl. Instrum. Meth. A506.3 (2003), pp. 250-303.

[6]   Kris Thielemans et al 2012 Phys. Med. Biol. 57 867

[7]   S. Korpar et al., "Aerogel RICH for Belle II", PoS ICHEP2010 (2010), p. 506

[8]   K. Hara et al., "Studies of a proximity focusing RICH with aerogel radiator for Belle II experiment", Nuclear Science Symposium Conference Record (NSS/MIC), 2010 IEEE. 2010, pp. 415-419

[9]   I. Adachi et al., "Study of a 144 channel multi-anode hybrid avalanche photo-detector for the Belle II RICH counter", Nucl. Instrum. Meth. A639 (2011), pp. 103-106

Project Coordinator: Els Koffeman, Nikhef

Francesco Zappon, ESR, Nikhef. Supervisor: Martin Van Beuzekom

INTRODUCTION

The importance of a pixel readout has been increasing constantly in the past years and today pixel detectors are widely used in the most important experiments in High Energy Physics [1], but have also found applications in many other fields [2]. The work presented here has been developed in the framework of pixel chip design for applications in Micro Pattern Gas Detectors (MPGD) and, specifically, for GridPix detectors.

1. GRIDPIX

A GridPix detector can be seen as a very small version of a Time Projection Chamber (TPC). In Figure 1 it is shown a diagram of this kind of detector: on top of a pixel readout chip an amplification Grid is built using MEMS technology. The chip-grid distance is about 50 μm and the holes in the grid are aligned with the pads of the pixel chip. On top of the Grid, at a distance that can vary from 1 mm to 2 cm, an electrode is placed and the entire volume is filled with gas. When a particle goes through the detector it ionizes the gas: the primary electrons created in the ionization process then drift towards the Grid by means of an applied electric field. When the electrons reach the Grid they enter in an area of very strong electric field: in here a multiplication process takes place, which creates an avalanche amplifying, the signal from the primary electrons in order to make it detectable by the frontend electronics.
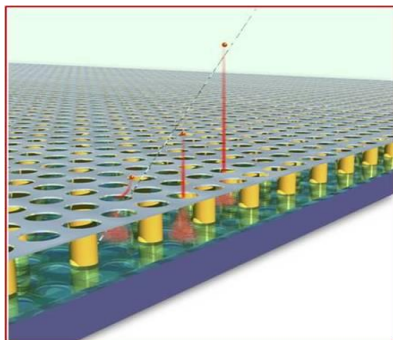

Figure 1: schematic representation of a GridPix detector. The particle passing through the drift volume ionizes the gas. The produced electrons are drifted toward the anode. When they reach the amplification region, a multiplication process takes place. The amplified charge is then detected by the readout chip.

Once the signal is detected, the pixel readout gives information on the X-Y position of the primary electrons, while measuring the time it takes for the charges to drift from the production point to the readout chip gives information on the Z coordinate. With this information is then possible to have a 3D reconstruction of the particle's track. Currently, the TimePix chip [3] is used as the readout chip for GridPix detectors. However, this chip has some limitations: in particular, as it is possible to see in Figure 2, if the drift volume is small (~ 1 mm) the number of electrons per track is low. Given that the resolution if TimePix is 10 ns it is not possible to discriminate the time of arrival of all the electrons and it is therefore not possible to perform a good track fit. To overcome this problem, hence, a better resolution is needed to perform the time measurement.
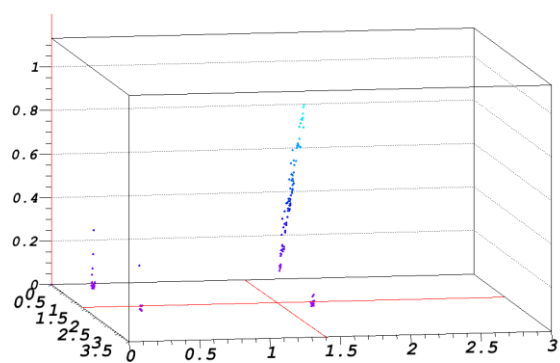

Figure 2: the same event as recorded in 4 different GridPix detectors. The top-right detector has a drift volume of 1 cm, while the other 3 detectors have only 1 mm (electrons that appear to be produced outside the drift volume are affected by timewalk). The unit for all the axis is cm.

2. HIGH RESOLUTION TIME MEASUREMENTS – TIME TO DIGITAL CONVERTER (TDC)

The main focus of this work is on how to design and implement a pixel chip to provide reliable high resolution time measurements. Many different approaches are possible to achieve a wide range of resolutions, but in the present case there are some hard constraints which must be taken into account. First of all, the limited area available since the pixel size is fixed to be 55x55 µm. Second, the power consumption must be kept to a minimum. Given these constraints the approach that was decided to adopt foresees the use of an oscillator to generate, for a short period of 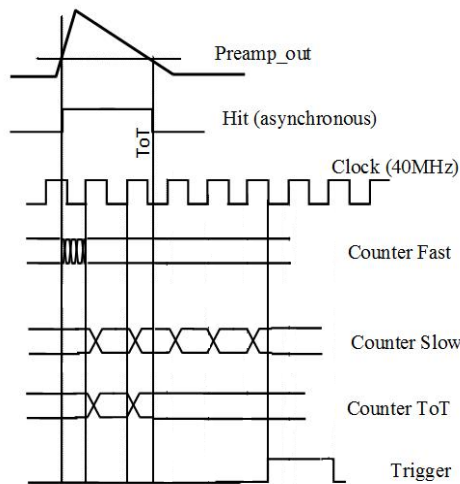time, a high frequency clock (Fast Clock). When the signal coming from the amplified primary electrons goes over threshold the oscillator is started and it is then stopped at the first rising edge of the slower System Clock as shown in Figure 3 (in the current applications, this clock runs at 40 MHz to match the LHC bunch crossing rate).

At this point, another counter (Slow Counter) starts counting the System Clocks until an external synchronous Trigger (common stop) arrives. The combination of the time information of the two counters gives the Time of Arrival (ToA) of the ionizing particle. It is straightforward, in this counting scheme, to add another counter that records the time spent by the signal over threshold (Time over Threshold - ToT - Counter). This gives information on the energy of the avalanche that generated the signal and can be used to correct the ToA for other effects like timewalk [10].

Figure 3: timing diagram that illustrates the implemented TDC solution.

3. GOSSIPO-3

GOSSIPO-3 [5] is a prototype chip developed in collaboration between Nikhef and Bonn University for the readout of gas detectors such as large Time Projection Chamber (TPC) or MPGD as GOSSIP. The chip has been proposed in 2008 as next iteration of GOSSIPO-2 [4], a pixel chip with a 16x16 pixel matrix designed to test mainly the functionality of the fast oscillator and to characterize the mismatch due to process variations. The most important circuits to test in GOSSIPO-3 were the local oscillator, the analog frontend, the on-pixel digital logic and two different types of Low Drop Out regulators. The prototype contains only two pixels: one equipped with the complete analog and digital chain (called Analog Pixel) and the other which has only the digital part (called Digital Pixel). The focus of this project has been on the physical implementation and testing of the pixel functionality.

3.1: Single pixel block diagram

In Figure 4 the block diagram of the pixel in GOSSIPO-3 is shown. The important things to notice are the presence of an oscillator in every pixel an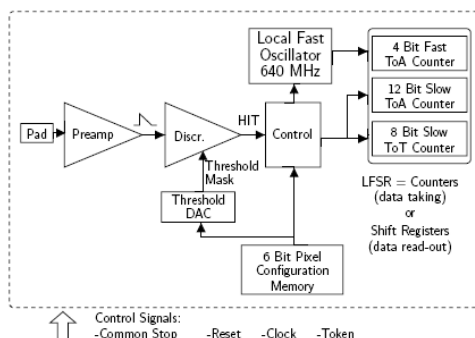d the Moore State Machine that controls the digital logic. The diagram also shows the various signals that need to be provided to control the pixel (Reset, Trigger, Token) in the data taking and in the readout phase. The counters implemented are Linear Feedback Shift Registers (LFSR), in order to minimize the area, since this type of counter can be used to shift out the data without the need of an additional shift register.

Figure 4: GOSSIPO-3 single pixel block diagram.

The oscillator used in GOSSIPO-3 consists of a NAND gate with a chain of inverters in the feedback loop. The delay introduced by the inverters chain determines the oscillation frequency and is affected by changes in temperature and supply voltage (see Figure 5).
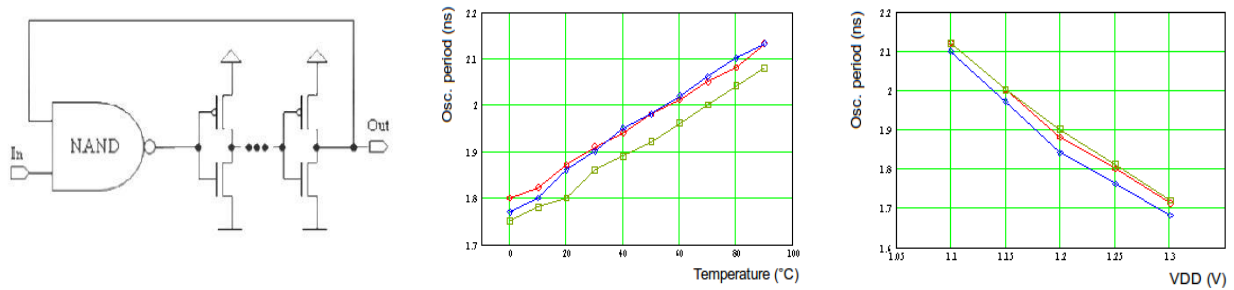

Figure 5: on the left it is shown a simplified schematic of the oscillator. In the centre is shown the temperature effect on the oscillation period while on the right the effect of a supply voltage variation.

3.2: Test results

To test GOSSIPO-3 it has been decided to use the S3 MultiIO board developed in Bonn [7]. The board is equipped with a Xilinx Spartan3 FPGA which can be controlled using the USB port present on the board itself (see Figure 6). The Data Acquisition software (DAQ) has been programmed in C++ using the Qt libraries to develop the GUI [8], while the FPGA firmware has been developed in Verilog using Xilinx ISE [11].
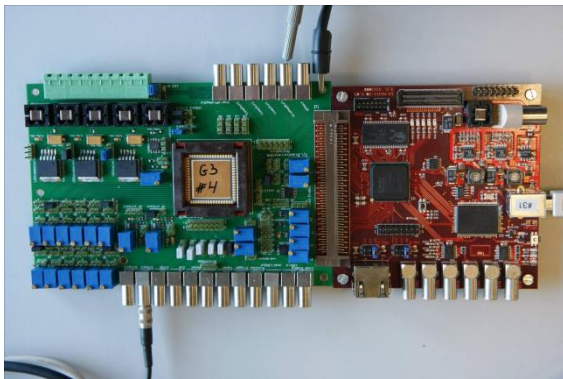

Figure 6: picture of the S3 MultiIO board (right, red color) and the board that hosts the GOSSIPO-3 chip (on the left, green). Notice the USB connector on the right side of the S3 board.

The main test that has been performed to completely characterize the TDC consists of injecting a pulse with different delay while keeping the time of arrival of the Trigger constant and recording the measured time. An example of such a test is shown in Figure 7.

The first step to extract the needed parameters from the data is to analyze the transition region between two consecutive bins of the TDC. To do so, the Error Function has been used to perform a fit which returns two parameters: the value on the x-axis where the function is at 50% (the red dot in Figure 8), which is the start/end point of the bin, and the sigma of the Gaussian (NB: the error function is defined as the integral of the Gaussian and it is assumed that all the noise sources that contribute to jitter have a Gaussian distribution).
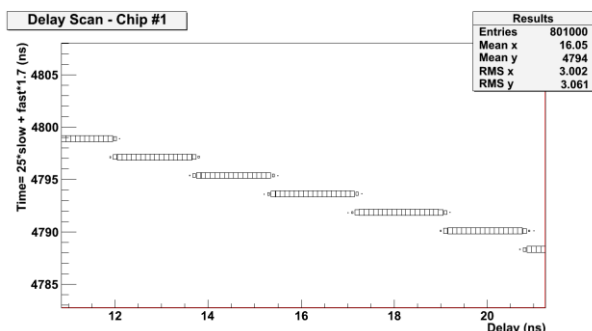

Figure 7: example of the outcome of a delay scan test performed with GOSSIPO-3. The time is decreasing as the test pulse is delayed toward the Trigger.

Once these two parameters have been extracted, it is possible to determine the Differential Non Linearity of the converter: the DNL is the relative difference between two consecutive bins of the TDC with respect to the ideal bin size. In Table 1 as an example the results for the Analog and Digital pixel of Chip 1 are

shown.

Chip	Bin size (ns)	Error	Jitter (ns)	Error	DNL
1 Digital	1.75	0.32	0.052	0.006	19.9%
1 Analog	1.77	0.21	0.09	0.01	31.8% (19.9%)

Table 1: Example of the relevant quantities measured for Chip 1. The number in parenthesis for DNL of the Analog pixel is calculated without taking into account bin 7 and 8 of the TDC.

Notice how the DNL of the TDC is quite high for the analog pixel. This is mainly due to two bins that depart more than the others from the ideal bin size (bin 7 and 8). It is understood that this behaviour is due to the presence of the falling edge of the system clock; in fact, tests performed with a 20 MHz clock show that the effect disappears. However, this result could not be reproduced by simulations.
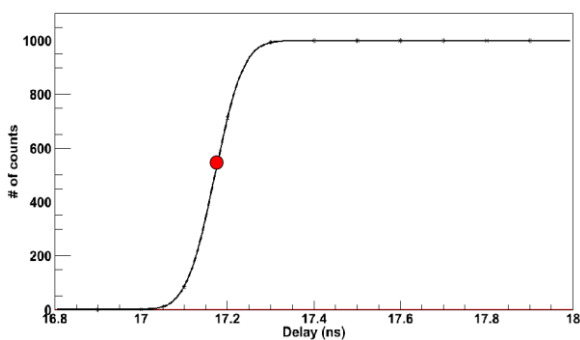

Figure 8: example of the fit performed in the transition region between two bins of the TDC. The red dot represents one of the parameters returned by the fit: the value on the x-axis where the function is at 50%.

4 GOSSIPO-4

To address the problems seen in GOSSIPO-3 a new prototype chip called GOSSIPO-4 [6] has been designed in the framework of TimePix-3 chip, a full-matrix chip that is the successor of TimePix. In particular, in GOSSIPO-4 the concept of Super Pixel, a 8-pixel structure with a common oscillator, has been introduced. This new implementation has been developed to reduce power consumption and area. Directly related to this new structure is the design of a Synchronization Logic which is present in every pixel and the use of a high density library for the digital design developed at CERN. The chip has been designed during 2012 and it is expected to be tested at the end of the same year.

4.1 GOSSIPO-4 super pixel and Synchronization Logic

A block diagram of the super pixel structure implemented in GOSSIPO-4 can be seen in Figure 9. The main difference with respect to GOSSIPO-3 is that the fast clock provided by the oscillator is now shared among 8 different pixels, instead of being local to the single pixel. The main drawback associated with this solution, which saves space and power, is given by the intrinsic asynchronous nature of the hit signal arriving at the pixel; if two pixels are hit during the same system clock cycle, in fact, the first one starts the oscillator while the second one has to hook up with the already running clock. Since what needs to be counted is the number of fast clock cycles, it is important to make sure that the distributed clock is glitch-free so that every flip flop in the fast counter see a clean signal and does not enter in a wrong counting state. To solve this problem a block

called Synchronization Logic, a fully asynchronous state machine, has been designed and implemented in every pixel. This block produces two signals: from the asynchronous hit and the system clock it generates a Gate which is used to start the oscillator (if not already started); from the Gate and the fast clock it generates a glitch-free Gated Fast Clock that is then supplied to the Fast Counter.
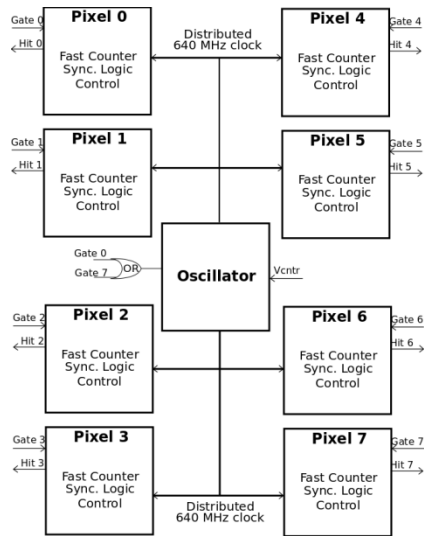

Figure 9: block diagram of the Super Pixel. The Oscillator is shared among 8 pixels.

4.2: GOSSIPO-4 oscillator

In GOSSIPO-4 the oscillator has been changed with respect to the one used in GOSSIPO-3. As explained, variations in the bin size were caused by crosstalk effect with the system clock. Another contribution of the measured mismatch in oscillation frequency between different chips has been identified with variation in supply voltage provided to the inverters in the oscillator. To correct for this effect and to make the oscillator more robust, a new approach has been adopted. As Figure 10 shows, the chain of inverters has been replaced with an alternation of RC stages and inverters. The former provide the required oscillation period, while the inverters act as buffers. The main characteristic of the capacitors used in this circuit is that they are not normal, but voltage controlled capacitor (varactor): the value of the capacitance is controlled by the provided voltage. In this way, it is possible to decouple the supply voltage from the control voltage (Vcntr) provided to the capacitances. Vcntr is generated by a PLL placed in the periphery of the chip that contains a replica of the oscillator. The constant feedback from the PLL to the single oscillators, then, ensures that the latter are kept at the same frequency. Another advantage of this configuration can be seen in Figure 11. For supply voltages > 1.2 V, the oscillation period is constant, as the characteristic curve reaches a plateau.
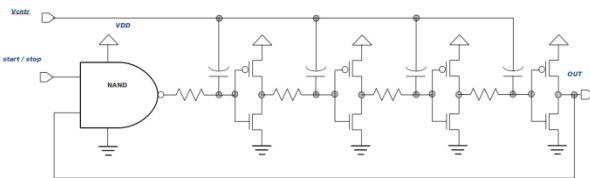

Figure 10: schematic of the oscillator used in GOSSIPO-4. The delay is introduced by the RC circuits, while the inverters act as buffer stages.
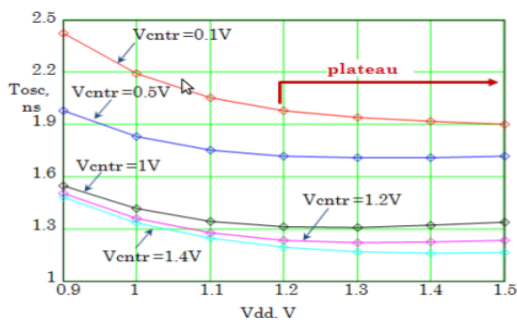

Figure 11: oscillation period as a function of the supply voltage (VDD) for different values of Vcntr. Notice the plateau that is reached when VDD>1.2 V.

4.2: GOSSIPO-4 pixel

As mentioned before, in every pixel a Synchronization Logic block is present. Besides it, there are other blocks as can be seen in Figure 12. At the input, to test the full functionality of the pixel, a multiplexer (MUX) is placed. The MUX allow us to select between 4 different input pulses, which are generated externally. The control logic is a Moore State Machine which controls the operation of the counters. The three counters are, as in GOSSIPO-3, LFSR. In this implementation, however, there is a difference: usually, a LFSR has 2^n-1 available states, because one state (the all-zero state, in the GOSSIPO-3 case) is forbidden; if the counter was to enter in this state, it would stay in the forbidden state for an indefinite time. In GOSSIPO-4, thanks to a NOR gate in the feedback chain, it is possible to obtain a full length counter with 2^n states available for counting [9].
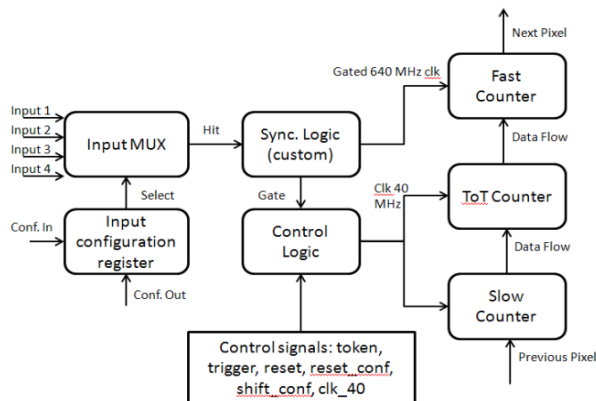

Figure 120: block diagram of the single pixel implemented in GOSSIPO-4.

CHAPTER 5: CONCLUSION

In the framework of Project 9 of the MC-PAD ITN the physical implementation and the testing of GOSSIPO-3 have been carried out successfully. The chip behaviour has been understood and characterized; some problems in the characteristics of the TDC and the new TimePix3 chip have naturally led to the design of a new prototype chip called GOSSIPO-4, to test a series of new circuits and a new high density standard cell library. The first submission of GOSSIPO-4 in 2011 was not successful due to a problem in a standard cell that was not detected during the design phase. A revised version of the chip has been submitted in 2012 and will be fully tested by the end of the year.

References

[1] L. Rossi, P. Fischer, T. Rohe, N. Wermes, *Pixel Detectors: from fundamentals to applications,* ISBN 978-3-540-28333-1

[2] Michael Campbell, on behalf of all members of the Medipix2 Collaboration, *10 years of the Medipix2 Collaboration* Nucl. Instrum. Meth. A Pages S1-S10

[3] X. Llopart et al. 2007 *Timepix, a 65k programmable pixel readout chip for arrival time, energy and/or photon counting measurements*, Nucl. Instrum. Meth. A 581 485

[4] V. Gromov, R. Kluit, H. Van der, *GraafDevelopment of a small-scale prototype of the GOSSIP chip in the 0.13um CMOS technology,* proceedings of TWEPP-07

[5] A. Kruth, C. Brezina, S. Celik, V. Gromov, R. Kluit, F. Zappon, K. Desch, H. Van der Graaf, *GOSSIPO-3: measurements on the prototype of a read-out pixel chip for Micro-Pattern Gaseous Detectors,* proceedings of TWEPP-10, JINST 5 C12005

[6] F. Zappon, M. Van Beuzekom, V. Gromov, R. Kluit, X. Fang, A. Kruth, 2012 *JINST* **7** C01081 *GOSSIPO-4: an array of high resolution TDCs with a PLL control*

[7] http://icwiki.physik.uni-bonn.de/twiki/bin/view/Systems/S3MultiIOSystem

[8] http://qt.digia.com/

[9] http://asicdigitaldesign.wordpress.com/2008/02/15/de-bruijn-and-maximum-length-lfsr-sequences/

[10] M. Fransen, *GridPix: TPC development on the right track,* PhD thesis, University of Amsterdam, 2012

[11] www.xilinx.com

PROJECT 10: MONOLITHIC DETECTORS

Project Coordinators: Marek Idzik, AGH-UST

Mohammed Imran Ahmed, ESR, IFJ-PAN and AGH-UST, Supervisors Michal Turala and Marek Idzik.

INTRODUCTION

In particle physics silicon, strips and pixels detectors are used to detect trajectory of particles with high precision to help in identifying primary and secondary vertices of short living particles. These detectors are located close to the collision point with high granularity to capture huge number of ionizing particles passing through the detector. Pixel detectors that are used now are of a hybrid type: a detector and readout electronics are realized in separate silicon wafers interconnected with bump bonding. They are thick detectors which preclude their use in experiments where multiple scattering effect must be minimized.

Silicon-on-insulator (SOI) technology offers a possibility to develop high precession, high granularity and thin monolithic pixel detectors. The additional feature of this technology is good radiation hardness [1]. SOI bonded wafers, the bottom layer is high-resistivity Si and works as a radiation detector, and CMOS circuits are implemented in the top low-resistivity Si layer, with both layers being separated by an oxide deposition, see Figure 1. With this technology complex CMOS circuits can be implemented in each pixel, so that intelligent data handling becomes possible. The technology has the advantages of latch-up free results in high temperature operation, smaller parasitic capacitances results in low power and high speed and low cost as compared to bulk CMOS process.
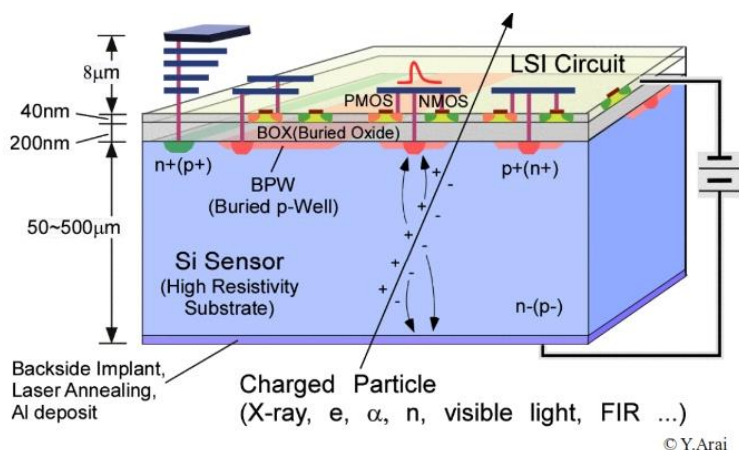

Figure 1: Cross-sectional view of SOI pixel detector.

The monolithic CMOS SOI pixel detector is developed for use in the Belle II experiment at S-KEKB collider and for future applications at ILC or LHC. Such detector is photo-sensitive and can also be used for imaging in outer space experiments and medical applications. The presence of back gate effect which causes a shift in transistor threshold, limits the application of large bias voltage making the detector only partially depleted. This effect can be mitigated by implanting lightly doped buried p-type well (BPW) just below the BOX layer, see Figure 1. A study performed using technology computer-aided design (TCAD) simulation confirm the functionality of the applied technique [2].

1 SOI PIXEL DETECTORS AND DESIGN PROTOTYPES

The fabrication of SOI pixel detectors was carried out at Lapis (previously named OKI) semiconductor using the 0.2μm CMOS fully-depleted SOI process. Some of the novel concepts exploring SOI technology are pursued at

KEK which includes Integration type pixel (INPTIX), Dual mode integration type pixel (DIPIX) and Counting type pixel (CNTPIX) detectors [3]. Prototyping is done by means of Multi project wafers (MPW) that are submitted to production twice a year. R&D is pursued within the SOIPIX collaboration. This report mainly concentrate on INTPIX and DIPIX detectors.

1.1 SOI pixel detectors

INTPIX3 is a signal integration type pixel detector designed to study remedies to back-gate effect observed in previous prototypes (INTPIX2) [4]. Eight different layouts are included in INTPIX3 chip to evaluate the back-gate effect and its suppression. The layouts differ by the presence of the BPW, its area and shape of the p+ implant. Each pixel size is 20x20 μm^2, size of each layout is (64x32) pixels and total number of pixels on the chip is 16384 (64x32x8). DIPIX resembles INTPIX with some additional features. Its circuit is designed to work both in n-type and p-type substrate, had an internal 10-bit Wilkinson type ADC and correlated double sampling (CDS) circuit in each pixel. Table 1 shown the summary of integration type pixel detector, which is designed and measured.

Detector	Pixel Size[um]	No. of Pixels	Effective Area [mm]	Chip area[mm]	Fabrication year	No. of pixel type	CDS in pixel
INTPIX3A	20x20	128x128	2.56x2.56	5x5	FY08	8	No
INTPIX3B	20x20	128x128	2.56x2.56	5x5	FY09-1	8	No
DIPIX1	14x14	256x256	3.58x3.58	5x5	FY10-1	1	Yes
DIPIX2 (CZ-n,FZ-n)	14x14	256x256	3.58X3.58	5x5	FY10-1	2	Yes

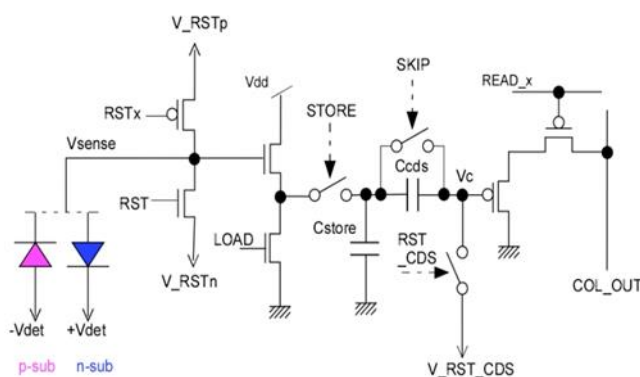**Table 4 Summary of integration-type pixel detectors**

Figure 2: Schematics of DIPIX1/2 single pixel readout

1.2 Design prototype

In Figure 2 the schematic of DIPIX1/2 single pixel circuit is shown. INPTIX3 schematic is similar to DIPIX1/2 with the exception of CDS part and it is design to work only with n-type substrate. The working principle of the circuit in Figure 2 is describe in this paper [5].

2 MEASUREMENT AND TEST RESULTS

The monolithic SOI pixel detectors shown in Table 1 are designed and found to be functional. The characterization of these detector is done using infrared laser and radiation sources. All the measurement shows in this chapter are done at room temperature i.e. 24^0C. In the following some example measurements and results are shown. The complete description may be found in [5,6,8].

2.1 Stability Test

In principle each pixel should be reset after every frame and if there is no signal in the sensor the pixel output should be constant. The stability test is done to check whether the detector is capable of operating in long run measurements. The pixels responses are analyzed in dark without any signal. The behavior of INTPIX3 and DIPIX1 detectors are studied as a function of time. The outputs of ADC conversion (average of 10 frames) for two different pixels are plotted over time in Figure 3. The measurement is taken continuously for 1 hour. Systematic changes during first 20,000 frames in DIPIX1 sensor are due to self heating and probably may be reduced in future using the CDS. In contrast to DIPIX1 results, INTPIX3 raw ADC values are adding up frame by frame till reaching saturation.
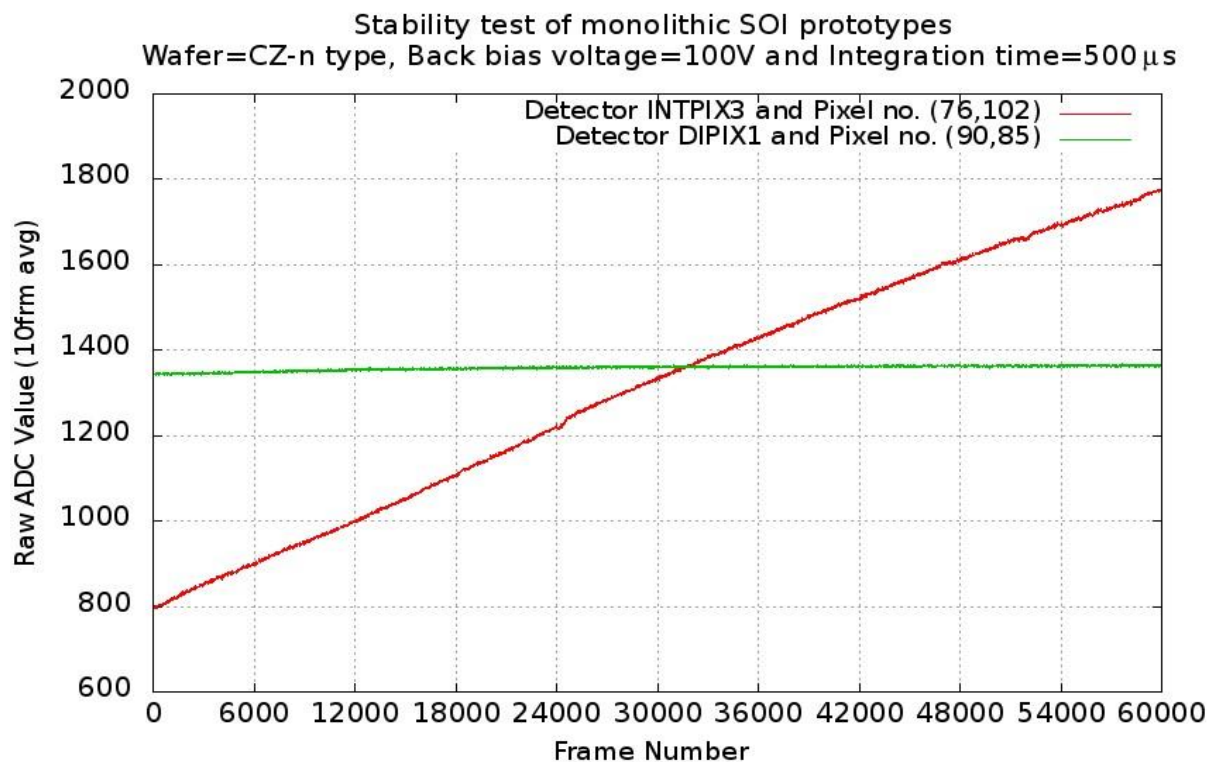

Figure 21: Stability test of SOI detectors by skipping CDS with 60,000 frames for single pixel. (the horizontal scale corresponds to 1 hour data taking)

2.2 Laser Measurements

The response of SOI detector has been tested with infrared (IR) laser (PDL 800-D) in pulse mode with 80 MHz frequency and 1060 nm of wavelength. The 3-Dimensional motorized setup (see Figure 4) is used to focus the Schfter+Kirchhoff laser optic "60fc-4-all-02-pq" to a spot size of ~10µm. (Spot size is calculated using INTPIX3 by focusing the laser at a focal distance).

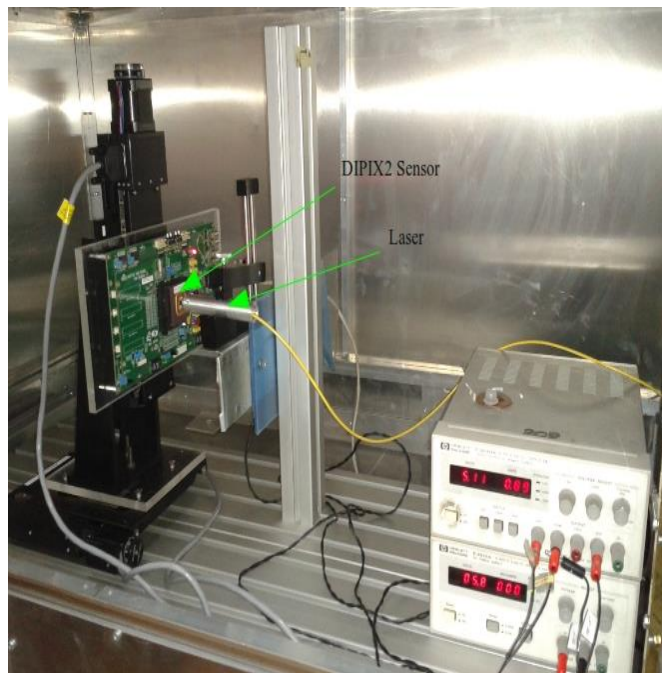Since the spot is smaller than the pixel pitch (see Table 1), the measured signal can be seen mainly in a single pixel. In DIPIX2, we observed a halo effect for very large group of pixels around the illuminated pixel. The amplitudes of these pixels are around 12 to 15% of the pixel with maximum amplitude and their distribution is beyond the Gaussian. The halo is seen in both sensors of DIPIX2 and it mostly depends on laser intensity. Figure 5 and 6 show the result before and after optimizing the laser intensity and back bias voltage for DIPIX2 FZ-n detector. The possible explanation for such behavior may be due to large charge generation disturbing the electric field in the sensor. The same conditions were used for Americium (Am-241) measurements.
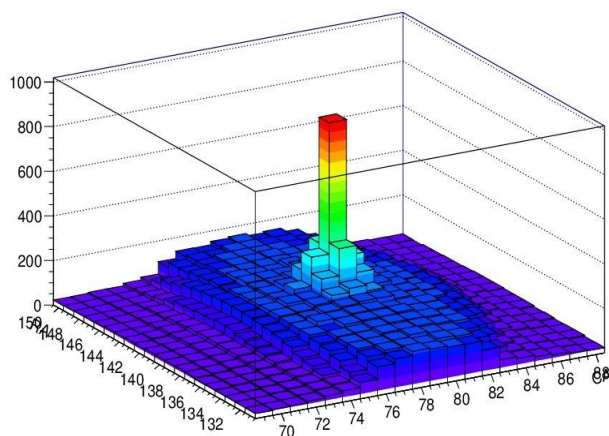

Figure 22: IR Laser setup
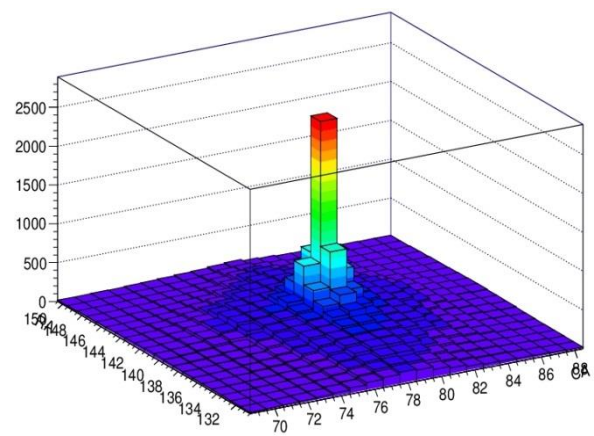

Figure 23: Before optimization

Figure 24: After optimization

2.3 Measurements using Am-241 source

The radioactive source used for this test setup is Am-241 with the activity of 10 mCi (=370MBq). As the incident photon rate is low (occupancy below 0.1%), we keep the source close to the sensor in the black box.

The DIPIX2 CZ-n type detector is used for this measurements and the optimized integration time and back bias voltage is applied, which is calculated in subchapter 2.2. The data was taken in two runs. Firstly the pedestal data of 500 frames was taken and then the signal data using radioactive (Am-241) source. The average pedestal value and the noise RMS were computed after suppressing initial frames (about 50-100), bad pixels, bad frames (having large number of bad pixels) and common mode. After the application of all mentioned cuts the Gaussian shape of the pedestal distribution is restored and the standard deviation (noise) of the data is significantly reduced. A simple clustering algorithm is used to find the peaks of Am-241 source and group of L x-ray lines. The frames for which the photons were registered (using 7σ noise cut) were extracted. Single, double, triple and quadruple clusters are calculated from each frame. Low energy lines with smaller sigma are seen in single and double pixel clusters and high energy (i.e. 59.5keV) peak with larger sigma is seen mostly in triple and quadruple pixel clusters. Figure 7 show the measurement result of radioactive (Am-241) source after merging all clusters. A well separated signal from noise is seen. The measured peaks correspond to the energy spectrum of Am-241. The conversion factor of whole readout chain (gain) of the sensor is 12.2μV/e⁻. The energy resolution i.e. full width at half maximum (FWHM) for single pixel cluster is ~1.66keV at 13.9keV. The equivalent noise charge of DIPIX2 CZ-n detector is ~86e⁻[5]. The INTPIX3 measurement result using Am-241 source are presented in poster [6].
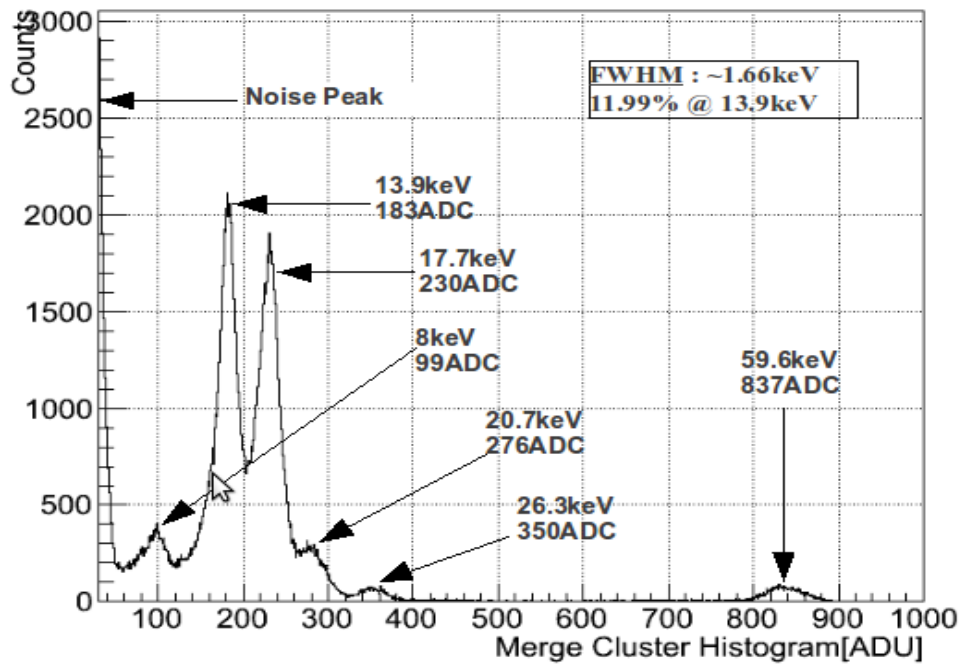
Figure 25: The energy spectrum of Am-241 from DIPIX CZ-n type detector obtained after merging all clusters.

2.4 Irradiation using cobalt Co-60 source

DIPIX2 CZ-n detector was irradiated with Co-60 γ's, and dose rate was 1.43Gy/min. The irradiation was interrupted every 40min to change the alanine capsule and last for 6 hour in total. The beam profile is known using TLD foil and Alanine capsules are placed below the DIPIX2 to calculate the dose rate. The shift in pedestal values before and after irradiation are shown in Figure 9 and 10 respectively. Please refer to the paper for the irradiation results of INTPIX3 and DIPIX2 [7,8].

Figure 9: Preirradiation

Figure 10: 0.5kGy Irradiation

2.5 Summary

The monolithic SOI detectors are functional and the prototypes designed using this technology are characterized using IR laser, Am-241 and Co-60 source. The ENC for DIPIX2 CZ-n is ~86e$^-$ and the energy resolution is 11.99% at 13.9keV which shows improvements comparing to previous sensors in this technology [6].

REFERENCES

[1] J.R. Schwank et al., Radiation Effects in SOI Technologies, IEEE Transactions on nuclear Science, Vol 50, No. 3 (2003).
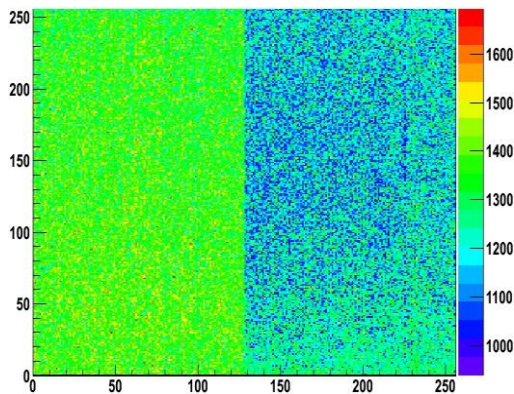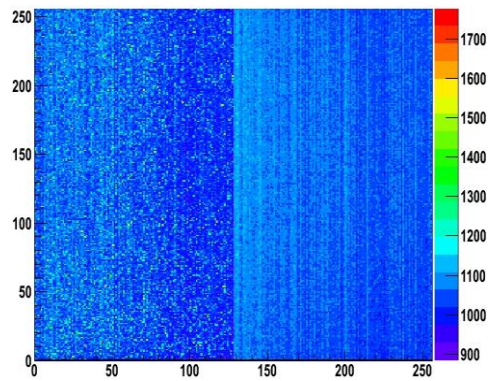
[2] R. Ichimiya, et al., Reduction techniques of the back gate effect in the SOI Pixel Detector, TWEPP (2009), 68-71.

[3] Y. Arai et al., Development of SOI pixel process technology, Nucl. Inst. Meth. A636 (2011), s31-s36.

[4] Y. Arai et al., First Results of 0.15 um CMOS SOI Pixel Detector, SNIC Symposium, (2006).

[5] M. I. Ahmed, Y. Arai, M. Idzik, P. Kapusta, T. Miyoshi, M. Turala , Measurement results of DIPIX pixel sensor developed in SOI technology, Nucl. Inst. Meth, (2012) in print.

[6] T. Miyoshi, Y. Arai, R. Ichimiya, Y. Ikemoto, A. Takeda, M. I. Ahmed, Poster P-in-n and n-in-p sensor performance study of SOI monolithic pixel detectors, at 8th Hiroshima Symposium (2011).

[7] K.Hara et al., Developemnt of FD-SOI Monolithic pixel devices for High-Energy charged particle detection.

[8] T. Miyoshi, Y. Arai, M. I. Ahmed, P. Kapusta, R. Ichimiya, Y. Ikemoto, F. Yowichi, T. Kazuya, A. Takeda, High-Resolution Monolithic Pixel Detectors in SOI Technology, International Workshop on Semiconductor Pixel Detectors for Particles and Imaging (PIXEL2012), 2-7 September 2012, Inawashiro, Japan

Project Coordinator: Christian Schmidt, GSI.

Prasoon Ambalathankandy, ESR, WFiIS, AGH, Cracow. Supervisor: Marek Idzik.

Shahinur Rahman, ER, GSI, Darmstadt. Supervisor: Eleni Berdermann

INTRODUCTION

The report presented here accounts for the works done on design and test of readout electronics for forward calorimetry for ILC, and in particular for the readout of LumiCal detectors. The overview of the LumiCal detector and its readout electronics is given in [1]. The work was dedicated to design and measurements of one of the readout ASICs (Application Specific Integrated Circuit) for LumiCal detector, namely the multichannel ADC. Chapter 1 details about Test and Measurement of ADC prototype. A part of this work was also reported during 1st MCPAD network meeting. Chapter 2 is dedicated to design, simulation, synthesis and implementation of slow control interface for multichannel ADC ASICs using SPI and I2C protocols. A quick discussion on both protocols their differences and advantages have also been included.

1. ADC TEST AND MEASUREMENT

A power scalable 10-bit pipeline ADC developed for the luminosity detector at the future International Linear Collider was thoroughly tested and characterized. The prototype ASIC is fabricated in 0.35µ CMOS technology. ASIC containing six ADC versions, baseline ADC version and slightly different versions (sampling switches, CMFB type, etc.) were tested. After the basic functionality test with a DC input signal, the complete measurements of ADC static & dynamic parameters were performed using a dedicated FPGA based test setup. The ADC static performance is quantified with INL and DNL measurements. The dynamic parameters are quantified with SINAD, THD, SNHR & SFDR parameter measurements.

ADC Specifications

ADCs converts an analog signal input to a digital output code. ADC measurements deviate from the ideal due quantization error, process variations in integrated circuits (ICs) and various sources of inaccuracies in the analog-to-digital conversion process. The ADC performance specifications [2] quantify errors that are caused by the ADC itself. It is essential to understand the ADC performance specifications which are generally categorized in two cathegories: static and dynamic. The application determines which specifications the designer will consider the most important.

Static ADC performance

The Differential non-linearity, or DNL, specifies the deviation of any code in the transfer function from an ideal code width of 1 LSB. The DNL is determined by subtracting the locations of successive code transition points after compensating for any gain and offset errors. The untegral nonlinearity or INL, is a result of cumulative DNL errors and specifies how much the overall transfer function deviates from a linear response. Example results of the measured DNL and INL errors for prototype ADC are shown in Figure 1. It is seen that both errors

stay well below 1 LSB, thus demonstrating a good ADC performance. A more complete discussion of ADC static performance may be found in [3].
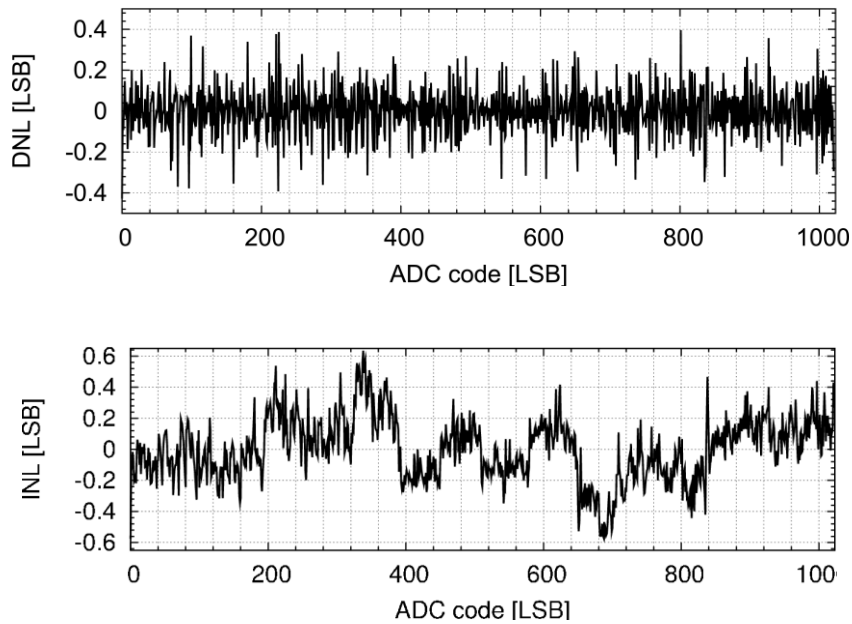
Figure 1: Measured DNL (top) and INL (bottom) errors

Dynamic ADC performance

There are few important dynamic parameters quantifying the ratio of signal (technically its RMS value) to noise/distortion (its RMS) at the assumption that ideal sine wave signal is sent to ADC input. The SINAD is a signal to noise and distortion ratio, the THD (Total harmonic distortion) is a ratio of the square root of harmonic distortions to signal, the SNHR is a signal to noise ratio (excluding harmonics) ratio, and SFDR (Spurious free dynamic range) is a ratio of signal to largest spurious spectral component observed over the full Nyquist band.

Figure 2: Example of measured dynamic parameters

An example of the measured FFT spectrum with all dynamic parameters calculated is shown in Figure 2. A good signal to noise and distortion (SINAD) ratio of 57.9 dB is measured, which corresponds to an effective ADC resolution [2] of 9.3 bits. The detailed discussion of dynamic performance may be found in [3].

2 SLOW CONTROL FOR ADC ASIC

The aim of this project is to design and implement a slow interface for multichannel ADC for LumiCal detector. Two serial protocols were under consideration Serial Peripheral Interfac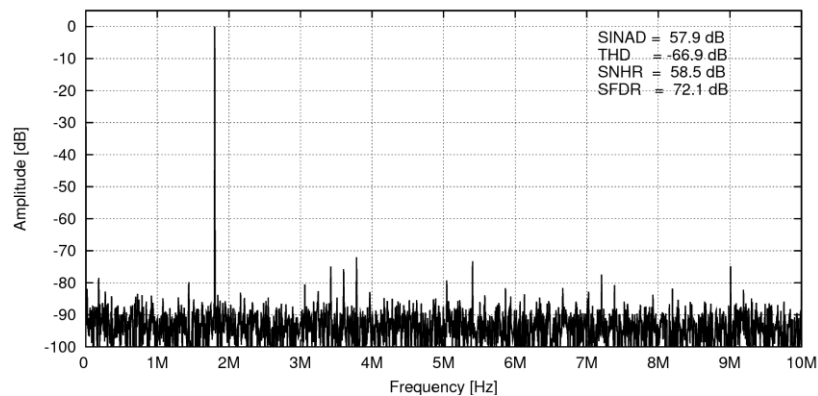e (SPI) and Inter-Integrated Circuit (I2C). Both protocols have some advantages and disadvantages so two separate design were done to test in practice both protocols. Both these protocols are master-slave protocols and the ASIC slow control block have to a slave device. The SPI [4] is rather simple protocol which makes it relatively easy in implementation. Its main disadvantage is lack of addressing and unidirectional wires. The I2C standard [5] is much more standardized which make it much harder to implement but offers more features comparing to SPI like addressing and bidirectional communication over only two signal wires.

Slow control using SPI

Slow control block based on SPI protocol is a slave SPI module that works in SPI mode '0' (active posedge and zero on input in idle state). Because there is no internal data structure in SPI protocol so the authors defined its own.

Information is send to the ASIC in 16-bit words called "commands". The serial command interpreted by the slow control block has 4-bit header (constant), 2-bit address, 2-bit internal register address and 8-bit data. The most significant bit MSb is transmitted first. The structure of the command is shown below.

1	0	1	0	A1	A0	C1	C0	D7	D6	D5	D4	D3	D2	D1	D0

The SPI command protocol defined for the LumiMulti ADC chip.

Slow control using I2C

I2C protocol is defined very in detail comparing to SPI. For example the addressing is included in the protocol. The address is 7-bit long. The protocol needs some asynchronous circuitry to detect "start" and "stop" special signaling sequences. It also defines that each data package (8 bit) is acknowledged.

The structure of I2C data package with acknowledgment is shown below.
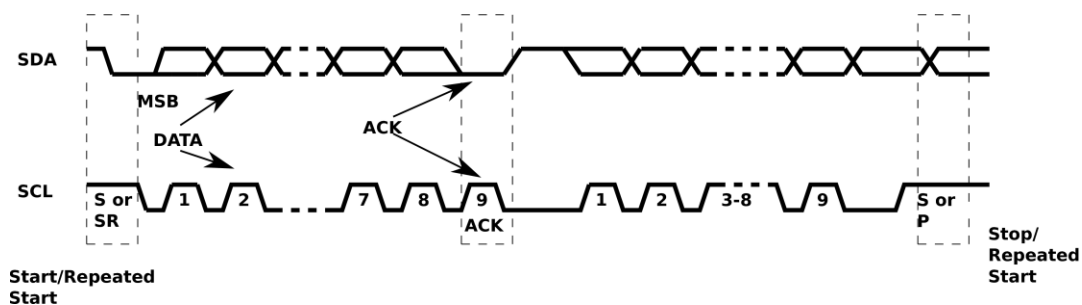
Because of all reasons above the implementation of I2C slow control module is also more complicated comparing to SPI.

Design(RTL) & Simulation

For both protocols the design and implementation was based on the same principles so it will be described together.

Slow control block (in both cases) was designed using fully digital flow starting from the definition of block functionality done in one of Hardware Description Language (HDL), in this case Verilog HDL, followed by verification. After these steps block was implemented using automatic synthesis and semi-automatic place-and-route tool to obtain final layout.

Once the functional design in Verilog HDL was completed it had to be verified and for which one can develop a test bench using also Verilog HDL to apply large number of stimuli at the input and check the output that is generated by the tested block (Design Under Test – DUT). For the described designs it is very inconvenient to check every possible combinations of the input manually by visual inspection of simulation results. So a self-checking test-bench was created to ensure the functional correctness of the design.

Described self-checking verification needs some metrics which helps to answer the question: "Are we checking everything?". One of such a metric is code coverage. The code coverage analysis can answer the question if each line/statement of a verified code was executed (statement coverage), if each condition was true and false (condition coverage) and if each signal has changed from 0 to 1 and back during simulation (toggle coverage). In first two cases achieving 100% coverage is a must while in the last toggle case it is very difficult and frequently not necessary.

Implementation & Testing (Prototype)

The Logic Synthesizer – Encounter RTL Compiler was used to turn the abstract RTL code written in Verilog HDL into a design implementation in terms of logic gates (netlist), to target the creation of ASICs. The second major phase in the ASIC design is commonly known as the backend where the cells in the netlist are placed on the die and then routed. The layout generated in AMS 0.35um CMOS technology for I2C slow control block by Encounter – place and route tool that is just prior to be submitted for IC fabrication is shown in Figure 3. The files corresponding to this layout were sent to fabrication.

Post-silicon validation is the last step in the development of a semiconductor integrated circuit. As we cannot rely on pre-silicon design verification alone to detect all design bugs, the simulations done during design phase are several orders of magnitude slower than actual silicon device. Post-silicon validation involves operating a manufactured chip in actual application environments to validate correct behaviors over specified operating conditions. A PCB was designed to host the just fabricated miniASIC. The I2C Master programmed on FPGA was sending out the set of data which would correctly address the Slave on the miniASIC. In response to the command received by the Slave it would write a set of data on to the register array and which are read back by the Master and displayed on the LED. Visual inspection of the LEDs was the first prove that the design is correct.
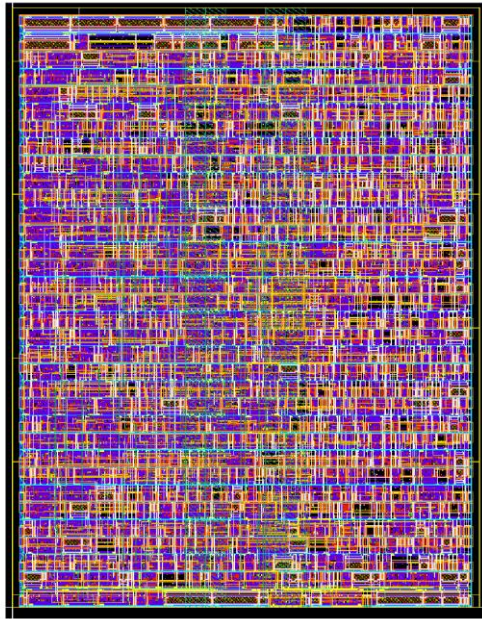
Figure 3: Layout of I2C block

REFERENCES

[1] H. ABRAMOWICZ, ET AL., (J. AGUILAR, P. AMBALATHANKANDY, M. IDZIK, SZ. KULIS) FCAL COLLABORATION, **Forward instrumentation for ILC detectors,** 2010 JINST 5 P12002

[2] *IEEE* Standard for Terminology and Test Methods for Analog-to-Digital Converters IEEE Std 1241-2000

[3] M. Idzik, K. Swientek, T. Fiutowski, S. Kulis, P. Ambalathankandy, A power scalable 10-bit pipeline ADC for luminosity detector at ILC JINST 2011

[4] SPI Block Guide V03.06, Freescale Semiconductor

[5] Philips I2C handbook(1999) NXP Semiconductors

Project Coordinator: Stefano Miscetti, INFN Frascati

Mary Tsagri, ESR, CERN. Supervisor: John Apostolakis

Filimon Roukoutakis, ER, INFN Frascati, Supervisor : Stefano Miscetti

INTRODUCTION

This project aimed to make an optimization of Monte Carlo tools based on state of the art simulation and detailed comparison and tuning on experimental data used as benchmark. The report is divided in two parts related to the specific tests .. In chapter 1,2 and 3 neutrons on gases whild on 4 the … In chapter 5 we concentrate on the effect of simulation of neutron response on calorimetry.. ……

1 SIMULATION OF GAS MIXTURES FOR HEP

This chapter focuses on various transport characteristics of argon-based gas mixtures, which are required for the high performance of HEP gas detectors. The requirements for high luminosity tracking lead to a compromise between several drift properties such as high primary ionization, low diffusion, low *Lorentz* angle and high drift velocity.

Results 1.1

The single ideal gas mixture does not exist. The desired detector performance, the purpose of use and the detector geometry dictate the choice of the gas mixture. As an example, the Gossip detector is intended for the upgrade of ATLAS inner tracker. Hence it will have to operate in a 2 T magnetic field. The following simulation results were produced for a Gossip detector of 50 um avalanche gap and for a gas gain equal to e^8 (~3000) which corresponds to a Townsend coefficient α, which for the case of Ar/CO_2 is around 1600/cm. With the help of the Garfield code, we find that the electric field for the amplification volume when α≈1600/cm is: E_{amp}≈100 kV/cm. From this, we can calculate the electric field in the drift volume and therefore the Lorentz angle.

In this work we present simulation results from three points of view. Tables 1 and 2 summarize the most important drift properties for various argon-based gas mixtures and indicate the most proper gas mixture for the Gossip detector.

From Tables 1 it is obvious that the number of candidate gas mixtures and gas concentrations that one can create and test are pretty large. However, parameters such as inflammability, cost, aging, neutron capture and toxicity restrict the use of many gas mixtures. For instance, as a result of our study, the choice of the ingredients in a gas mixture for the Gossip detector narrows down to argon and CO_2. Of course, this choice may vary from detector to detector as it always depends on the experiment requirements.
None of the gas mixtures presented in this work is satisfactory as an exclusive can dictate for use in the Gossip detector. Among the various reasons for this are the operational stability (sparks), the high drift velocity and the low diffusion. Nevertheless, the argon and CO_2 mixture satisfies pretty well most of these prerequisites. Moreover, argon-based mixtures provide more accurate particle identification and better spatial resolution compared to the other gas mixtures becoming thus a good candidate for the Gossip detector.

2 TEST OF GEANT-4 EM SIMULATION IN THIN GAS LAYERS

A second important step, which is the scope of this chapter, is that of verifying and clarifying the behavior of the Geant4 electromagnetic (EM) physics constructors from the eV to the TeV energy range, focusing on the detector performance simulation results. The Standard EM Physics working group and the Geant4 Low Energy EM Physics Working Group develop and maintain a set of models to describe EM interactions. Both teams are continuously improving and updating Geant4.

As shown in this Chapter, we found an unexpected ionization energy loss distribution of minimum ionizing particles (MIPs) in thin gas layers for several Geant4 constructors. Most of the constructors produce an unphysical shoulder on the higher energy side of the otherwise smooth Landau distribution. This work helped the Geant4 team to localize and understand problems in the simulation. The newer releases of Geant4 no longer produce the shoulder of the spectral shape of the ionization energy loss of MIPS in matter. In particular, the expected distribution in gases where this observation was done, has improved.

Gas mixture	E_{amp} [kV/cm]	E [V/cm]	Drift v [cm/μs]	σ_T [μm]	σ_L [μm]	Lorentz angle [deg]
Ar:CO$_2$ [50:50]	105.6	5000 (no max)	8.01	203	123	(v_E,v_{BT}): 4.88 (v_E,$v_{E\times B}$): 14.6
Ar:C$_2$H$_6$ [50:50]	86.4	1744	4.67	192	127	(v_E,v_{BT}): 36.4 (v_E,$v_{E\times B}$): 20.5
Ar:CH$_4$ [50:50]	96.8	690	6.75	151	161	(v_E,v_{BT}): 40.3 (v_E,$v_{E\times B}$): 16.6
Ar:CH$_4$ [90:10]	81.3	800	8.27	101	108	(v_E,v_{BT}): 41.1 (v_E,$v_{E\times B}$): 16.9
Ar:CF$_4$ [50:50]	90.4	3174	11.5	98.5	55.5	(v_E,v_{BT}): 19.4 (v_E,$v_{E\times B}$): 25.3
Ar:CF$_4$ [80:20]	83.4	1507	9.45	109	83.7	(v_E,v_{BT}): 35.4 (v_E,$v_{E\times B}$): 23.1
Ar:CF$_4$ [90:10]	81.3	800	8.27	101	108	(v_E,v_{BT}): 41.1 (v_E,$v_{E\times B}$): 16.9
Ar:DME [90:10]	78.1	1529	3.64	299	162	(v_E,v_{BT}): 12.8 (v_E,$v_{E\times B}$): 20.3
Ar:DME [50:50]	87.2	5000 (no max)	4.94	157	96.3	(v_E,v_{BT}): 1.66 (v_E,$v_{E\times B}$): 8.61
Ar:CF$_4$:CO$_2$ [60:10:30]	98.1	5000 (no max)	8.08	213	117	(v_E,v_{BT}): 5.54 (v_E,$v_{E\times B}$): 15.1
Ar:CO$_2$:iC$_4$H$_{10}$ [80:10:10]	81.3	5000 (no max)	5.36	262	148	(v_E,v_{BT}): 3.36 (v_E,$v_{E\times B}$): 11.3
Xe:CF$_4$:CO$_2$ [50:30:20]	89.7	4905 (no max)	7.98	151	76	(v_E,v_{BT}): 5.81 (v_E,$v_{E\times B}$): 15.7

Gas mixture	E_{amp} [kV/cm]	E [V/cm]	σ/v [ns/cm]	Lorentz angle [deg]
Ar:CO$_2$ [50:50]	105.6	5000 (no min)	1.53	(v_E,v_{BT}): 4.88 (v_E,$v_{E\times B}$): 14.6
Ar:C$_2$H$_6$ [50:50]	86.4	3083	2.54	(v_E,v_{BT}): 6.84 (v_E,$v_{E\times B}$): 14.8
Ar:CH$_4$ [50:50]	96.8	1133	2.24	(v_E,v_{BT}): 33.3 (v_E,$v_{E\times B}$): 20.4
Ar:CH$_4$ [90:10]	82.8	360	6.91	(v_E,v_{BT}): 39.4 (v_E,$v_{E\times B}$): 15.4
Ar:CF$_4$ [50:50]	90.4	3859	0.47	(v_E,v_{BT}): 14.8 (v_E,$v_{E\times B}$): 23.2
Ar:CF$_4$ [80:20]	83.4	1854	0.86	(v_E,v_{BT}): 31.2 (v_E,$v_{E\times B}$): 24.1
Ar:CF$_4$ [90:10]	81.3	1068	1.24	(v_E,v_{BT}): 37.9 (v_E,$v_{E\times B}$): 19.5
Ar:DME [50:50]	87.2	5000 (no min)	1.95	(v_E,v_{BT}): 1.66 (v_E,$v_{E\times B}$): 8.61
Ar:DME [90:10]	78.1	1579	4.44	(v_E,v_{BT}): 12.3 (v_E,$v_{E\times B}$): 19.9
Ar:CF$_4$:CO$_2$ [60:10:30]	98.1	5000 (no max)	1.45	(v_E,v_{BT}): 5.54 (v_E,$v_{E\times B}$): 15.1
Ar:CO$_2$:iC$_4$H$_{10}$ [80:10:10]	81.3	5000 (no min)	2.76	(v_E,v_{BT}): 3.36 (v_E,$v_{E\times B}$): 11.3
Xe:CF$_4$:CO$_2$ [50:30:20]	89.7	5000 (no min)	0.95	(v_E,v_{BT}): 5.71 (v_E,$v_{E\times B}$): 15.6

Table 1: Drift properties as they were calculated for gas gain equal to 3000: (Left) drift properties based on maximum drift velocity, (Right) drift properties based on the minimum ratio between the longitudinal

2.1 Results
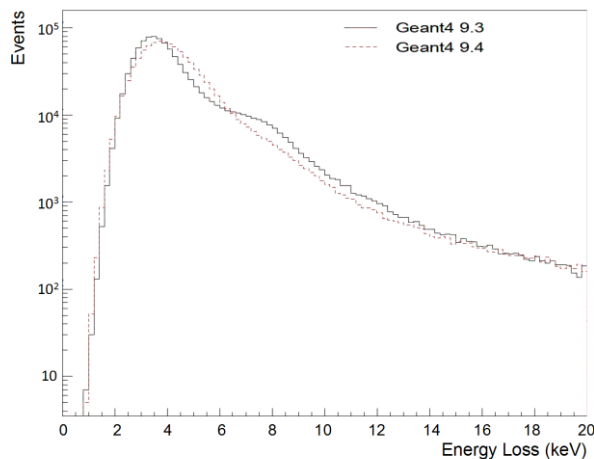
We have investigated the ionization energy loss of minimum ionizing particles in thin gas layers as it has been simulated by the Geant4 code. Several models showed an unexpected shoulder on the high energy tail of the Landau distribution for 500 MeV/c incident electrons in various gas constituents. We provided a detailed validation

Figure 1: Energy loss distribution of 500 MeV/c electrons in 15 mm thin chamber, filled with 80% Ar and 20% CO$_2$. This result shows clearly the improvement reached with the updated fluctuation model (Geant4 release 9.4). The new model calculates the ionization energy loss of charged particles in matter more accurate and follows a normal distribution.

[2] by examining possible shoulder dependence on the electron incident energy, the material of the detector, the thickness of the material, the various physics processes and the fluctuation model included in the Geant4 code.

The Geant4 fluctuation model, which reproduces the ionization energy loss for charged particles in thin layers, was recently improved in order to become properly applicable also to very thin layers or low density materials [3]. This revised model is also less dependent on step limitations, e.g. range cut-offs for the production of secondary particles, compared to its previous versions. Note that the fluctuation model applies to all the EM physics constructors in Geant4. Therefore, improves by default all the different physics constructors (Standard, Livermore and Penelope).

Finally, we arrive to the conclusion that the shoulder on the high-energy tail of the ionization energy loss distribution is not a physical phenomenon. Following various cross checks we have undertaken during this work, the origin of the shoulder was finally localized and traced to the fluctuation model implemented by the Geant4 code. Thus, the shoulder seems not to be some new physics but rather an inaccuracy of Geant4. It is worth noticing here that this correction to the fluctuation model may have a significant impact for simulations also in LHC experiments including their high energy showers, since the corrected Geant4 release might imply improvements which could be relevant in certain cases. However, a dedicated, precise measurement of the ionization energy loss of MIPs in thin gaseous detectors is needed.

3 NEUTRON SIMULATION IN GASES IN GEANT-4

This chapter presents a study of the neutron simulation in Geant4. In this work, we review and compare the behavior of neutron cross-sections in Geant4 for key chamber gases with measured neutron cross-sections including older and recent data sets. Following this work, the Geant4 group has updated nuclear data in Geant4 improving its performance and reliability.

3.1 Results

We have compared G4NDL versions 3.13 cross-sections with several evaluated neutron data sets. We focused our study on typical elements used in gaseous detectors for HEP experiments such as helium, argon, xenon and krypton, but we have also studied some main constituents of quenchers such as hydrogen, carbon and oxygen. As a result, the G4NDL 3.13 is mostly based on the older versions of JEFF evaluated neutron data sets.

The most recent evaluated nuclear data library ENDF/B-VII.0 has many improvements making it the best candidate to base a future G4NDL version as described in details in [4]. The most relevant advantages for particle physics detectors are:
   a. new and precise neutron cross-sections are available for more elements,
   b. new evaluations up to 150 MeV for many neutron- and proton-induced reactions,
   c. neutron and proton reactions with new light nucleus and
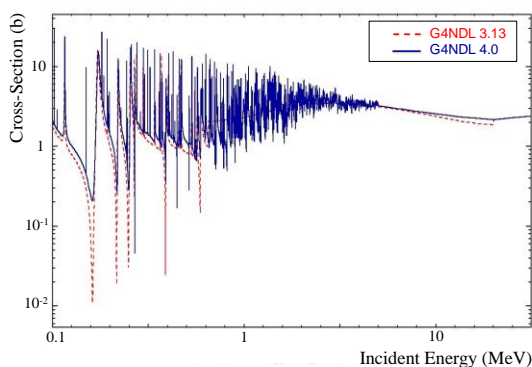   d. a larger set of photonuclear reactions are included.

Figure 2: Argon cross-sections. Comparison of old (red) and new (blue) G4NDL (ENDF/B-VII.0) total neutron cross-sections versus incident neutron energy. The latest Geant4 release (9.5) now follows the best available data.

Recently, the new ENDF/B-VII.0 neutron cross-sections were implemented in the last G4NDL (version 4.0). The

new Geant4 neutron data library is included in the Geant4 9.5 release and contains improved data for most of the chemical constituents. The data had to be translated into the Geant4 format, in order to convert the resonance contribution into cross-section data points, and also to transform all cross-section data points into linear-linear interpolated form, which is required by the Geant4 code.

4 APPLICATION EXAMPLE: DATA AND MC COMPARISON OF MICROMEGAS

This Chapter presents some measurements taken in Saclay with a Micromegas detector [5], focusing on the experimental estimate of the electron transmission. In our test setup, we could vary the operating conditions of the Micromegas detector, applying different voltages to the anode, the mesh and the cathode. This allowed us to compare the Micromegas performance with a full simulation made with Ansys and Garfield++.
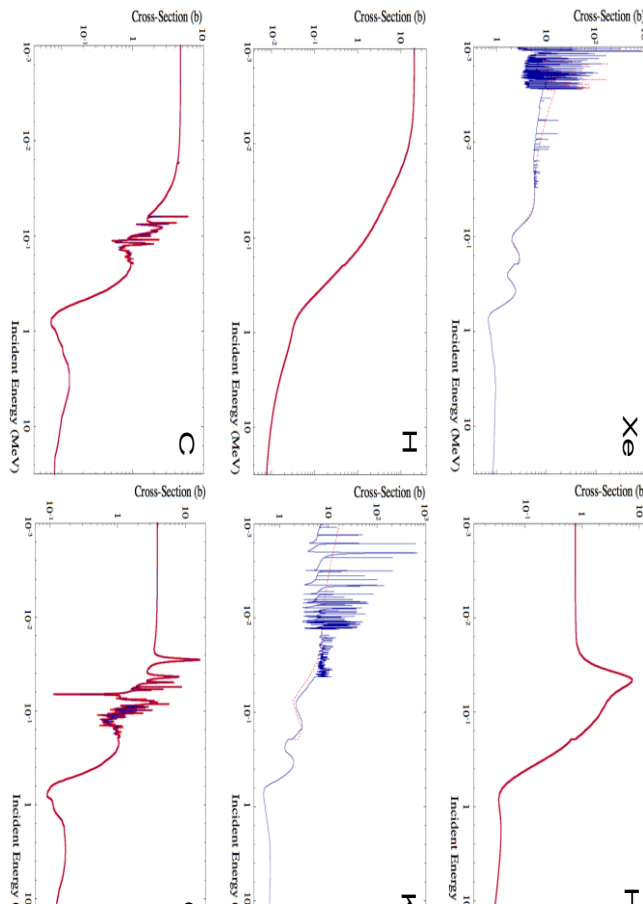

Figure 3: Comparison of old (red) and new (blue) G4NDL (ENDF/B-VII.0) total neutron cross-sections versus incident neutron energy for various constituents. The latest Geant4 release (9.5) now follows the best available data

4.1 Results

We performed a simulation with the Garfield++ code and we compared the results with the measurements. Similar values to the experimentally obtained transmission values were also derived by our simulations. A precise model of the micro-mesh was introduced, while the electric field was calculated using the Ansys code.
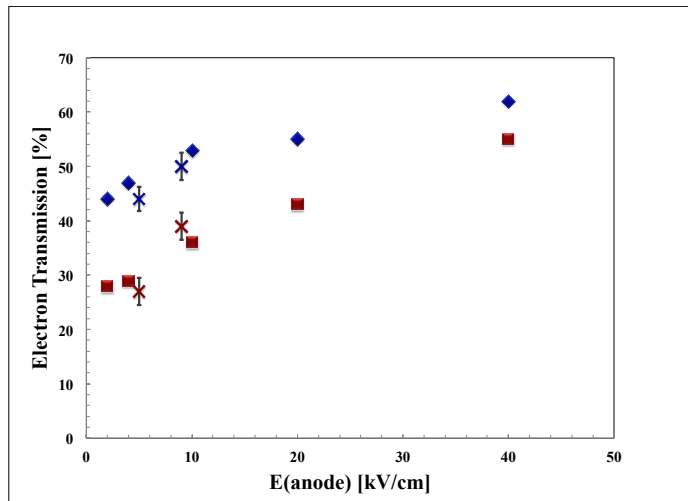
Figure 4: Experimental validation of simulation results using Ansys and Garfield++ tools. The blue points refer to the cathode mesh while the red ones refer to the cathode wires plane for the gas mixture: 50% Ar and 50% C_2H_6. The blue and red crosses are the corresponding measured values for anode electric fields $E_{anode} \approx 5 \sim kV/cm$ and $E_{anode} \approx 9 \sim kV/cm$, using cathode wires (red crosses) and cathode mesh (blue crosses).

A uniform voltage was applied on the cathode mesh ($V_{cathode}$) and on the anode (V_{anode}), when simulating the actual experimental configurations. Both, experimental and simulated results are shown in Figure 4; it is seen that the maximum measured transmission with the cathode wires is ~39\%, while that with the cathode mesh is, as expected, even better and equal to ~50\%. Interestingly, these two values, at $E_{anode} \approx 9$ kV/cm, together with the other two values at a lower anode electric field, at $E_{anode} \approx 5$ kV/cm, reproduce the simulation results.

The agreement between simulation and measurement is quite satisfactory. This is certainly an experimental validation of the simulation codes used throughout this work. In addition, these measurements provide more insight of the actual processes occurring during this last step of signal creation in a Micromegas detector. We recall, this very last propagation of the initial ionization charges occur in a region whose configuration distinguishes Micromegas from all the other detectors used in particle physics

5 NEUTRON RESPONSE ON SCINTILLATING FIBER CALORIMETERS

This chapter deals with a benchmark test of the simulation of neutron response and detection efficiency in heterogeneous calorimeters. This study was motivated by the findings [6-7-8] of a tremendous increase of neutron detection efficiency, in the energy range between few to 200 MeV, of scintillating fiber calorimeters with respect to bulk scintillators when comparing with the equivalent thickness of scintillating material. In the following we refer to KLOE, KLOne and Spacal detectors as their response found in data has been used as benchmark to compare with simulation. KLOE and KLOnE have the basic intrinsic construction details, 1 mm diameter fibers positioned at the vertices of an equilater triangle inside thin (0.5 mm thickness) grooved lead layers, for a fiber:lead:glue ratio of 48:42:10 in volume. The only practical difference is the fiber length: KLOnE is a small size prototype of the KLOE barrel calorimeter which was exposed to the neutron beam of TSL, Uppsala, and has a length of 65 cm while the KLOE modules have 400 cm length. We call Spacal a different kind of calorimeter where the fibers are arranged at the vertices of square structure and result in a fiber:total volume ratio of 19.5% [9].

The requirement for a detailed simulation of several calorimeter geometries using both Geant4 and Fluka led to the choice of utilizing Virtual Monte Carlo (VMC) [10] as a framework for this detailed study. VMC has been developed by the ALICE-LHC collaboration and it is also used by other collaborations such as PANDA and ILC-D. It is also currently part of the ROOT Data Analysis Framework [11-12]. VMC provides a consistent detector description between Geant4 and Fluka, by using the ROOT geometric modeller. In addition, since VMC has been modelled after Geant3, we have the possibility to use also this simulation code.

During the first period of the project, the existing FORTRAN code for the Geant3 simulation of an electromagnetic calorimeter prototype, from KLOE collaboration, has been studied thus allowing us to extract the Geant3 geometry and to create the first geometry in ROOT format. Based on this, fully configurable geometries for KLOE, KLOnE and Spacal calorimeters have been implemented. In all of them it is possible to vary the dimensions of the fibers (diameter and length), their positioning grid, as well as the compositing materials.

Part of the simulation framework is the primary particle generator. The framework that we have developed allows the runtime plugging-in of a user-provided generator following a very simple interface. For our specific user-case of the calorimeters simulation, several such generators have been developed. Among them (i) a simple fixed particle "gun" which generates a specific type of particle with fixed momentum and origin, (ii) a parameterized generator to produce a specific particle whose momentum and/or position vector components follow a histogram distribution and (iii) another generator that follows the same logic used to simulate with Fluka the KLOnE calorimeter, neutrons are produced in a fixed position and with a fixed direction with random kinetic energy following a provided energy spectrum. For the latter case, we currently have three different distributions corresponding to the three different energies used during the test-beam.

Efforts were made in implementing [13] the treatment for optical response within the MC engines. In Geant4 case, we were able to observe scintillation photons produced according to the yield expected from the scintillator parameters. Geant3 does not have scintillation mechanism but we planned to implement one in VMC by back-porting the Geant4 code accordingly. This would have allowed a deeper comparison between Geant3 and Geant4 optical transport properties since Geant3 has optical photon transport capabilities itself. However, after consulting the Geant4 optical transport experts, it was understood that for the given detailed geometries the optical transport results would require a lot of testing to assure that they were physically consistent. Furthermore, the different required parameters for Geant4 and Fluka optical transport would require additional validation, since optical properties are currently not part of the VMC framework. Finally, in order to speed-up the simulation, usually only a fraction of the scintillation photons is simulated. Since most of the parameters to control this fraction are mainly experimentally measured (photon collection efficiency, photon attenuation in the material and photo-sensor quantum efficiency) and are outside of the scope of this simulation framework, it was decided to emulate the optical response in the custom-written digitization phase, where full control of the properties was possible. This provided additional flexibility in tuning the optical response during the fast digitization phase instead of the relatively computationally intensive simulation phase. It also allows to introduce BIRK's mechanism in the light yield production at this stage.
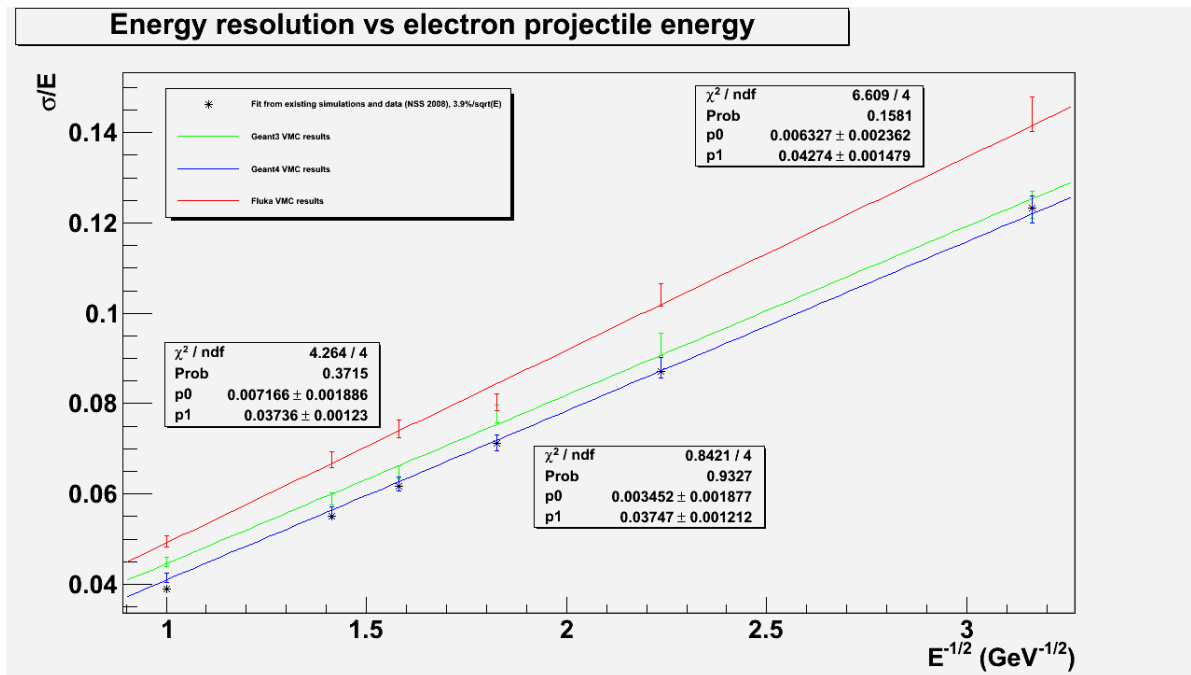
Figure 5: Dependence of the simulated energy resolution as a function of 1/√(E/GeV) for the KLOE calorimeter prototype using Geant-3 (green curve), Geant-4 (blue curve) and Fluka (red curve). Black points refer to experimental Data measured during prototyping phase (NIM-95).

In addition to the optical transport, the digitization includes the configurable readout segmentation of the detectors in an integrated way by considering as input the hits of a specific geometry and Monte Carlo engine and as output the number of photoelectrons per readout channel stored in a portable ntuple. The generic simulation framework (EasyVMC) along with the MC-PAD-specific calorimeter geometries was available as the first of two milestones in July 2011.

The following are some of the most important results obtained using Geant3.21/11, Geant4.9.4.p04, Fluka2008.03 and ROOT 5.28.00 (with the appropriate versions of VMC add-ons).

5.1 Electromagnetic showers: energy resolution and response

This was performed for validation of the framework. Fixed energy beam and the default E/M options of each simulation engine were used.

For the KLOE/KLOnE calorimeter, we have generated 1000 events at different beam energies with and without adding the photoelectron yield. We were able to observe a Gaussian response for each energy and disentangle the sampling fluctuation from light yield fluctuation. In Figure 5, we show the comparison among different simulation engines and experimental data from the prototype. The Geant4 simulation nicely reproduces experimental data. For the Spacal calorimeter, we have demonstrated that, when used in head-ON configuration, the tunnelling effect of electrons impinging at an angle of 0° with respect to the fiber axis originates a clear deterioration of response and resolution (as experimentally observed). The results obtained at an angle of 2.5° are consistent with data obtained in the dedicated test beam. (Geant4 E/M physics list results shown here). Results of the simulation are reported in Figure 6.
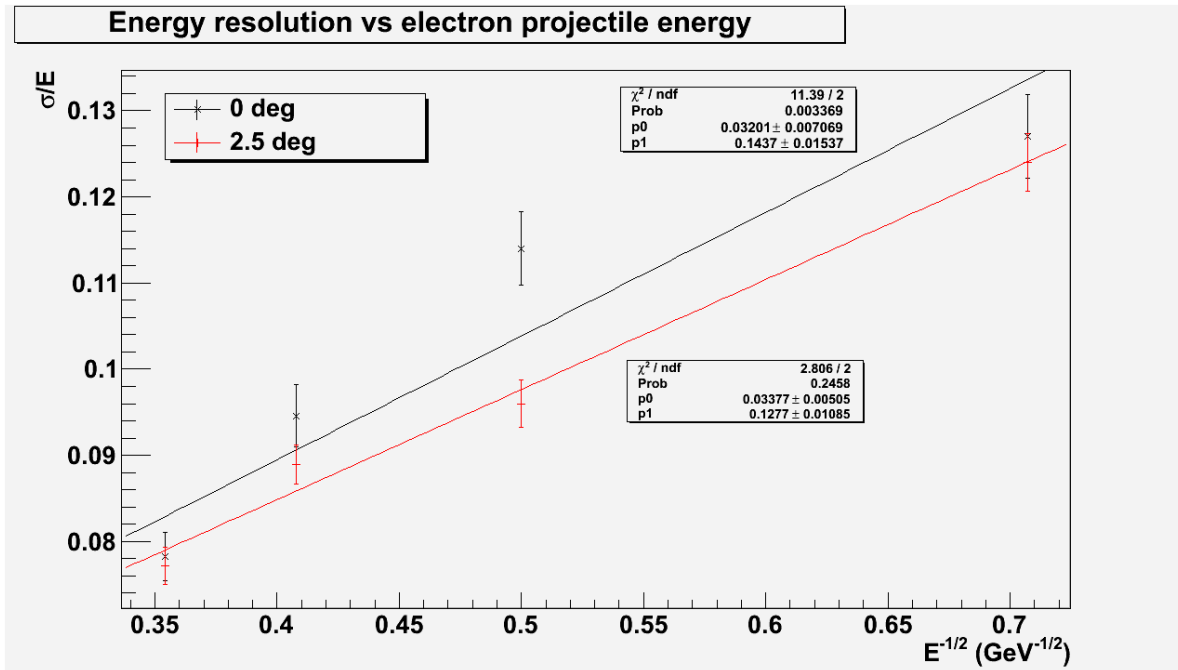
Figure 6: Dependence of the simulated energy resolution as a function of 1/√(E/GeV) for the SPACAL-2 calorimeter prototype using Geant-4 simulation. The black(red) curve is for an impinging angle of 0°(2.5°) with respect to the fiber axis.

5.2 Validation of calorimeter response to proton

Knowing that the response to neutron in a scintillator is basically due to the elastic scattering of neutrons to protons and then to the energy deposited by the proton in the scintillator itself, we have tuned the simulation to provide a reasonable response to protons. In order to do that, we took advantage to the in-situ response of the KLOE EMC to a sample produced by machine background events interacting on the inner quadrupoles having protons and deuterons in the final state.
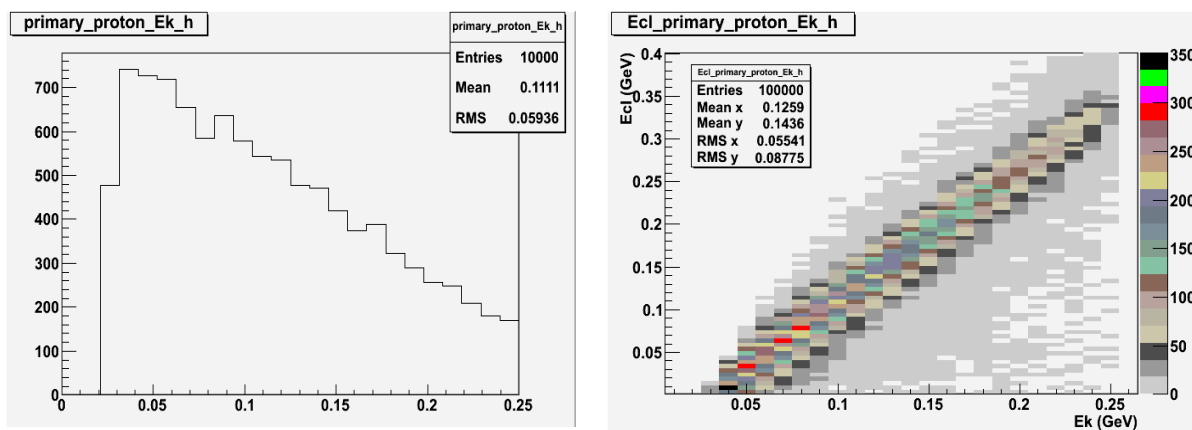

Figure 7: (Left) Distribution of proton momentum (GeV) for the data sample used to calibrate the energy response and resolution of the KLOE calorimeter; (Right) correlation between Cluster energy (GeV) and proton momentum (GeV) for the simulated sample after application of the Birk's law in the scintillation mechanism.

In the experiment, protons were distinguished from deuterons by Time Of Flight measurement in the calorimeter and tracked with high resolution by the drift chamber system. Their trajectory was extrapolated to the calorimeter and the energy of the connected clusters reconstructed. For the simulation, the detailed full size geometry was exposed to a proton beam with characteristics as measured experimentally such as the

specific momentum (see Figure 7, left) and the incident angle profile. Birk's saturation law in light yield was also taken into consideration to improve the description of the calorimeter response. The distribution of simulated cluster energy as a function of proton momentum is shown after correcting for Birk's law, in Figure 7 right. By slicing this scatter plot, we have then compared energy linearity and resolution as a function of proton momentum between data and simulation. The results are consistent with the experimental data with the exception of the small deuteron contamination which was not add to this simulation. (Geant4 E/M physics list results shown here).

5.1 Response and detection Efficiency to neutrons

Test beams for two lead/scintillating fiber calorimeters (KLOnE and Spacal-3) have been performed at TSL in 2007. The beam energy profile impinging on the calorimeter face has been simulated from experimental measurements for 3 different peak energies (28 MeV, 45 MeV and 178 MeV). Geant3 has limited hadronic interaction simulation capabilities, using out-dated Fluka routines. Geant4 has instead a variety of hadronic physics lists. We have tried different options and ended up selecting the physics list FTFP_Bertini which, according to bibliography, better reproduces a wide range of experimental results in calorimetry. In our low-energy regime Bertini cascade is the component that is actually used, while FTFP (Fritiof Parametrized) is applicable only for E >~ 6 GeV. Trying an alternative parametrization, FTFP_BIC (Binary cascade for low energies) provided similar results, within error, in our case but resulted to be much slower. The detection efficiency was extracted by performing the ratio of neutron momentum distribution for all generated events and the ones having a calorimeter cluster above a given threshold in energy. The efficiency, ε_D, is expressed in %/cm since it has been normalized to the overall scintillator thickness in the detectors. Both KLOnE and Spacal detectors have been simulated. In Figure 8, we report the results of the Geant4 simulation. At a threshold of 10 MeV we found a simulated efficiency of 3.8 % (8%) in KLOnE (Spacal) compared to the 1.9 % (8%) mesured in experimental data [8]. The simulated efficiencies are not perfectly consistent with the experimental results obtained at TSL indicating that some systematic studies are still needed to better tune the calibration of light yield and thresholds as well as the beam spot width. However, the results are really exciting since they show a definitive increase of efficiency with respect to ε_D of 0.5-1%/cm observed in bulk scintillators. This confirms the experimental observation that a denser (i.e. cheaper) calorimeter with a reasonable light yield can get even better neutron detection efficiency that a high sampling calorimeter.
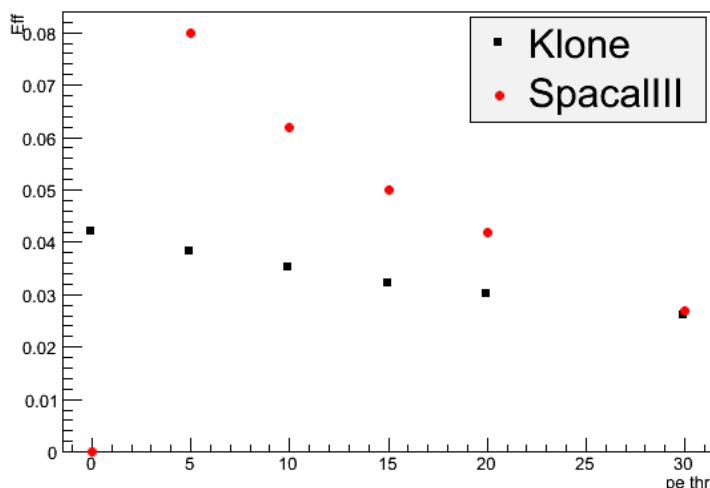

Figure 8: Geant-4 simulated dependence of the neutron detection efficiency ε_L as a function of the applied threshold for 178 MeV neutron beam with the "TLS"-like spectrum. Black (red) points are for KLOnE (Spacal-3) detector. The Threshold is expressed in MeV(electron equivalent). The efficiency is expressed in %/cm since it has been normalized to the total scintillator thickness in the detector.

References

[1]   N.Colonna et al., *The n_TOF Collaboration, Neutron cross-section measurement at the n_TOF facility at CERN*, Nuclear Instruments and Methods in Physics Research Section B 213 (2004) 49-54.

[2]   W. W. M. Allison, C. B. Brooks, J. N. Bunch, R. W. Pleming, and R. K. Yamamoto,*The ionisation loss of relativistic charged particles in thin gas samples and its use for particle identification II. Experimental results,* Nuclear Instruments and Methods 133 (1976) 325-334.

[3]   A. Schalicke, A. Bagulya, O. Dale, F. Dupertuis, V. Ivanchenko, and O. Kadri, A. Lechner, M. Maire, M. Tsagri, and L. Urban, *Geant4 electromagnetic physics for the LHC and other HEP applications,* Journal of Physics: Conference Series 331 (2011) Series 032029.

[4]   M. B. Chadwick, P. Oblozinsk'y, M. Herman, *et al.*, *ENDF/B-VII.0: Next Generation Evaluated Nuclear Data Library for Nuclear Science and Technology,* Nuclear Data Sheets 107 (2006) 2931-3060.

[5]   G. Charpak, J. Derre, Y. Giomataris, and Ph. Rebourgeard, *Micromegas, a multipurpose gaseous detector,* Nuclear Instruments and Methods in Physics Research A 478 (2002) 26-36.

[6]   M.Anelli et al., (KLOnE Collaboration) *Measurement and simulation of the neutron response and detection efficiency of a Pb-Scintillating fiber calorimeter*, Nuclear Instruments and Methods in Physics Research A 581 (2007) 368-372.

[7]   M.Anelli et al., (KLOnE Collaboration*) Measurement of neutron detection efficiency between 22 and 174 MeV using two different kinds of Pb-scintillating fiber sampling calorimeters,* Nuclear Instruments and Methods in Physics Research A 617 (2010) 107-108.

[8]   M.Anelli et al., (KLOnE Collaboration*) Measurement of the neutron detection efficiency of a 80% absorber-20% scintillating fibers calorimeter,* Nuclear Instruments and Methods in Physics Research A 626-627 (2011) 67-71.

[9]   M.Bertino et al., Nuclear Instruments and Methods in Physics Research A 357 (1995) 363.

[10]   ALICE Collaboration. *The Virtual Monte Carlo*. Computing in High Energy and Nuclear Physics, 24-28 March 2003, La Jolla, California

[11]   I. Hrivnakova. *The Geant4 Virtual Monte Carlo*. Journal of Physics: Conference Series 119 (2008) 032025

[12]   I. Hrivnakova. *The Virtual Geometry Model*. Journal of Physics: Conference Series 119 (2008) 042016

[13]   F. Roukoutakis et al. Nuclear Science Symposium Conference Record. NSS '10. IEEE. *KLOE calorimeter simulation with Virtual Monte Carlo,* 2010.